

MODELLING OF INTERACTION OF SHOCK WAVES WITH ANALYTICAL
METHODS

A THESIS SUBMITTED TO
THE GRADUATE SCHOOL OF NATURAL AND APPLIED SCIENCES
OF
MIDDLE EAST TECHNICAL UNIVERSITY

BY

MESUT KOÇ

IN PARTIAL FULFILLMENT OF THE REQUIREMENTS
FOR
THE DEGREE OF MASTER OF SCIENCE
IN
MECHANICAL ENGINEERING

FEBRUARY 2022

Approval of the thesis:

**MODELLING OF INTERACTION OF SHOCK WAVES WITH
ANALYTICAL METHODS**

submitted by **Mesut Koç** in partial fulfillment of the requirements for the degree of **Master of Science in Mechanical Engineering, Middle East Technical University** by,

Prof. Dr. Halil Kalıpçılar
Dean, Graduate School of **Natural and Applied Sciences**

Prof. Dr. M. A. Sahir Arıkan
Head of the Department, **Mechanical Engineering**

Prof. Dr. Mehmet Halûk Aksel
Supervisor, **Mechanical Engineering**

Examining Committee Members:

Asst. Prof. Dr. Özgür Uğraş Baran
Mechanical Engineering, METU

Prof. Dr. Mehmet Halûk Aksel
Mechanical Engineering, METU

Asst. Prof. Dr. Ali Karakuş
Mechanical Engineering, METU

Asst. Prof. Dr. Hediye Atik
Aerospace Engineering, Atilim Uni.

Asst. Prof. Dr. Onur Baş
Mechanical Engineering, TED Uni.

Date: 09.02.2022

I hereby declare that all information in this document has been obtained and presented in accordance with academic rules and ethical conduct. I also declare that, as required by these rules and conduct, I have fully cited and referenced all material and results that are not original to this work.

Name Last name : Mesut Koç

Signature :

ABSTRACT

MODELLING OF INTERACTION OF SHOCK WAVES WITH ANALYTICAL METHODS

Koç, Mesut
Master of Science, Mechanical Engineering
Supervisor : Prof. Dr. Mehmet Halûk Aksel

February 2022, 121 pages

In supersonic air vehicles, specially shaped air ducts are used to supply the air with required properties to the combustion chambers. Two-dimensional supersonic flow solvers used to design such geometrical shapes have become less accurate as the geometrical shape of the air duct becomes asymmetric or flow becomes three-dimensional. This problem can be overcome by solving the interaction between shock planes using analytical methods. In this study, an analytical solution model based on principles of gas dynamics is to be conducted and validation of this solution model is to be done via existing experimental data and computational fluid dynamics tools. Solution time is to be reduced and prototyping-testing expenses are to be decreased with the solution of the problem using analytical methods.

Keywords: 3D Shock-shock interaction, Supersonic corner flow, Flow field, Analytical methods, Mach reflection

ÖZ

ŞOK DÜZLEMLERİNİN ETKİLEŞİMLERİNİN ANALİTİK YÖNTEMLERLE MODELLENMESİ

Koç, Mesut
Yüksek Lisans, Makina Mühendisliği
Tez Yöneticisi: Prof. Dr. Mehmet Halûk Aksel

Şubat 2022, 121 sayfa

Sesüstü hızlarda seyreden hava araçlarının hava alıklarından giren havanın yanma odasına istenen özelliklerde ulaşabilmesi hava alıklarının özel geometrik yapılara sahip olmasıyla sağlanır. Bu geometrik yapıların tasarımında kullanılan iki boyutlu ses üstü akış çözümü, hava alıklarının duvarlarının asimetrik veya akışın üç boyutlu özellikte olduğu koşullarda doğruluktan uzaklaşmaktadır. Bu sorunun giderilmesi, şok düzlemlerinin birbirleriyle olan etkileşimlerinin analitik yöntemlerle çözümlenmesi yoluyla sağlanabilir. Bu çalışmada, problemin analitik yöntemlerle çözümü için gaz dinamiği ilkelerinden yola çıkılarak bir çözüm modeli oluşturulacak ve oluşturulan çözüm modelinin doğrulaması mevcut deneysel veriyle ve hesaplamalı akışkanlar dinamiği araçlarıyla yapılacaktır. Bu sayede; çözümleme süresi kısaltılacak ve prototipleme-test maliyetleri azaltılacaktır.

Anahtar Kelimeler: Üç boyutlu şok-şok etkileşimleri, Sesüstü köşe akışı, Akış alanı, Analitik yöntemler, Mach yansımaları

To my family and humankind

ACKNOWLEDGMENTS

I would like to express my deepest gratitude to my thesis supervisor Prof. Dr. Mehmet Halûk Aksel for his guidance, advice, criticism, and insight throughout the research.

I would like to thank my beloved wife, Özge. Without her support and understanding, this work could not be finished. I also should remember my family. I am always inspired by their patience and love.

Lastly, I would like to present my appreciation to my colleagues from Roketsan for their friendship. They impressed me with their attitude and backed me up when I had to be absent from work.

This research, including the graduate education period, is financially supported by Roketsan.

TABLE OF CONTENTS

ABSTRACT	v
ÖZ	vi
ACKNOWLEDGMENTS	viii
TABLE OF CONTENTS.....	ix
LIST OF TABLES	xii
LIST OF FIGURES	xiii
LIST OF ABBREVIATIONS	xvii
LIST OF SYMBOLS	xviii
CHAPTERS	
1 INTRODUCTION	1
1.1 Analytical Methods	2
1.2 Numerical Methods	2
1.3 Experimental Methods	2
1.4 Outline and Objective.....	4
2 LITERATURE REVIEW	5
2.1 Types of and General Properties for Reflections	5
2.2 The Transition of Reflection Types	7
2.3 Importance of Reflection Types	11
2.4 Flow Field Determination for Three-Dimensional SSI.....	11
2.4.1 Experimental Work	12
2.4.2 Numerical Work.....	18
2.4.3 Analytical Work	19

3	SOLUTION	21
3.1	Assumptions.....	21
3.2	Description of Solution Domain	22
3.3	Description of Analytical Solution Technique	23
3.3.1	Finding the Wedge and Characteristic Directions	23
3.3.2	Determination of Interaction Type via Shock Polars	28
3.3.3	Calculation of Mach Number of Stem and Related Angles	34
3.3.4	Calculations for Plane of Investigation	41
3.4	Numerical Solutions	44
3.4.1	Geometry Preparation.....	44
3.4.2	Meshing	45
3.4.3	Solver.....	46
3.4.3.1	Material Model.....	46
3.4.3.2	Boundary Conditions	46
3.4.3.3	Solver Settings	47
3.4.3.4	Mesh Adaptation	49
3.4.3.5	Demonstration of Results of Numerical Solutions.....	51
3.5	Computer Source and Solution Durations	52
4	RESULTS AND DISCUSSIONS	53
4.1	Comparison of Flow Fields.....	54
4.1.1	Comparison of Flow Field with Experimental Data.....	54
4.1.2	Comparison of Flow Field with Numerical Results	57
4.1.3	Comparison of Flow Field with Analytical Results	70
4.2	Pressure Ratios Across Mach Stem	71

4.3	Discussion of Results	74
5	CONCLUSION AND FURTHER WORK.....	81
	REFERENCES	83
	APPENDICES	
A.	Sample Calculations for Analytical Solutions	87
B.	Shock Polar Diagrams for Solutions.....	100
C.	Pressure Ratios Along Calculation Lines	107
D.	Velocity and Pressure Contours from Numerical Solutions	115

LIST OF TABLES

TABLES

Table 1.1 Comparison of solution methods for SSI	3
Table 3.1 Material properties	46
Table 3.2 Computer source.....	52
Table 4.1 Flow and geometrical parameters.....	53
Table 4.2 Comparison of pressure ratios across Mach stem	73
Table 4.3 Limits of wedge angles for RR formation.....	76
Table 4.4 Comparison of slip line angles found by different equations.....	78

LIST OF FIGURES

FIGURES

Figure 2.1. Schematic illustration for a RR	5
Figure 2.2. Schematic illustration for an MR	6
Figure 2.3. Demonstration of RR (a) and MR (b) with shock polar curves.....	10
Figure 2.4. Flow structures for Mach 3.17 and symmetrical wedge angles at 12.2^0 for laminar flow / adapted from [14]	13
Figure 2.5. Flow structures for Mach 3 and symmetrical wedge angles at 9.5^0 for turbulent flow / adapted from [17].....	16
Figure 2.6. Flow structures for Mach 3 and symmetrical wedge angles at 9.5^0 for both laminar and turbulent flows / adapted from [17]	17
Figure 3.1. Solution domain with geometrical and characteristic parameters	23
Figure 3.2. Demonstration of velocity components on characteristic plane.....	27
Figure 3.3. Demonstration of flow deflection angles on characteristic plane.....	29
Figure 3.4. Shock polar curves (a) for flow parameters (b).....	32
Figure 3.5. Numerical results based on flow parameters in Figure 3.4 b).....	32
Figure 3.6. Shock polar curves (a) for flow parameters (b).....	33
Figure 3.7. Numerical results based on flow parameters in Figure 3.6 b).....	33
Figure 3.8. Demonstration of the Galilean transformation	35
Figure 3.9. Demonstration of diffraction of a shock by a wedge.....	37
Figure 3.10. Demonstration of moving shock wave problem.....	38
Figure 3.11. Demonstration of results on the plane of investigation	42
Figure 3.12. Demonstration of geometry a) and mesh b)	45
Figure 3.13. Demonstration of boundary condition on geometry	47
Figure 3.14. Demonstration of final mesh / inlet and symmetry regions hidden....	50
Figure 3.15. Demonstration of final mesh for outlet region	50
Figure 3.16. Demonstration of calculation line for pressure ratio	51
Figure 4.1. Comparison of analytical and experimental result for Case Ref. [17] .	55
Figure 4.2. Comparison of analytical and experimental results for Case Ref. [14]	56

Figure 4.3. Comparison of analytical and numerical results for Case Ref. [17]	57
Figure 4.4. Comparison of analytical and numerical results for Case Ref. [14]	58
Figure 4.5. Comparison of analytical and numerical results for Case A.....	59
Figure 4.6. Comparison of analytical and numerical results for Case B	60
Figure 4.7. Comparison of analytical and numerical results for Case C	61
Figure 4.8. Comparison of analytical and numerical results for Case D.....	62
Figure 4.9. Comparison of analytical and numerical results for Case E	63
Figure 4.10. Comparison of analytical and numerical results for Case F	64
Figure 4.11. Comparison of analytical and numerical results for Case G.....	65
Figure 4.12. Comparison of analytical and numerical results for Case H.....	66
Figure 4.13. Comparison of analytical and numerical results for Case I	67
Figure 4.14. Comparison of analytical and numerical results for Case J	68
Figure 4.15. Comparison of analytical and numerical results for Case K.....	69
Figure 4.16. Comparison of analytical results for Case Ref. [17]	71
Figure 4.17. Maximum symmetrical wedge angle for RR / adapted from [21]	76
Figure 5.1. Screenshot of analytical solution procedure / 1	88
Figure 5.2. Screenshot of analytical solution procedure / 2	89
Figure 5.3. Screenshot of analytical solution procedure / 3	90
Figure 5.4. Screenshot of analytical solution procedure / 4	91
Figure 5.5. Screenshot of analytical solution procedure / 5	92
Figure 5.6. Screenshot of analytical solution procedure / 6	93
Figure 5.7. Screenshot of analytical solution procedure / 7	94
Figure 5.8. Screenshot of analytical solution procedure / 8	95
Figure 5.9. Screenshot of analytical solution procedure / 9	96
Figure 5.10. Screenshot of analytical solution procedure / 10	97
Figure 5.11. Screenshot of analytical solution procedure / 11	98
Figure 5.12. Screenshot of analytical solution procedure / 12	99
Figure 5.13. Shock polar curves for Case Ref. [17]	100
Figure 5.14. Shock polar curves for Case Ref. [14]	101
Figure 5.15. Shock polar curves for Case A.....	101

Figure 5.16. Shock polar curves for Case B	102
Figure 5.17. Shock polar curves for Case C	102
Figure 5.18. Shock polar curves for Case D	103
Figure 5.19. Shock polar curves for Case E.....	103
Figure 5.20. Shock polar curves for Case F.....	104
Figure 5.21. Shock polar curves for Case G	104
Figure 5.22. Shock polar curves for Case H	105
Figure 5.23. Shock polar curves for Case I.....	105
Figure 5.24. Shock polar curves for Case J	106
Figure 5.25. Shock polar curves for Case K	106
Figure 5.26. Pressure ratios for Case Ref. [17]	107
Figure 5.27. Pressure ratios for Case Ref. [14]	108
Figure 5.28. Pressure ratios for Case A	108
Figure 5.29. Pressure ratios for Case B.....	109
Figure 5.30. Pressure ratios for Case C.....	109
Figure 5.31. Pressure ratios for Case D	110
Figure 5.32. Pressure ratios for Case E.....	110
Figure 5.33. Pressure ratios for Case F.....	111
Figure 5.34. Pressure ratios for Case G	111
Figure 5.35. Pressure ratios for Case H	112
Figure 5.36. Pressure ratios for Case I	112
Figure 5.37. Pressure ratios for Case J	113
Figure 5.38. Pressure ratios for Case K	113
Figure 5.39. Contours of Case Ref. [17] for Mach number (a) and pressure (b)..	115
Figure 5.40. Contours of Case Ref. [14] for Mach number (a) and pressure (b)..	116
Figure 5.41. Contours of Case A for Mach number (a) and pressure (b)	116
Figure 5.42. Contours of Case B for Mach number (a) and pressure (b).....	117
Figure 5.43. Contours of Case C for Mach number (a) and pressure (b).....	117
Figure 5.44. Contours of Case D for Mach number (a) and pressure (b)	118
Figure 5.45. Contours of Case E for Mach number (a) and pressure (b).....	118

Figure 5.46. Contours of Case F for Mach number (a) and pressure (b)	119
Figure 5.47. Contours of Case G for Mach number (a) and pressure (b).....	119
Figure 5.48. Contours of Case H for Mach number (a) and pressure (b).....	120
Figure 5.49. Contours of Case I for Mach number (a) and pressure (b)	120
Figure 5.50. Contours of Case J for Mach number (a) and pressure (b)	121
Figure 5.51. Contours of Case K for Mach number (a) and pressure (b).....	121

LIST OF ABBREVIATIONS

ABBREVIATIONS

SSI	:	Shock-shock interaction
RR	:	Regular reflection
MR	:	Mach reflection
Re	:	Reynolds number
3D	:	Three dimensional
2D	:	Two dimensional
CFD	:	Computational fluid dynamics
i	:	Incident
r	:	Reflected
GUI	:	Graphical user interface
M	:	Mach number
MPI	:	Message passing interface
An.	:	Analytical
Num.	:	Numerical
Exp.	:	Experimental

LIST OF SYMBOLS

SYMBOLS

θ_1, θ_2	: Wedge angle of the first and second wedge
λ_1, λ_2	: Sweep angle of the first and second wedge
ν	: Dihedral angle
β_1, β_2	: Shock angle of the first and second wedge
η	: The angle between first and second wedges on characteristic plane
α_1, α_2	: The angle between the resultant velocity vector and first and second wedges on the characteristic plane
δ_1, δ_2	: Shock wave angles for first and second shock waves on characteristic plane
χ_1, χ_2	: The angle between Mach stem moving direction and first and second slip lines on the characteristic plane
θ_{w1}, θ_{w2}	: The angle between Mach stem moving direction and first and second shock wave moving directions on the characteristic plane
ζ	: Pressure ratio
.	: Dot product
\times	: Cross product
$ R $: Resultant of vector R

CHAPTER 1

INTRODUCTION

Propulsion systems can be categorized into two groups according to their fuel-burning mechanisms. Rocket motors generally have their fuel and its oxidizer in their fuel tanks, so they do not need any input from the outside atmosphere. Such systems are members of the first group. In the second group, only fuel is carried in the system and the oxidizer (i.e., air) is taken from the outer environment. The second group may also be called air-breathing systems. Turbofans and ramjets are examples of such propulsion systems. The former group has the advantage of integrity when the combustion process is considered. The latter group, on the other hand, generally has less mass since it can supply one of two combustion inputs from its outer space.

Some air-breathing systems have tunnels to provide air to combustion systems which are called air ducts. Air ducts are specially designed to decrease pressure losses since the efficiency and completeness of the combustion in the chamber are mainly determined by the properties of the incoming air.

The seek for higher cruise speeds for air systems forces them to travel at supersonic speeds. As the speed of systems approaches the speed of sound, shock waves begin to form. A shock wave causes abrupt changes in flow properties such as total pressure loss and temperature increase.

The formation of shock waves is inevitable during a supersonic cruise and becomes critically important when they occur around and inside air ducts. Different than their occurrence in external flow conditions, shock waves reflect from surfaces and interact with each other. Therefore, the reflection and interaction phenomena of shock waves should be well understood as it is not only important for having better control of the combustion process of propulsion systems, but also for keeping the system away from being mechanically damaged by overheating or excessive pressure loads.

Reflection and interaction of shock waves may be examined by several techniques. These techniques are divided into three following methods; analytical, numerical, and experimental.

1.1 Analytical Methods

Analytical methods are based on gas dynamics equations. Despite having easier solutions, they are, in general, only applicable to two-dimensional problems with their usual forms. Their solutions demand little or no computing sources, therefore, the cost of application of analytical methods is low.

1.2 Numerical Methods

Numerical methods imply finite difference, finite volume, or finite element analysis and are performed by numerically solving Euler or Navier-Stokes equations. Since the flow field is divided into solution volumes, no geometrical limits are defined, thus they are applicable for different boundary conditions. In numerical methods, the effects of different flow physics may be investigated. For instance, viscous effects and time dependency of the flow field can be studied by comparing the solutions. On the other hand, shock waves are assumed to have an infinitesimally small thickness since they are very thin in structure. To capture the flow properties across a shock wave adequately, special techniques, such as mesh adaptation based on flow gradients, should be applied. The cost of application of numerical solutions is considerable since numerical methods require medium or high computing sources depending on the type of solution carried out and the required accuracy.

1.3 Experimental Methods

Experimental methods give the most comprehensive results for the problem when compared with other solution methods. Hence, they offer a complete result for the

problem investigated. Nevertheless, they require carefully selected (or designed) measurement equipment, a detailed testing plan, a suitable testing facility, and highly skilled labor. Experiments including shock waves are generally carried out in shock tubes or wind tunnels which have high running costs. Therefore, the cost of application for experimental methods is enormous. In addition, not every possible configuration may be experimentally investigated due to the limitations of testing facilities i.e., testing time or airflow speed. Thus, the applicability of the related solution method for different boundary conditions is intermediate.

Solution methods are compared concerning their applicability for different boundary conditions, cost of application, and completeness of solution in Table 1.1.

Table 1.1 Comparison of solution methods for SSI

Criteria	Solution methods		
	Analytical	Numerical	Experimental
Applicability for different boundary conditions	Low	High	Medium
Cost of application	Low	Medium	High
Completeness of solution	Low	Medium	High

It can be predicted that increasing the complexity of the solution by introducing all possible flow physics would result in numerical methods that may produce closer outcomes to experimental methods. Yet, the same comment cannot be made for analytical methods since their main deficiency is the lack of a three-dimensional (3D) approach to Shock-shock Interaction (SSI) problems.

1.4 Outline and Objective

In this work, an analytical approach is sought to study the 3D SSI problem for steady corner flows. Related literature findings are presented and commented on. The solution procedure is based on shock polar diagrams and the “spatial-dimension reduction” technique. This technique has been developed and used in the solution of similar problems by several researchers which are mentioned in related sections. The solution procedure is presented in four major steps and every step is explained in detail. Assumptions and solution theory for analytical solutions are also provided. Schemes and approaches used in numerical solutions are expressed with available computing sources. Flow fields for both symmetrically and asymmetrically intersecting wedges with different geometrical parameters are calculated using the presented analytical approach. Results are compared with existing experimental data available in the literature, numerical results that have been realized for this work, and analytical results obtained by different researchers by using the same analytical solution technique. The comparison is made in both qualitative and quantitative manners. Flow fields are compared qualitatively by positions for incident shock waves, Mach stems, and slip lines. Quantitative comparisons are made for shock strength around Mach stems by pressure ratio. Deviations from numerical, experimental, and analytical data are evaluated and discussed. The study is concluded and future work is listed following the findings of the presented study. More details for the analytical solution are presented in Appendices such as the introduction of software coding, screenshots of analytical solutions from software Graphical User Interface (GUI), shock polar diagrams, pressure ratios along the calculation lines, and velocity / pressure contours from numerical results of cases studied.

CHAPTER 2

LITERATURE REVIEW

2.1 Types of and General Properties for Reflections

When a shock wave encounters a medium that has a different acoustic impedance than the one it travels, it reflects from the boundary of the medium. This reflection is known as shock wave reflection. In general, shock wave reflections can be categorized as regular and irregular reflections. Irregular reflections are also named Mach reflections [1, p. 3].

A schematic illustration for a regular reflection (RR) is given in Figure 2.1. RR is characterized by two shock waves (i for incident and r for reflected) intersecting with the surface at point R. Flow field can be investigated in three zones (0, 1, and 2). Undisturbed flow M_0 experiences two oblique shock waves (i and r). Flow at zone 0 is parallel to flow at zone 2.

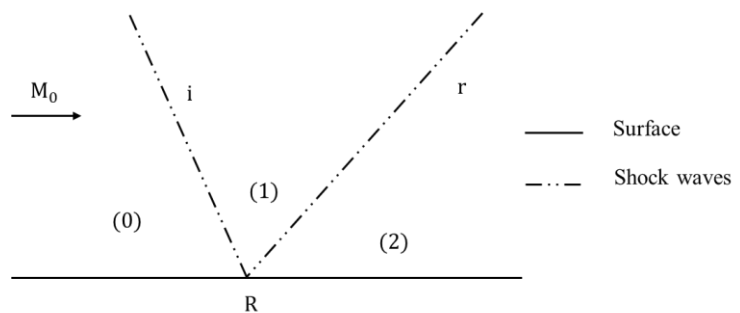


Figure 2.1. Schematic illustration for a RR

RR can be solved by using conservation (continuity, momentum, and energy) equations written for two shock waves and using the parallelism of flow directions in regions 0 and 2 [1, p. 15]. Alternatively, oblique shock relations can be used with parallelism of flow for the solution of RR.

A schematic illustration for an MR (Mach reflection) is given in Figure 2.2. There are three shock waves (i for incident, r for reflected, and m for Mach stem) intersecting at point T. Different from RR, a slip line (shown with s) exists in MR, and the flow field is divided into four regions (0, 1, 2 and 3). Instead of point R which is located on the surface, discontinuities intersect at point T. Point T is also known as triple point. The flow above point T experiences two oblique shock waves (i and r), whereas below point T encounters one normal shock wave (m). Across the slip line; s, the flow has the same pressure and direction. Flow does not change its direction along the wedge surface. However, the direction of flow along the slip line may or may not be parallel to the undisturbed direction.

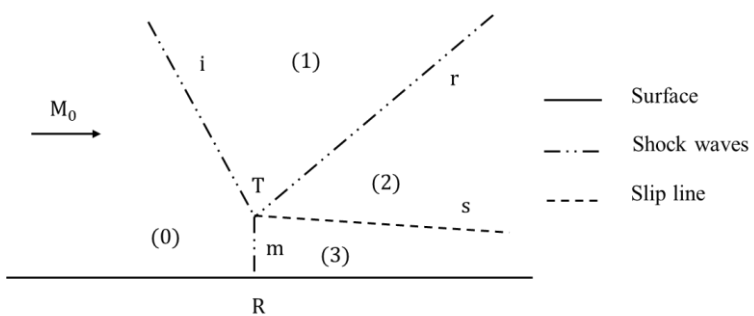


Figure 2.2. Schematic illustration for an MR

Like RR, MR can be formulated by using conservation equations written across three shock waves, equality of pressures, and parallelism of flow direction around slip line (regions 2 and 3) [1, p. 16]. However, it is stated that solving this equation set does not yield a unique solution and is not sufficient to determine the complete flow field [1, p. 18].

The Mach reflections can be divided into several subgroups concerning the trajectory of the triple point of T. A complete table for types of shock wave reflections was given in [1, p. 9]. It should also be emphasized that some reflection types can only be detected in certain time dependency conditions. According to time dependency, reflections are categorized into three; steady, pseudo-steady, and unsteady.

As already discussed, different types of reflections have distinguishable features which determine the flow field structures. However, the solution methods provided for reflection types do not indicate up to which point the reflection would be a regular type. This point, the lack of information on when a reflection changes its type, opens a gate through a very challenging research area of gas dynamics which is the specification of transition criteria.

2.2 The Transition of Reflection Types

From the early 1940s to the present, plenty of research has been done on the determination of transition criteria between RR and MR. For two-dimensional flows, a very comprehensive summary of this phenomenon was given in [1, pp. 25-36].

Four major criteria were suggested for transition phenomena. The first one is named “the detachment criterion”. According to this, the transition should occur from RR to MR if the reflected shock wave’s maximum deflection angle is less than the flow turning angle. A similar criterion for transition was defined as “the sonic criterion”. This criterion assumes that flow can turn up to its sonic point (i.e., flow after reflected shock wave is sonic). It should be noted that the difference between the detachment and the sonic criteria is only a small fraction of a degree [1, p. 31], therefore they can be considered as practically the same criterion. Thirdly, “the mechanical equilibrium condition” necessitates that the pressure behind the reflected shock wave is equal to the pressure behind the normal incident shock wave. In other words, no sudden pressure change should be expected during the transition (which was the case with detachment criterion for some cases) since no compression or expansion waves were

ever observed in experiments [1, p. 30]. This criterion is more likely named “the von Neumann criterion”. This is one of the most widely used conditions together with the detachment criteria. Finally, the length-scale criterion was introduced by Hornung et al [2].

Solutions that were made for von Neumann and detachment criterion indicate that there is a region at which RR and MR are theoretically possible. This region is called the dual-solution domain. Studies showed that different criterion for transition holds for different conditions such as the transition direction (from RR to MR, or the opposite way), time dependency (steady, pseudo-steady, and unsteady), and disturbance level in the test environment [2, 3, 4, 5, 6, 7, 8].

Kawamura and Saito [9] examined the reflection problem by using shock-polar diagrams in the hodograph plane. They stated that as the incoming flow is deflected by an incident shock, the pressure of the flow is increased as a function of the wedge angle that creates the incident shock. Instead of defining the shock polar diagram as a function of wedge and shock angles, they proposed to define it by using the pressure ratio and the wedge angles. Expressing the problem in terms of pressure ratio and wedge angles directly connected the flow parameters to geometrical variations. It should also be noted that pressure ratio and parallelism of flow directions were boundary conditions for the solution of RR and MR. As a result, boundary conditions could directly be found from shock-polar diagrams and a better understanding of shock wave reflection could be obtained by visualization of the problem.

Procedure for defining the shock polar curves and their explanations are as follows:

1- Formation of polar diagram for an incident shock: This curve is prepared by finding all pressure ratio solutions for possible wedge (i.e., deflection) angles by using oblique shock relations. Mach number and ratio of specific heats of upstream flow are two independent variables of these relations. So, different mediums and/or Mach numbers indicate different curves. Oblique shock equations are valid until shock wave separates from wedge (i.e., bow

shock occurs). Therefore, the wedge deflection limit is determined by this “maximum turning point” criteria. It should be noted that for a selected deflection angle, two possible solutions exist, which are called weak and strong shock solutions.

If wedge angle is known, pressure ratio can be found by reading the corresponding pressure ratio value from the shock polar curve. Mach number of flow after incident shock wave can be found by using the above-mentioned oblique shock relations, also.

- 2- ***Formation of polar diagram for a reflected shock:*** Reflected shock polar curve can be prepared by using the information and remarks given for incident shock. Two main differences must be emphasized. Firstly, the starting point of the reflected shock polar should be placed on the corresponding deflection angle defined for the incident shock polar curve. As it is more possible to occur, the weak shock (i.e., lower pressure ratio) solution should be taken as the origin. This pressure ratio value is also a multiplier when the shock polar curve for reflected shock is being formed. Secondly, the Mach number found for the flow after the incident shock wave should be used when solutions for oblique shock relations are obtained.
- 3- ***Determination of reflection type by using shock polar curves:*** Polar curves for the incident and reflected shocks for known Mach numbers are plotted together (on the same graph). If the reflected shock polar crosses the ordinate (pressure ratio) axis, the reflection type is RR. The intersection of the reflected shock polar curve with the pressure ratio axis indicates that flow can be deflected up to its initial direction. If the reflected shock polar does not cross the pressure ratio axis, the reflection type is MR. This situation demonstrates that the flow after the reflected shock cannot be turned up to its upstream direction. As a result, a new region (zone 3 in Figure 2.2) occurs, whose borders are the wedge surface, a slip line, and a normal shock wave. This normal shock wave is also called Mach stem.

Two shock polar diagrams prepared for RR and MR can be seen in Figure 2.3. For the RR case, pressure ratios are around 3 and 6.5 for zones 1 and 2. For the MR case, pressure ratios are approximately 4.5 for zone 1 and 10.5 for zones 2 and 3. For RR, the flow direction in zone 2 is parallel to zone 0. For MR, however, flow in zone 3 is only parallel to the upstream flow on the wedge surface. Incident and reflected shock polar diagrams intersect at a point with a positive deflection angle. This intersection point determines the angle of the slip line to the upstream flow and its value can be read from the shock polar diagrams. Hence, an approximately 10^0 deviation from the upstream flow should be expected along the slip line.

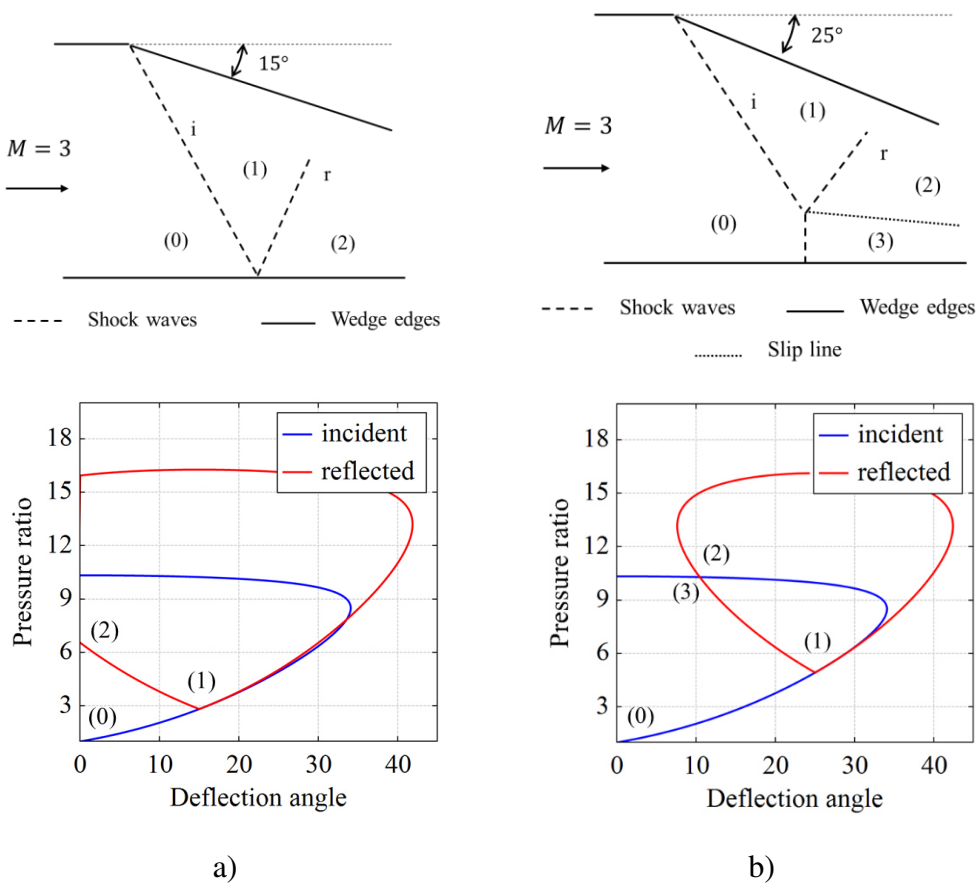


Figure 2.3. Demonstration of RR (a) and MR (b) with shock polar curves

2.3 Importance of Reflection Types

As already underlined, for supersonic flights, the correct estimations of flow properties have critical importance. Reflection of shock waves is one of the main investigation areas on this topic as different types of shock wave reflections alter the pressure and temperature in the flow field abruptly. These sudden changes can result in unexpected situations. For instance, the formation of normal shock (i.e., Mach stem) creates higher total pressure losses and can create unchoked (subsonic) flow in ramjet air ducts. This situation can result in an “unstart” problem which was investigated in [10]. Another extreme condition happens when a detached shock wave intersects with an oblique shock. This interaction creates an MR and causes abnormally high heat transfer rates on surfaces. This subject was studied in [11, 12]. Although these examples might be considered as different, both of the situations can only be controlled by having a better understanding of the reflection phenomena of the shock waves. It should also be emphasized that internal flow conditions are more susceptible to both of the adverse outcomes of the above-mentioned abnormalities as a series of shock wave reflection and / or interaction incidents will inevitably occur which may amplify the unfavorable results.

2.4 Flow Field Determination for Three-Dimensional SSI

Reflection of shock waves can successfully be studied by using both of the available solution methods if the flow field can be treated in two dimensions. For example, oblique shocks are one of the most encountered wave structures in aeronautics. They may be investigated as three-dimensional structures due to the selection of coordinate systems based on other properties. However, the oblique shock waves are planar and could be handled as two-dimensional if a proper selection of coordinate systems is made. Nevertheless, such an approach applies only to a few limited cases such as two intersecting shock waves whose plane normals are orthogonal or the existence of only a single oblique shock wave. Such conditions may be observed

very rarely. On the contrary, almost always three-dimensional interaction of shock waves is expected in real flights when the maneuvers of an aircraft during its cruise are considered.

Three-dimensional reflection and interaction problems can be separated as external and internal problems. In addition to works given in [11] and [12], an example of an external flow problem is the investigation of flow properties around a rudder of a hypersonic air vehicle given in [13]. Internal problems, on the other hand, define the flow travels in a close conduit whose properties are predominantly determined by interactions of oblique shock waves. These kinds of flow structures are generally observed in rectangular-shaped tunnels such as air ducts. It is also common to study this problem as a corner flow problem since the flow structures on a corner repeat themselves for other corners, too. In other words, the overall properties of a supersonic flow in a close conduit can be estimated by using the flow properties calculated around a corner. Therefore, they are also defined as corner flow problems.

As already mentioned and discussed in previous sections, the solution of the internal supersonic corner flow problem with analytical methods is the objective of this study. Therefore, the scope of the literature survey is limited to the solutions to this problem. The remarkable studies done for corner flow problems are summarized in the following sections.

2.4.1 Experimental Work

Four experimental studies are selected to be presented and explained in detail considering their importance and association with this study. The results of two of the experiments are also used in this study for comparison purposes.

Charwat and Redekeopp [14] performed a set of experiments to investigate the supersonic flow field in the vicinity of a corner formed by two intersecting wedges. Pressure measurement and oil flow photographs were used by researchers for this study. Static pressure data was measured on wedge surfaces and total pressure data

was determined by a fine impact probe which traversed on a plane at a 1-inch distance from the leading edge. By using the pressure data obtained from the traversing pressure probe, the flow field was reconstructed, and wave pattern was demonstrated. Oil flow visualizations were presented to determine compression, expansion, and separation regions on wedge surfaces. Mach number, the asymmetrical intersection of wedges, and dihedral angle effects were investigated. It should be underlined that the boundary layer was always laminar in all experiments. The most detailed explanation was given for the case of Mach number 3.17 and the symmetrical intersection of wedges at 12.2^0 and given in Figure 2.4.

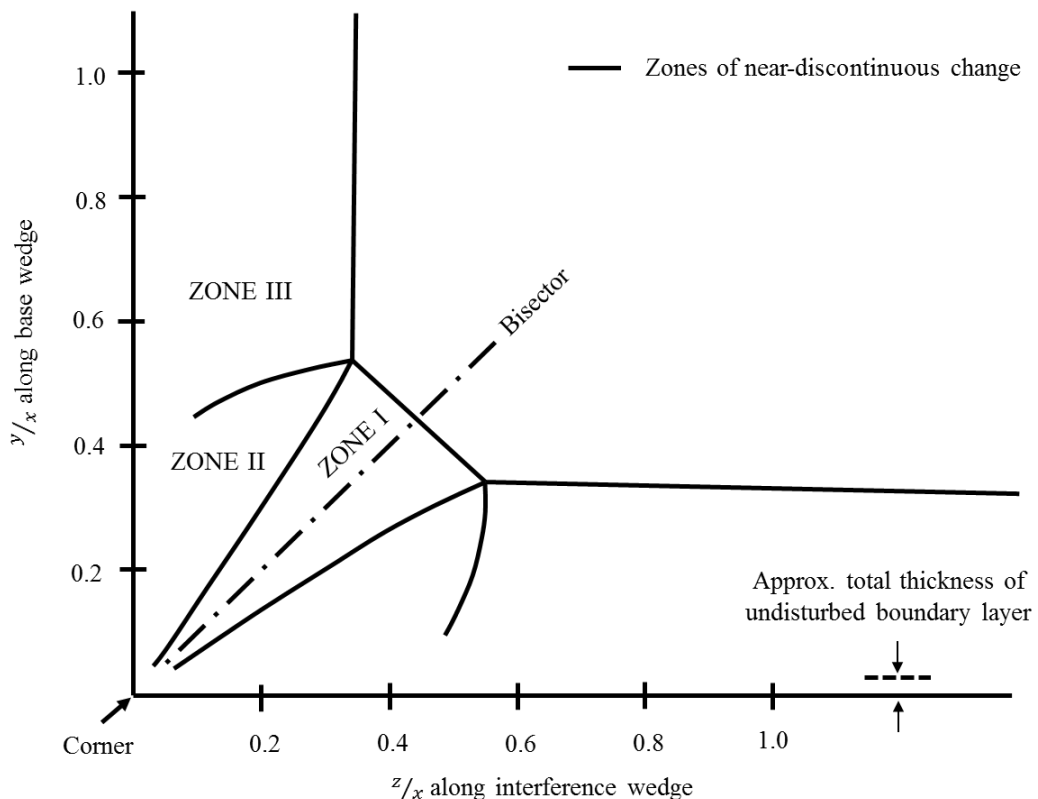


Figure 2.4. Flow structures for Mach 3.17 and symmetrical wedge angles at 12.2^0
for laminar flow / adapted from [14]

By following the outcome of their work, Charwat and Redekeopp stated that the flow field could be defined under several principal regions, and despite being distorted, these principal regions could be identified in all experiments. Therefore, it was said that “the characteristic skeleton wave structure” [14, p. 488] of the flow field was captured and this structure was found to be qualitatively similar in all experiments. Another significant conclusion of the work was the indication of a vorticity gradient caused by entropy waves (i.e., slip surfaces). Researchers emphasized that for a realistic analysis of the corner flow problem, this phenomenon should not be disregarded.

Cresci et al [15] conducted experimental and numerical work to study the flow field in the region of interaction of corner flow. Wedge angles were kept at 0^0 (i.e., flat plate) for a freestream Mach number of 11.2. This configuration of wedges created a flow condition with no deflection in the flow field and shock waves with an angle equal to the Mach angle of the flow. Flow structures were defined as pressure contours by using the data gathered from Pitot pressure readings. It can be concluded that flow structures in the corner regions resembled the data obtained from other experimental work [14, 16, 17] despite not having detailed information and comments as others. Numerical investigations were also done and explained in upcoming sections.

Watson and Weinstein [16] investigated the characteristics of the flow fields over two symmetrical wedges with different angles (0^0 , 5^0 , and 10^0) forming corner flow conditions. The medium was chosen as Helium and Mach number was selected as 20. The flow field was visualized by following Pitot pressure traces, oil flow photographs from wedge surfaces, and surface pressure distributions were presented. They compared their results with the findings of [14] and concluded that the same flow features were observed in both. Despite its similarity, they emphasized that the flow field was found to be distorted because of two reasons. The first reason was pointed out to be the higher Mach number which was 3.17 in [14]. As Mach number of flow increases, shock angles become smaller for a known wedge angle. As a

result, the interaction of shock waves occurs closer to wedge surfaces. In such a case, boundary layer thicknesses become comparable with shock wave distances from surfaces. Therefore, the displacement of boundary layers affects the shock wave structure. The second reason was underlined as the formation of large vortices. Indeed, Watson and Weinstein successfully proved this hypothesis with oil-flow and electron-beam photographs. Vortex formations were observed at regions where reflected shock waves intersect with the wedge surfaces and the strength of vortices was found to be increased as wedge angle and Mach number increased.

West and Korkegi [17] studied the problem of supersonic interaction in the corner regions. Like previous works, to visualize and reconstruct the flow field, oil flow studies and pressure measurements (both Pitot and surface) were conducted. Distinctly, the effects of Re (Reynolds) number on flow structures were studied. For flow conditions of different Re numbers, laminar, transitional, and turbulent regions were investigated with surface pressure and oil flow patterns. In turbulent flow conditions, boundary layer effects were expected to be minimized. Therefore, the inviscid structure of flow was supposed to be captured in fully developed turbulent flow conditions. Indeed, it was stated that for Re numbers in the range of $3 - 60 \times 10^6$, flow structures only changed at regions close to wedge surfaces and were found almost identical for the incident, reflected, and corner (i.e., Mach stem) shocks and shear layers (i.e., slip surfaces). This finding was also supported by the surface pressure data obtained for the same Re number range. The surface pressure readings also showed a very similar pressure distribution for all turbulent cases.

The flow structure was constructed by following the Pitot pressure data. At the construction of the flow field, approximate mid-points of regions with rapid pressure change were used. An adaptation of this flow field is given in Figure 2.5.

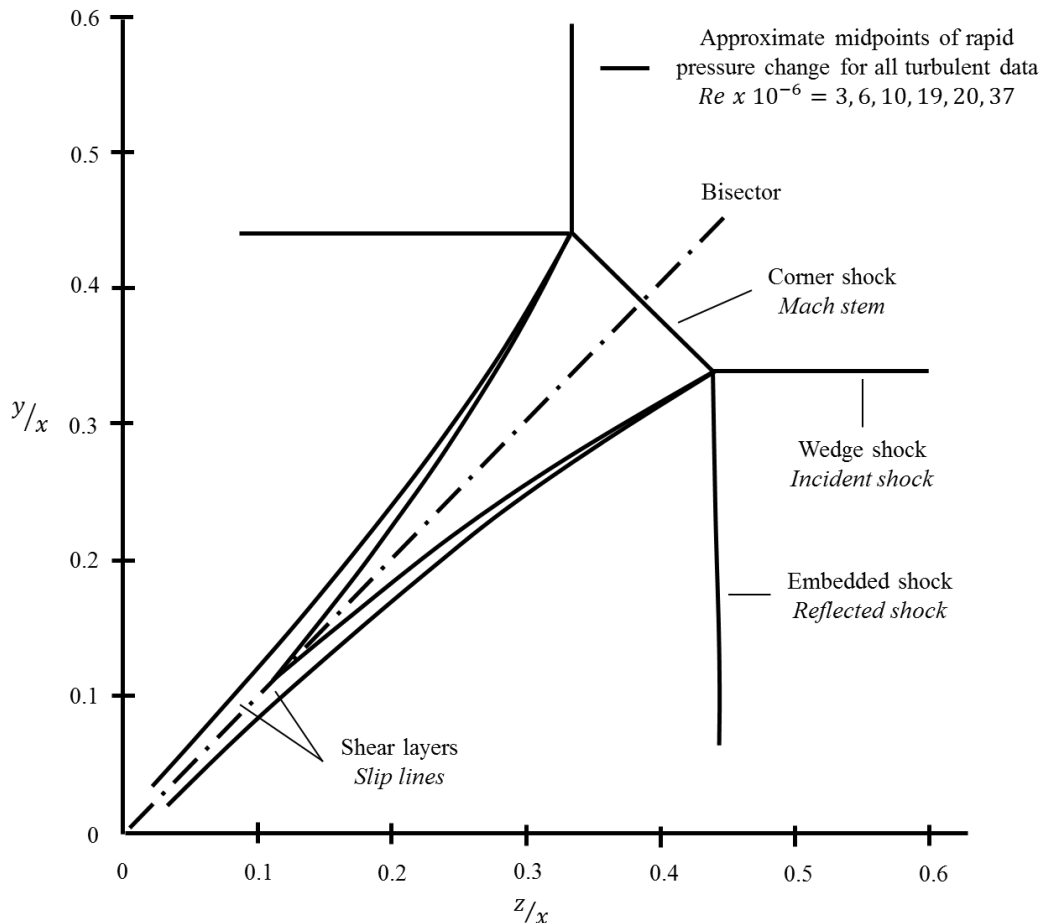


Figure 2.5. Flow structures for Mach 3 and symmetrical wedge angles at 9.5^0 for turbulent flow / adapted from [17]

By following the surface pressure measurements and flow field constructions, the authors concluded that for Re number higher than 3×10^6 flow structure was said to be “conically invariant and therefore represents the inviscid structure [17, p. 656]”. For Re number lower than 3×10^6 , on the other hand, researchers showed that surface pressure distribution changed significantly. This change was explained with laminar and/or transitional boundary layer formations. It was concluded that for Re number much below than 3×10^6 , viscous effects dominated the flow field. The authors also compared their results with the findings of [14] where the flow was completely

laminar. It was shown that flow fields were found similar for close Re numbers. However, as the Re number increased, incident and corner shock waves were found to be closer to wedge surfaces. This difference was emphasized to be clear proof of the existence of “significant viscous influences in the form of boundary-layer displacement effects and strong laminar viscous-inviscid interactions [17, p. 655]”. Figure 2.6 shows the comparison of flow structures of a particular laminar case with the turbulent structure.

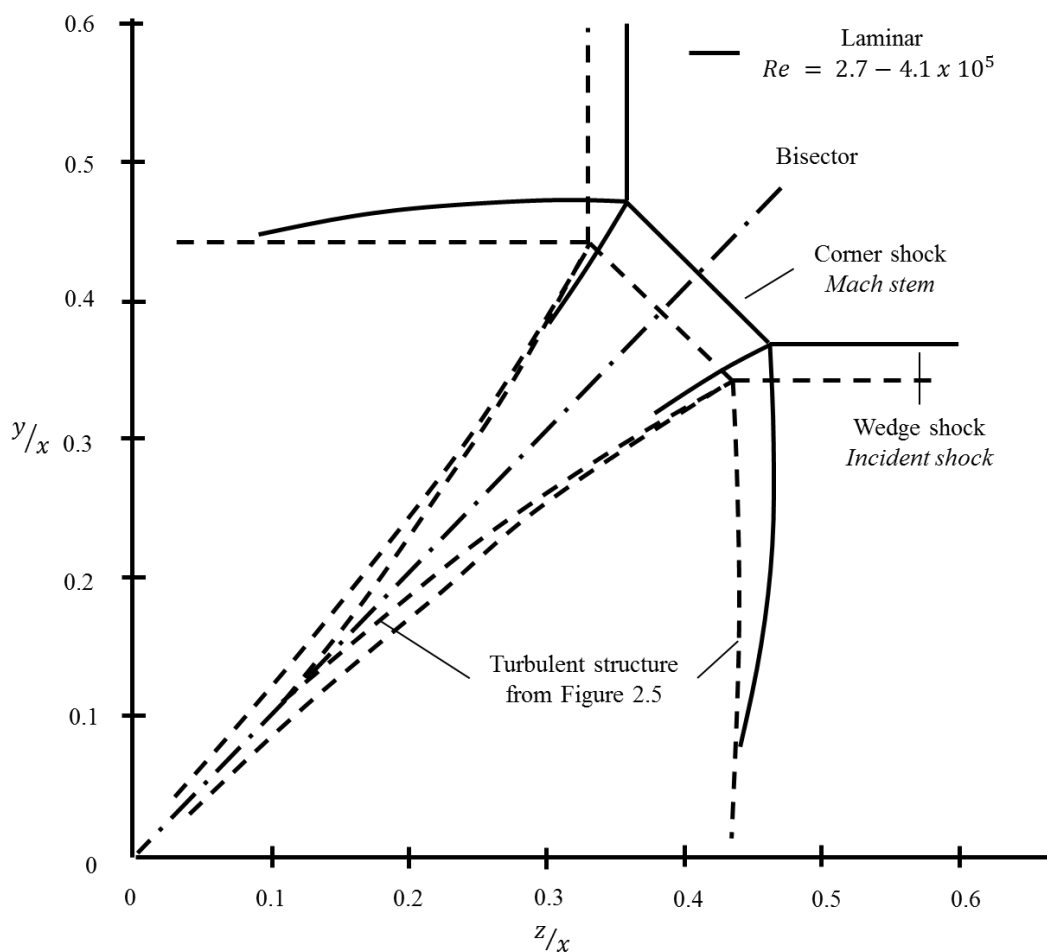


Figure 2.6. Flow structures for Mach 3 and symmetrical wedge angles at 9.5^0 for both laminar and turbulent flows / adapted from [17]

2.4.2 Numerical Work

As computer technology and computational fluid dynamics methods develop after the 1960s, numerical methods for the solution of corner flow were being used with increasing popularity.

As stated in the previous section, Cresci et al [15] executed a numerical study and showed its conformity with their experimental data. Their numerical solution method was based on [18] and solutions were obtained by an explicit finite difference calculation. Convergence criteria and mesh sizes were defined. Numerical solutions could not be continued for the distance at which experimental data exists because of long solution times. Pressure and temperature distributions, that were obtained numerically, were in close agreement with the experimental data. Thus, it was concluded that despite having “a relatively long time, this analysis is at present the only technique that can be satisfactorily used [15, p. 2246]” for such problems.

Kutler [19] conducted a numerical work by using a second-order accurate shock-capturing technique by using inviscid and steady flow assumptions which were explained in detail in [20]. Cartesian coordinates of space were transformed into “nonorthogonal, conical” coordinates by selecting the axial direction as the basis. This transformation made the conservation laws, which were expressed as partial differential equations, dimensionless and “totally hyperbolic”. Results of numerical solutions which were obtained for the case given in [17] were presented and compared with experimental data. He stated that numerical solutions represent the flow structures qualitatively although results for the slip line and embedded (reflected) shock deviated from experimental results. This deviation was said to be expected due to viscous effects which were not included in his numerical solution.

Marconi [21] developed a computational procedure for inviscid flow fields around internal corners. It was stated that a “computational procedure developed to predict conical, inviscid, supersonic corner flow field” and second-order, finite-difference marching technique was used in solutions. Details of the computational procedure

were given in [22]. As in similar works, experimental data obtained in [14] and [17] were used for comparison. The outcome of this work also showed that flow structures were found closer to high Re number experiments. Variations of geometrical parameters and inflow velocity were investigated.

Meguro et al [23] investigated the corner flow structure by both experimental and numerical methods. For numerical solutions, the Weighted Average Flux (WAF) method was stated to be applied to three-dimensional unsteady compressible Euler equations. Experiments were done for different wedge angles and numerical results were checked with experimental data. The flow was conditioned as unsteady (or pseudo-steady) with a moving shock wave and flow structures were captured with double-exposure diffuse holographic interferometry in experiments. Shapes of Mach stems occurred due to shock wave interactions were compared with visual results of experiments and a good agreement was observed.

Goonko et al [24] approached the corner flow problem with a focus on spatial interaction and studied the flow by solving three-dimensional steady Euler equations with the marching method. They discussed the effects of changing wedge, sweep, and dihedral angles. Different types of reflections (both RR and subtypes of MR) were shown in terms of velocity contours. They showed that the flow field becomes complicated and rare subtypes of MR were observed as Mach number and angles were increased.

2.4.3 Analytical Work

There is very limited analytical work done on the three-dimensional reflection and interaction field.

Azevedo and Liu [25, 26] proposed an analytical method to estimate the height of Mach stem for MR type reflections and compare their results with observations in the experimental work of Henderson and Lozzi [4]. They also performed a sensitivity analysis to show the possible reasons for the deviation of their results from

experimental outcomes. Although not being in the three-dimensional domain, their method was found remarkable to be mentioned

Yang et al developed an analytical approach [27, 28, 29, 30, 31] which is called “spatial-dimension reduction”. The idea behind this technique is to convert the three-dimensional steady SSI problem into a two-dimensional unsteady one. In other words, “one spatial dimension is handled as a temporal dimension [30, p. 312]”. For the implementation of their solution method, the characteristic direction should be determined based on the geometrical parameters and inflow velocity is to be projected onto characteristic planes. Solutions on characteristic planes which are normal to the characteristic direction can be carried out by using shock dynamics principles [32]. They compared their analytical results with the findings of [17]. In addition, they performed numerical solutions by solving 3D unsteady Euler equations and tested their analytical results with numerical ones. It was concluded that good agreement was observed with not only experimental data but also numerical results.

CHAPTER 3

SOLUTION

This chapter is devoted to the solution steps of the problem and presented under five main titles. The assumptions which are used at solutions (both numerical and analytical) are identified and discussed shortly. The geometrical properties that define the corner flow problem are demonstrated. Then, the analytical solutions are classified under four captions based on the successive solution steps. After, the numerical solution methodology followed in this work is explained. Finally, available computing sources together with approximate solution durations are described.

3.1 Assumptions

Based on findings from the literature review, assumptions below are made in this work:

- 1- Viscous effects are neglected. This assumption is coherent for two main reasons. Firstly, it was shown that above a certain Re number, characteristic flow features were the same. These non-changing structures were identified as a representation of the inviscid nature of the reflection in [17]. Secondly, in corner flow problems, flow is only laminar up to a certain Re number and this laminar or transitional region becomes smaller and less important as the speed of flight increases. So, the viscosity can be neglected for high-speed flows.
- 2- Ideal and perfect gas assumptions are made. This assumption should be made to find the state variables and to use the gas dynamics equations in the analytical solutions.

- 3- Unsteady effects are temporary and the performance of a system is understood better under steady-state conditions. Thus, no time dependency is modeled in analytical solutions. In other words, the corner flow problem is assumed to be steady.

3.2 Description of Solution Domain

A corner flow problem inherently necessitates two planes whose intersection can be defined with a line. The objective of the problem is to find the flow structures around the corner and geometrical definitions of the planes (i.e., wedges) directly determine the flow structure by changing the oblique shock waves which rise from the initial line (i.e., leading edge) of the wedge.

The geometry of the two intersecting wedges can be defined by using five angles if the angular position of one of the leading edges is selected as the basis. These angles have been named the wedge, sweep, and dihedral angles and are shown in Figure 3.1 with other characteristic parameters and vectors. It should also be mentioned that similar geometrical definitions are also common in literature. Resembling geometrical definitions may be seen in numerical and analytical studies mentioned in Section 2.4.2 as [21, 24] and in Section 2.4.3 as [27, 28, 29, 30, 31].

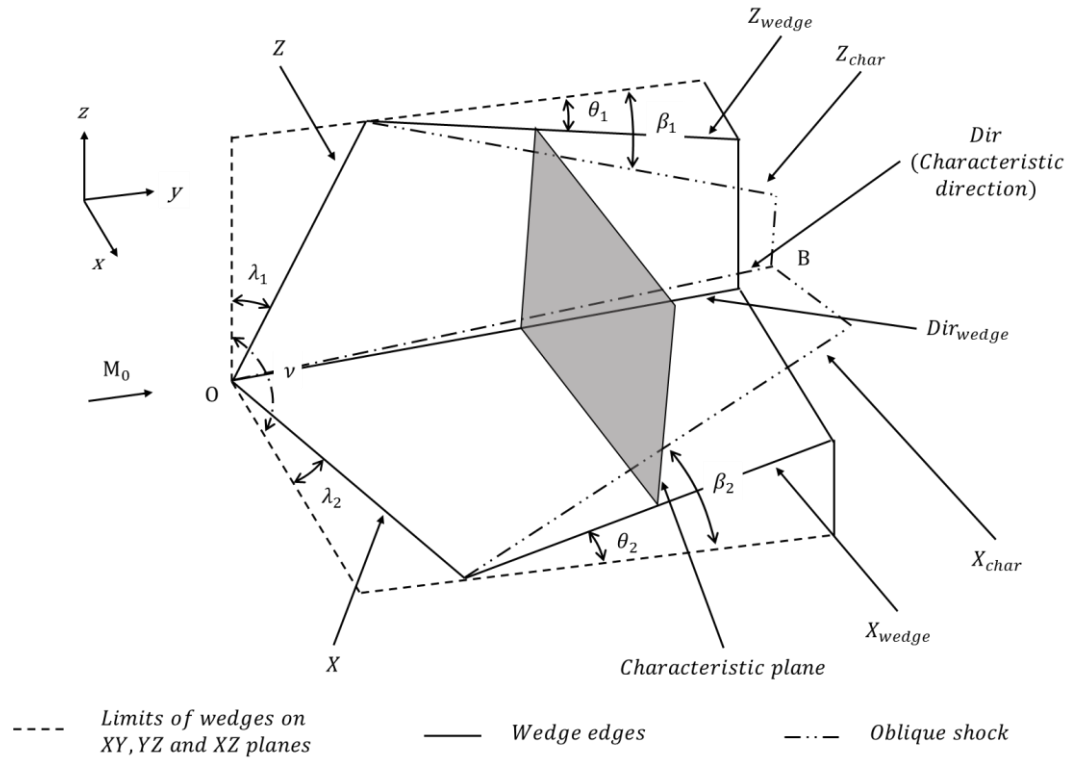


Figure 3.1. Solution domain with geometrical and characteristic parameters

3.3 Description of Analytical Solution Technique

In this work, an analytical solution technique based on the “spatial-dimension reduction” method developed by Yang et al [27, 28, 29, 30, 31] has been adopted. The solution steps are as follows.

3.3.1 Finding the Wedge and Characteristic Directions

Directions of wedge lines are to be found in unit vector form as follows. In equations, vectors are demonstrated in bold and italic characters.

$$\mathbf{Flow} = \begin{bmatrix} 0 \\ 1 \\ 0 \end{bmatrix} \quad (1)$$

$$\mathbf{X} = \begin{bmatrix} \sin(\nu) \cos(\lambda_2) \\ \sin(\lambda_2) \\ \cos(\nu) \cos(\lambda_2) \end{bmatrix} \quad (2)$$

$$\mathbf{Z} = \begin{bmatrix} 0 \\ \sin(\lambda_1) \\ \cos(\lambda_1) \end{bmatrix} \quad (3)$$

$$\mathbf{X}_{wedge} = \begin{bmatrix} 0 \\ \cos(\theta_2) \\ \sin(\theta_2) \end{bmatrix} \quad (4)$$

$$\mathbf{Z}_{wedge} = \begin{bmatrix} \sin(\theta_1) \\ \cos(\theta_1) \\ 0 \end{bmatrix} \quad (5)$$

$$\mathbf{Dir}_{wedge} = (\mathbf{Z} \times \mathbf{Z}_{wedge}) \times (\mathbf{X} \times \mathbf{X}_{wedge}) \quad (6)$$

Flow is defined in +y direction as defined in Equation (1). \mathbf{X} and \mathbf{Z} are unit vectors that define the leading edges of wedges by Equations (2) and (3). In Equations Equations (2) and (3), ν , λ_2 and λ_1 define the dihedral and sweep angles, respectively. \mathbf{X}_{wedge} and \mathbf{Z}_{wedge} identify the directions of wedges in flow direction and determined by the wedge angles θ_2 and θ_1 , respectively. \mathbf{X}_{wedge} and \mathbf{Z}_{wedge} can be found by using Equations (4) and (5). Cross section line of wedges are defined as \mathbf{Dir}_{wedge} and can be found by Equation (6).

Characteristic direction is defined as the intersection line of two oblique shock waves emanated from wedges. To find the characteristic direction, shock angles (β) for wedge angles (θ) should be found. Oblique shock wave equations given in [33, p. 360] can be used for this purpose.

$$\cot(\theta_1) = \tan(\beta_1) \left(\frac{\gamma+1}{2} \frac{M_0^2}{(M_0 \sin(\beta_1))^2 - 1} - 1 \right) \quad (7)$$

$$\cot(\theta_2) = \tan(\beta_2) \left(\frac{\gamma+1}{2} \frac{M_0^2}{(M_0 \sin(\beta_2))^2 - 1} - 1 \right) \quad (8)$$

$$\mathbf{Z}_{char} = \begin{bmatrix} \sin(\beta_1) \\ \cos(\beta_1) \\ 0 \end{bmatrix} \quad (9)$$

$$\mathbf{X}_{char} = \begin{bmatrix} 0 \\ \cos(\beta_2) \\ \sin(\beta_2) \end{bmatrix} \quad (10)$$

$$\mathbf{Dir} = (\mathbf{Z} \times \mathbf{Z}_{char}) \times (\mathbf{X} \times \mathbf{X}_{char}) \quad (11)$$

Equations (7) and (8) can be used to find the shock angles β_1 and β_2 . It should be noted there are two roots for solutions of Equations (7) and (8). Small roots indicate the weak shock solutions which are more possible to occur. Thus, they should be used for the next steps.

\mathbf{Z}_{char} and \mathbf{X}_{char} identify the direction of shock angles in the flow direction and are functions of shock angles β_1 and β_2 , respectively. These directions can be calculated by using Equations (9) and (10). Finally, the characteristic direction \mathbf{Dir} is defined in Equation (11).

In corner flow problems, shock waves are formed due to change of flow directions and shock waves are the sources of change of flow parameters. Owing to being planar, their intersection can be defined with a line. This line was chosen as the characteristic direction. Along the characteristic direction, flow parameters do not change since interaction with any discontinuity is impossible. The characteristic

plane is perpendicular to the characteristic direction. On successive characteristic planes, change of flow parameters starts at point O (see Figure 3.1) and grows as the characteristic plane moves in the flow direction. In other words, for a steady corner flow problem, flow parameters change only in successive characteristic planes. Therefore, calculations and determination of reflection type are done on this plane.

$$\mathbf{M}_{c,d} = \frac{\mathbf{Dir} \cdot (M_0 \mathbf{Flow})}{|\mathbf{Dir}|} \mathbf{Dir} \quad (12)$$

$$\mathbf{M}_{c,p} = M_0 \mathbf{Flow} - \mathbf{M}_{c,d} \quad (13)$$

To find the velocity component on the characteristic direction in terms of Mach number ($\mathbf{M}_{c,d}$), upstream velocity vector should be projected in the characteristic direction as in Equation (12). The upstream velocity vector can be defined as the vectorial sum of two vectors which are defined on the characteristic direction and the characteristic plane. Thus, the velocity component on the characteristic plane $\mathbf{M}_{c,p}$ can be found by using Equation (13).

In the characteristic plane, shock wave directions and the angle between shock wave directions and velocity in the characteristic plane should be found (see Figure 3.2).

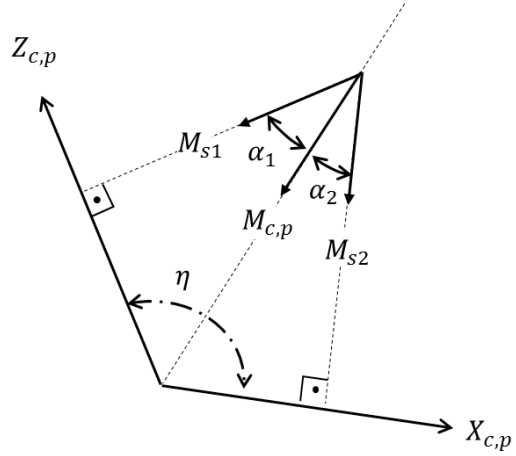


Figure 3.2. Demonstration of velocity components on characteristic plane

$$\mathbf{Z}_{c,p} = \mathbf{Z} - \mathbf{Z}_{c,d}$$

$$\text{where} \quad (14)$$

$$\mathbf{Z}_{c,d} = \frac{\mathbf{Dir} \cdot \mathbf{Z}}{|\mathbf{Dir}|} \mathbf{Dir}$$

$$\cos(\alpha_1) = \frac{\mathbf{Z}_{c,p} \cdot \mathbf{M}_{c,p}}{|\mathbf{Z}_{c,p}| |\mathbf{M}_{c,p}|} \quad (15)$$

$$M_{s1} = |\mathbf{M}_{c,p}| \sin(\alpha_1) \quad (16)$$

$$\mathbf{X}_{c,p} = \mathbf{X} - \mathbf{X}_{c,d}$$

$$\text{where} \quad (17)$$

$$\mathbf{X}_{c,d} = \frac{\mathbf{Dir} \cdot \mathbf{X}}{|\mathbf{Dir}|} \mathbf{Dir}$$

$$\cos(\alpha_2) = \frac{\mathbf{X}_{c,p} \cdot \mathbf{M}_{c,p}}{|\mathbf{X}_{c,p}| |\mathbf{M}_{c,p}|} \quad (18)$$

$$M_{s2} = |\mathbf{M}_{c,p}| \sin(\alpha_2) \quad (19)$$

$$\cos(\eta) = \frac{\mathbf{X}_{c,p} \cdot \mathbf{Z}_{c,p}}{|\mathbf{X}_{c,p}| |\mathbf{Z}_{c,p}|} \quad (20)$$

Shock wave directions $\mathbf{Z}_{c,p}$ and $\mathbf{X}_{c,p}$ on a characteristic plane can be found by the projection of directions of the wedge leading edges \mathbf{Z} and \mathbf{X} on the characteristic plane as given in Equations (14) and (17). It should be noted that shock waves are originated from the leading edges of wedges and follow the characteristic direction **Dir**. Angles in between $\mathbf{M}_{c,p}$ and shock wave directions $\mathbf{Z}_{c,p}$ and $\mathbf{X}_{c,p}$ are defined as α_1 and α_2 , respectively. They can be found by using cosine law as given in Equations (15) and (18). By using α_1 and α_2 , M_{s1} and M_{s2} which are normal components of $\mathbf{M}_{c,p}$ to $\mathbf{Z}_{c,p}$ and $\mathbf{X}_{c,p}$ can be found as given in Equations (16) and (19). The angle between shock waves in the characteristic plane (i.e., angle in between $\mathbf{Z}_{c,p}$ and $\mathbf{X}_{c,p}$) is identified as η and can be found by using cosine law as given in Equation (20).

It should be underlined that the velocity components M_{s1} and M_{s2} can also be considered as shock wave velocities for a pseudo-steady problem.

3.3.2 Determination of Interaction Type via Shock Polars

Shock polar diagrams indicate how the reflection (i.e., interaction) will occur based on wedge deflection angles and inflow Mach number. Therefore, shock polar analysis is to be performed on the characteristic plane. The problem can be shown as shown in Figure 3.3.

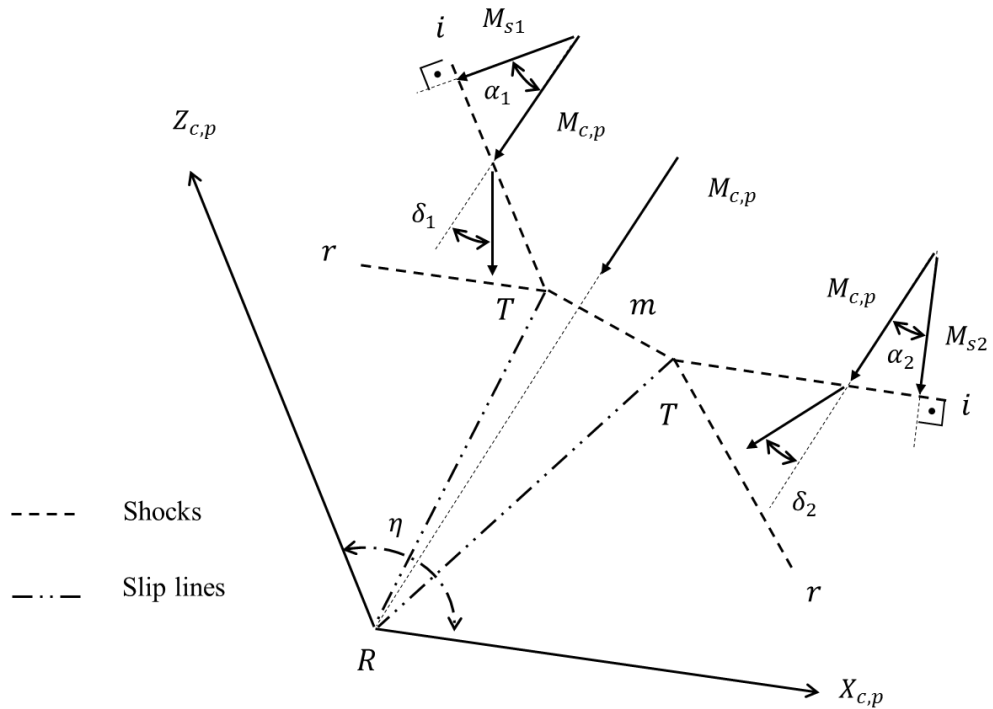


Figure 3.3. Demonstration of flow deflection angles on characteristic plane

When it is assumed that MR occurs; two triple points T's, incident shock wave i's and reflected shock wave r's should occur. Two triple points T's are connected with Mach stem m. Shock wave angles (α_1, α_2) of incident shock wave i's were already found by Equations (15) and (18).

$$\cot(\delta_1) = \tan(\alpha_1) \left(\frac{\gamma + 1}{2} \frac{|\mathbf{M}_{c,p}|^2}{\left(|\mathbf{M}_{c,p}| \sin(\alpha_1) \right)^2 - 1} - 1 \right) \quad (21)$$

$$\cot(\delta_2) = \tan(\alpha_2) \left(\frac{\gamma + 1}{2} \frac{|\mathbf{M}_{c,p}|^2}{\left(|\mathbf{M}_{c,p}| \sin(\alpha_2) \right)^2 - 1} - 1 \right) \quad (22)$$

To obtain shock polar diagrams, corresponding wedge angles (δ_1, δ_2) should be found first. They can be found by using Equations (21) and (22). These equations are oblique shock wave equations ([33, p. 360]).

$$\zeta_n = 1 + \frac{2\gamma}{\gamma + 1} ((|M_{c,p}| \sin(\beta_n))^2 - 1) \quad (23)$$

$$\tan(\theta_n) = 2 \cot(\theta_n) \frac{(|M_{c,p}| \sin(\beta_n))^2 - 1}{2 + |M_{c,p}|^2 (\gamma + \cos(2\beta_n))} \quad (24)$$

$$\mu_0 \leq \beta_n \leq 90^\circ \text{ where } \sin(\mu_0) = \frac{1}{|M_{c,p}|} \quad (25)$$

Shock polar curve for upstream Mach number (for the characteristic plane, $|M_{c,p}|$) can be found by solving the pressure ratio (ζ) equation (given in Equation (23)) after an oblique shock ([33, p. 359]) for every specified shock angle. Wedge angles (θ) should also be found for every specified shock angle (β) ([33, p. 360]) via Equation (24), and the curve is prepared for pressure ratio values for wedge angles. Shock angle is limited with Mach angle (μ_0) ([34, p. 1010]) and normal angle (see Equation (25)).

$$(M_1 \sin(\alpha_1 - \delta_1))^2 = \frac{(\gamma - 1)(|M_{c,p}| \sin(\alpha_1))^2 + 2}{2\gamma((|M_{c,p}| \sin(\alpha_1))^2 - (\gamma - 1))} \quad (26)$$

$$(M_2 \sin(\alpha_2 - \delta_2))^2 = \frac{(\gamma - 1)(|M_{c,p}| \sin(\alpha_2))^2 + 2}{2\gamma((|M_{c,p}| \sin(\alpha_2))^2 - (\gamma - 1))} \quad (27)$$

Shock polar curves for flow after incident shock wave i's can be prepared by following the procedure described above. It should be emphasized that Mach number after incident shock wave i's (M_1, M_2) on the characteristic plane should be used instead of $|\mathbf{M}_{c,p}|$ when required. This value can be found by using Equations (26) and (27). These equations define the Mach number after oblique shock wave and taken from [33, p. 360].

$$\zeta_1 = 1 + \frac{2\gamma}{\gamma + 1} ((|\mathbf{M}_{c,p}| \sin(\beta_1))^2 - 1) \quad (28)$$

$$\zeta_2 = 1 + \frac{2\gamma}{\gamma + 1} ((|\mathbf{M}_{c,p}| \sin(\beta_2))^2 - 1) \quad (29)$$

The pressure ratios ζ_1 and ζ_2 for deflection (i.e., wedge) angle can be found as given in Equations (28) and (29). Together with the deflection angle, the pressure ratio ([33, p. 359]) will be used in determining the initial point of shock polar curve for flow after incident shock wave i's.

After the flow properties after incident shock wave i's are obtained, three shock polar curves can be united in one graph. It should be noted that pressure ratio values for shock polar curves of flow region behind incident shock wave i's are to be multiplied with initial pressure ratio values found in Equations (28) and (29).

Determination of interaction type is done by inspection of two shock polar curves obtained for flow region behind incident shock wave i's. If the reflected shock polars intersect with each other, RR will occur. Otherwise, MR will form.

Sample graphs that demonstrate the shock polar curves and numerical results for selected flow parameters are prepared and given in Figure 3.4 and Figure 3.5 for MR and in Figure 3.6 and Figure 3.7 for RR respectively.

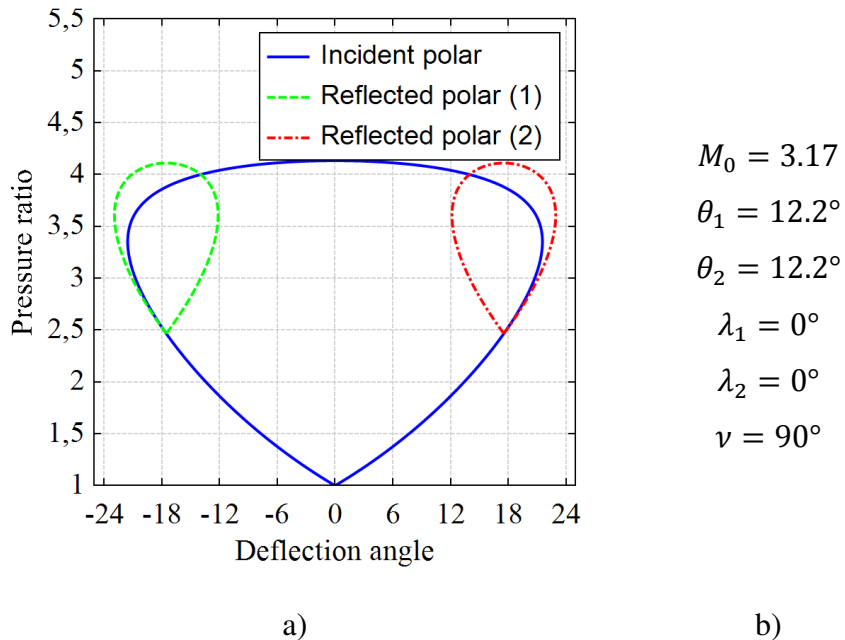


Figure 3.4. Shock polar curves (a) for flow parameters (b)

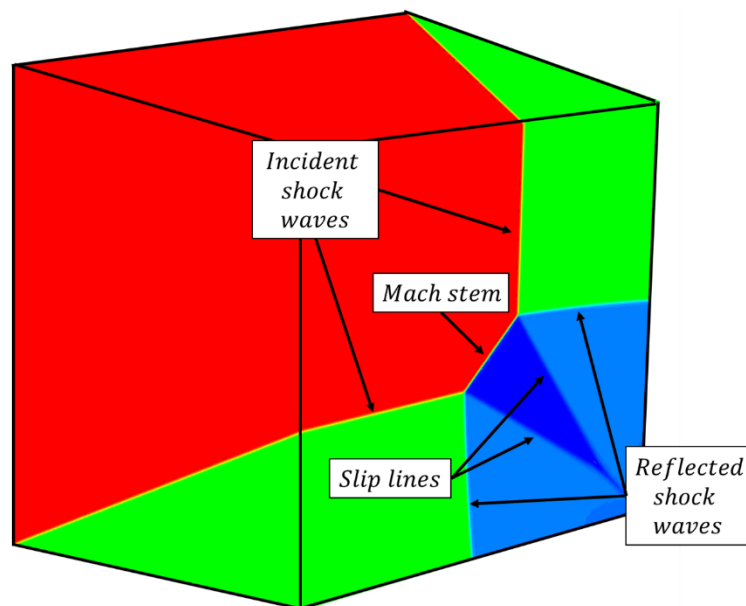


Figure 3.5. Numerical results based on flow parameters in Figure 3.4 b)

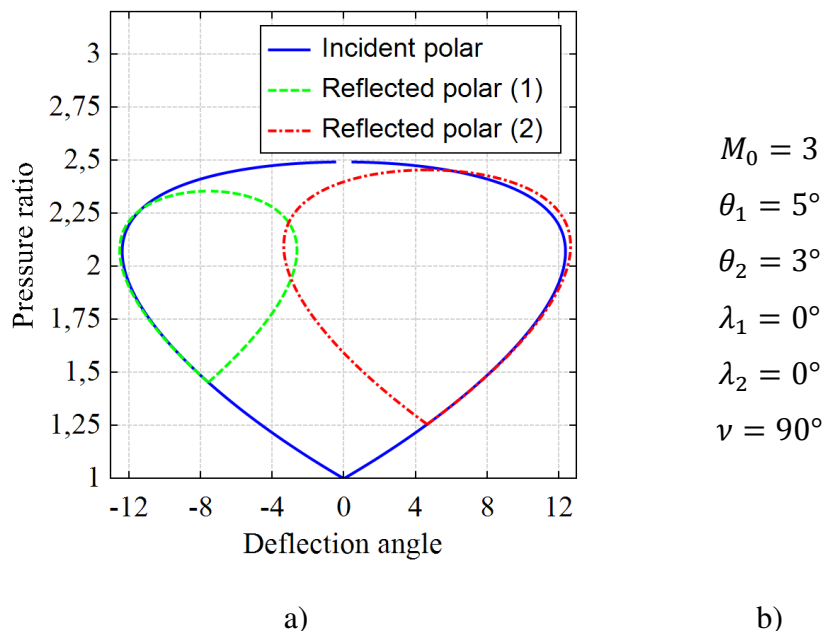


Figure 3.6. Shock polar curves (a) for flow parameters (b)

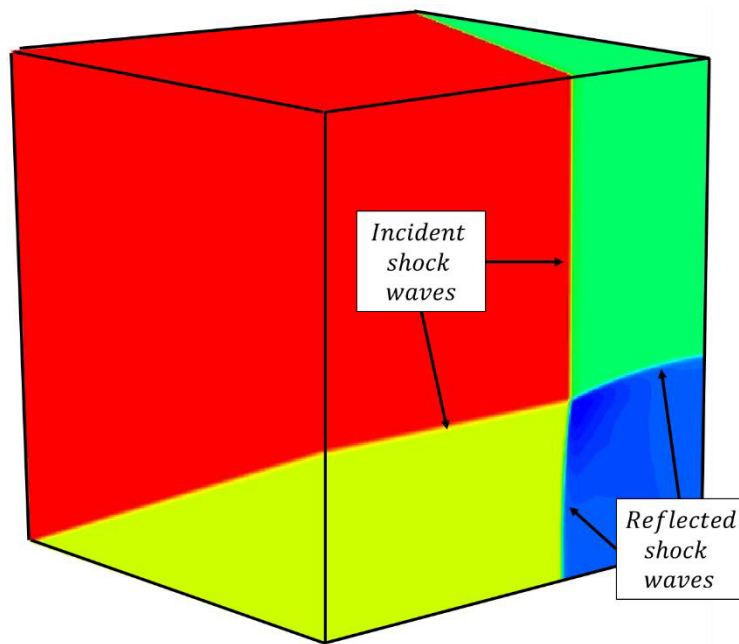


Figure 3.7. Numerical results based on flow parameters in Figure 3.6 b)

It should be noted that numerical results are obtained by following the procedure explained in Section 3.4. Figure 3.5 and Figure 3.7 indicate the Mach number contours on outer boundaries. Shock wave structures are indicated on the outlet plane. As expected, slip lines and Mach stem are not observed in the RR case.

3.3.3 Calculation of Mach Number of Stem and Related Angles

Interaction type is determined by the investigation of shock polar curves. If it is determined that MR will form, Mach number of stem and angles define its shape should be found.

As a general rule, the solution strategy should be based on simplifying the problem and assimilating it to another one whose solution is known as much as possible. The viscosity is already assumed to be insignificant and its effects are neglected. Under this assumption, two different types of boundary conditions become identical. These conditions are “wall” and “symmetry” as used in CFD terminology. In fluid mechanics, a wall-type boundary condition defines no flux across the boundary, whereas a symmetry-type one dictates that the derivative of flow properties on the boundary should be zero. Hence, by following the above-mentioned explanations and assumptions, it can be stated that in the absence of viscosity, the interaction of shock waves can be analytically transformed into a reflection problem. In other words, the problem of two interacting shock waves can be treated by using the solution of a shock wave reflected by a solid wall.

Flow parameters on the characteristic plane were found. However, it is impossible to find the position of Mach stem and slip lines since no relation can be defined between $M_{c,p}$ and the Mach stem (see Figure 3.3). This is the major difficulty to be overcome. Luckily, there are principles for the transformation of shock wave problems and solutions available for transformed problems.

Galilean transformation is defined to convert the problem with a moving shock wave to one possessing a stationary shock wave by selecting the coordinate frame which

travels with the shock wave. Although it is not common, the transformation can also be used for the opposite. Therefore, a problem of two intersecting steady shock waves can be transformed into a problem with two intersecting and moving shock waves. It should be kept in mind that in Galilean transformation, static properties of flow are preserved, whereas total (and dynamic) properties are changed [35, p. 7]. Hence, to find the correct dynamic properties, Galilean transformation should be done twice and the problem should be defined in its initial coordinate frame. Nevertheless, it is not required for static properties. A moving shock wave problem can be transformed into a steady shock wave one as shown in Figure 3.8.

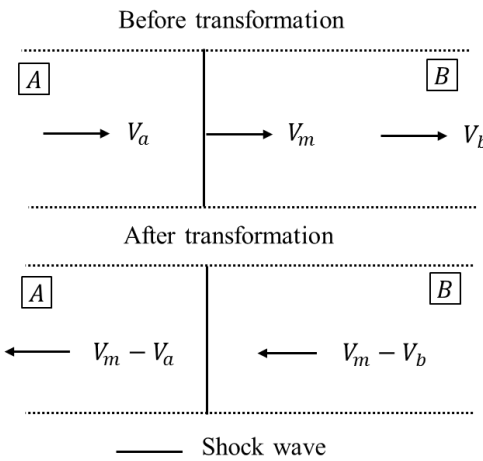


Figure 3.8. Demonstration of the Galilean transformation

It is shown that the case can be transformed into a problem with two moving and interacting shock waves via the Galilean method. It is also emphasized that the reflection of a shock wave from a surface and the interaction of two shock waves are also identical for inviscid flow. Then, the next solution step including the moving shock wave solutions based on shock dynamics principles can be introduced.

When a shock wave travels in a closed conduit with varying cross-sectional areas, its strength will change with changing area. Chester (1954), Chisnell (1957), and

Whitham (1958) developed the same relation by using different methods. This relation is known as the C.C.W. (C. for Chester, C. for Chisnell, and W. for Whitham) relation and defines the relationship between the shock wave Mach number and cross-sectional area of the conduit for uniform quiescent gas ahead of the shock wave [36, p. 486].

$$\frac{2MdM}{(M^2 - 1)K(M)} + \frac{dA}{A} = 0$$

where

$$K(M) = 2(2\mu + 1 + M^{-2})^{-1} \left(1 + \frac{2}{\gamma + 1} \frac{1 - \mu^2}{\mu} \right)^{-1} \quad (30)$$

$$\mu = \frac{(\gamma - 1)M^2 + 2}{2\gamma M^2 - (\gamma - 1)}$$

C.C.W. equation is given in Equation (30). $K(M)$ is a slowly varying function and its value is limited in between 0.5 and 0.3941 [32, p. 27] for diatomic gases (i.e., $\gamma = 1.4$). A defines the cross-sectional area of flow.

If a planar shock wave is diffracted around a wedge, a linear boundary forms in between undisturbed and disturbed shock waves. This linear boundary is called “shock-shock” and properties of flow can be found by following the above-mentioned C.C.W. relations and by using shock-ray solutions [32, p. 65]. The definition of this problem can be seen in Figure 3.9.

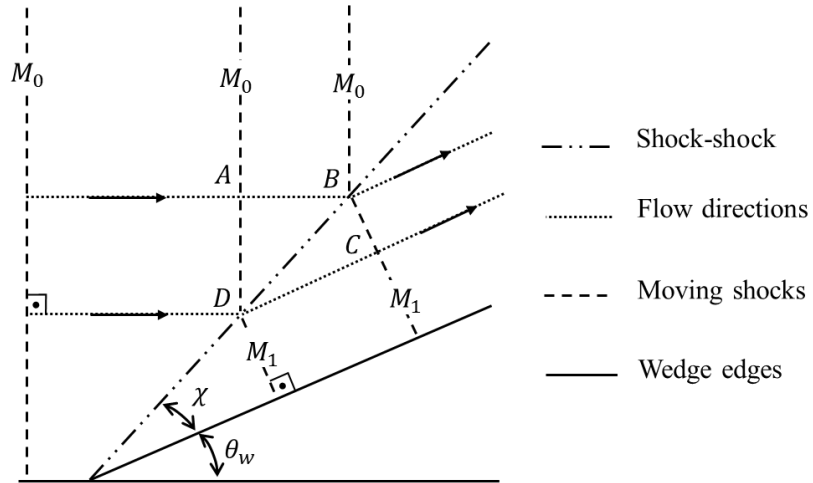


Figure 3.9. Demonstration of diffraction of a shock by a wedge

$$\tan(\chi) = \frac{f(M_1)}{f(M_0)} \left(\frac{1 - \left(\frac{M_0}{M_1} \right)^2}{1 - \left(\frac{f(M_1)}{f(M_0)} \right)^2} \right)^{\frac{1}{2}} \quad (31)$$

$$\tan(\theta_w) = \frac{M_1}{M_0} \frac{\left(1 - \left(\frac{M_0}{M_1} \right)^2 \right)^{\frac{1}{2}} \left(1 - \left(\frac{f(M_1)}{f(M_0)} \right)^2 \right)^{\frac{1}{2}}}{1 + \frac{f(M_1)}{f(M_0)} \frac{M_1}{M_0}} \quad (32)$$

$$f(M) = \exp \left(- \int \frac{2MdM}{(M^2 - 1)K(M)} \right) \quad (33)$$

The angle χ defines the trajectory of shock-shock and can be found by using Equation (31) if Mach numbers of undisturbed and diffracted flow are known. Similarly, wedge angle θ_w can be calculated by using Mach numbers of flow before and after the shock-shock region (see Equation (32)). Finally, Equation (33) identifies the solution of Equation (30) for A . It should be noted that Equations (31)

and (32) depend on solution Equation (33) whereas Equation (33) only depends on Mach number if γ is assumed to be constant. Equations (31), (32) and (33) are defined by following [32, p. 67].

Finally, if the Galilean transformation is done to the problem defined in Figure 3.3 and if the definitions for the angles and shock interface boundaries are used for the definition of the transformed problem, it can be defined as given in Figure 3.10. It should be underscored that the shock-shocks correspond to the slip lines and the flow field that is not affected by the shock waves has no velocity components on the characteristic plane. The flow field in the characteristic plane can be approximated as shock-shock evolution for a moving shock wave hits a wedge whose solution was already described.

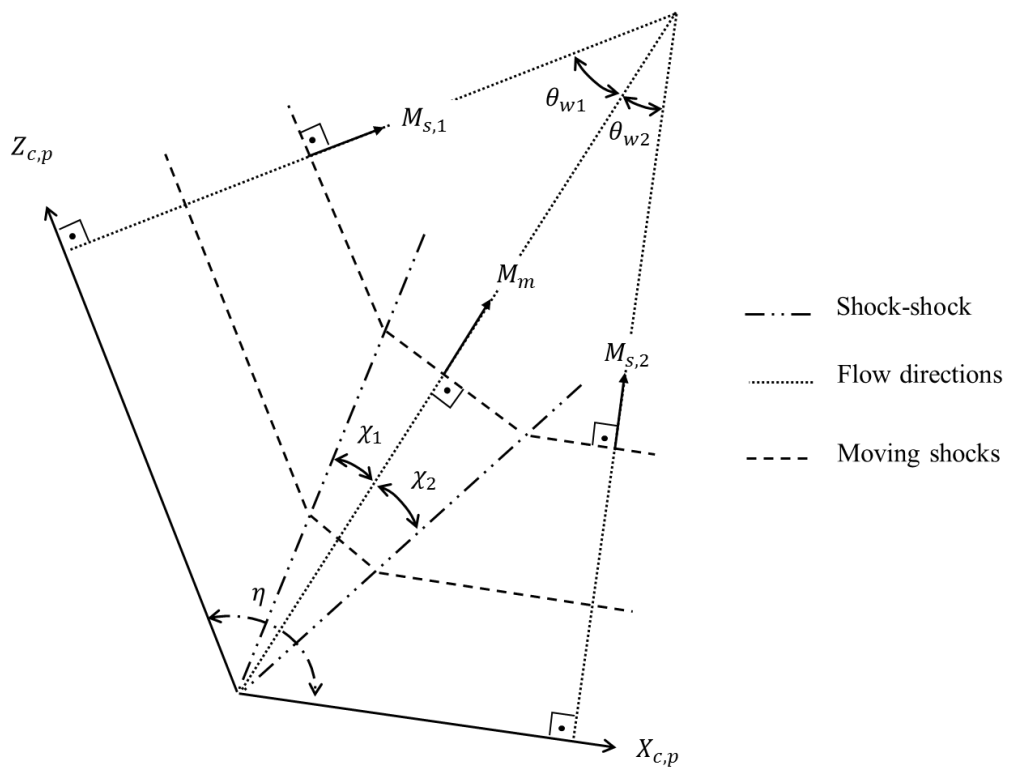


Figure 3.10. Demonstration of moving shock wave problem

$$\tan(\theta_{w1}) = \frac{M_m}{M_{s,1}} \frac{\left(1 - \left(\frac{M_{s,1}}{M_m}\right)^2\right)^{\frac{1}{2}} \left(1 - \left(\frac{f(M_m)}{f(M_{s,1})}\right)^2\right)^{\frac{1}{2}}}{1 + \frac{f(M_m)}{f(M_{s,1})} \frac{M_m}{M_{s,1}}} \quad (34)$$

$$\tan(\theta_{w2}) = \frac{M_m}{M_{s,2}} \frac{\left(1 - \left(\frac{M_{s,2}}{M_m}\right)^2\right)^{\frac{1}{2}} \left(1 - \left(\frac{f(M_m)}{f(M_{s,2})}\right)^2\right)^{\frac{1}{2}}}{1 + \frac{f(M_m)}{f(M_{s,2})} \frac{M_m}{M_{s,2}}} \quad (35)$$

$$\theta_{w2} + \theta_{w1} + \eta = 180^\circ \quad (36)$$

By following the equations given for the solution of diffraction of a moving shock from a wedge, Equations (34), (35), and (36) are defined. These equations are to be solved simultaneously. The wedge angles for moving shock waves in characteristic plane θ_{w1} and θ_{w2} are functions of Mach number of stem M_m , $M_{s,1}$ and $M_{s,2}$. Set of equations is completed with Equation (36).

$$\tan(\chi_1) = \frac{f(M_m)}{f(M_{s,1})} \left(\frac{1 - \left(\frac{M_{s,1}}{M_m}\right)^2}{1 - \left(\frac{f(M_m)}{f(M_{s,1})}\right)^2} \right)^{\frac{1}{2}} \quad (37)$$

$$\tan(\chi_2) = \frac{f(M_m)}{f(M_{s,2})} \left(\frac{1 - \left(\frac{M_{s,2}}{M_m}\right)^2}{1 - \left(\frac{f(M_m)}{f(M_{s,2})}\right)^2} \right)^{\frac{1}{2}} \quad (38)$$

It should be noted that shock-shock lines define the trajectory of triple point T's. Thus, they can be considered as slip lines. The angles between shock-shock (i.e., slip line) and Mach stem direction are defined as χ_1 and χ_2 can be found as defined in Equations (37) and (38). It should be noted that Equations (37) and (38) are formed by following the principles of diffraction of a moving shock wave from a wedge (see Equation (31)).

After Mach number of stem M_m is found, the second Galilean transformation (see Figure 3.8) should be done in the reversed way to find the flow properties. The transformed problem included two interacting moving shock waves on a quiescent medium. Thus, undisturbed velocity V_b in Figure 3.8 equals to zero. However, after the second transformation, the flow which experiences a normal shock is found to have the Mach number equal to the Mach number of stem. Therefore, the pressure ratio across Mach stem can be found as follows.

$$\zeta_m = \frac{2\gamma M_m^2 - (\gamma - 1)}{\gamma + 1} \quad (39)$$

Equation (39) defines the pressure ratio across Mach stem ζ_m and uses the normal shock waves relations ([33, p. 349]). Pressure ratio ζ_m is selected as the quantity to be compared with other results, numerical or experimental.

Angles define the slip lines χ_1 and χ_2 are found by Equations (37) and (38) and their definitions can be seen in Figure 3.10. Thus, the solution on the characteristic plane could be completed if the directions of slip lines were identified.

$$\mathbf{Dir}_{S1} = \mathbf{C}_1 + \mathbf{C}_2 \cos\left(\frac{\pi}{2} - (\pi - \eta - \theta_{w1}) + \chi_1\right) \quad (40)$$

$$+ \mathbf{C}_3 \sin\left(\frac{\pi}{2} - (\pi - \eta - \theta_{w1}) + \chi_1\right)$$

$$\mathbf{Dir}_{S2} = \mathbf{C}_1 + \mathbf{C}_2 \cos\left(\frac{\pi}{2} - (\pi - \eta - \theta_{w1}) - \chi_2\right) \quad (41)$$

$$+ \mathbf{C}_3 \sin\left(\frac{\pi}{2} - (\pi - \eta - \theta_{w1}) - \chi_2\right)$$

where;

$$\mathbf{C}_1 = ((-\mathbf{Dir}) \cdot (-\mathbf{Dir}^T)) \mathbf{X}_{c,p}$$

$$\mathbf{C}_2 = \mathbf{X}_{c,p} - \mathbf{C}_1$$

$$\mathbf{C}_3 = -\mathbf{Dir} \times \mathbf{X}_{c,p}$$

Equations (40) and (41) can be used to find the directions of the slip lines. \mathbf{Dir}_{S1} and \mathbf{Dir}_{S2} define the slip lines on the characteristic plane and are found by rotation of direction vector of $\mathbf{X}_{c,p}$ around the characteristic direction \mathbf{Dir} by wedge (θ_{w1}) and slip line angles χ_1 and χ_2 . The rotation equations are known as Rodriques' formula [37].

3.3.4 Calculations for Plane of Investigation

The final step of the analytical solutions is to present the findings properly. Although the characteristic plane is useful for solving the problem, it would be inappropriate to demonstrate the results on it for two main reasons. Firstly, because of the way it is defined, the characteristic plane changes for any change either in the flow or in the geometrical parameters. It is even affected by the change of flow medium, from air to Helium, for instance. Therefore, it would be impossible to evaluate the impact of a variable that changes if the results are demonstrated on the characteristic plane. Secondly, it is aimed to compare the analytical results with experimental data,

therefore both results could be displayed similarly. The experimental data explained and discussed in Section 2.4.1 was expressed in conical coordinates as the upstream flow direction is selected as the basis. This selection implies that comparison can be made at any plane whose normal is parallel to the direction of undisturbed flow. Therefore, the investigation plane is selected as normal to the upstream flow.

The schematic demonstration of results on the plane of investigation is given as in Figure 3.11. The lines on the scheme can be categorized into four groups which show the wedges, the incident shock waves, the slip lines, and the Mach stem.

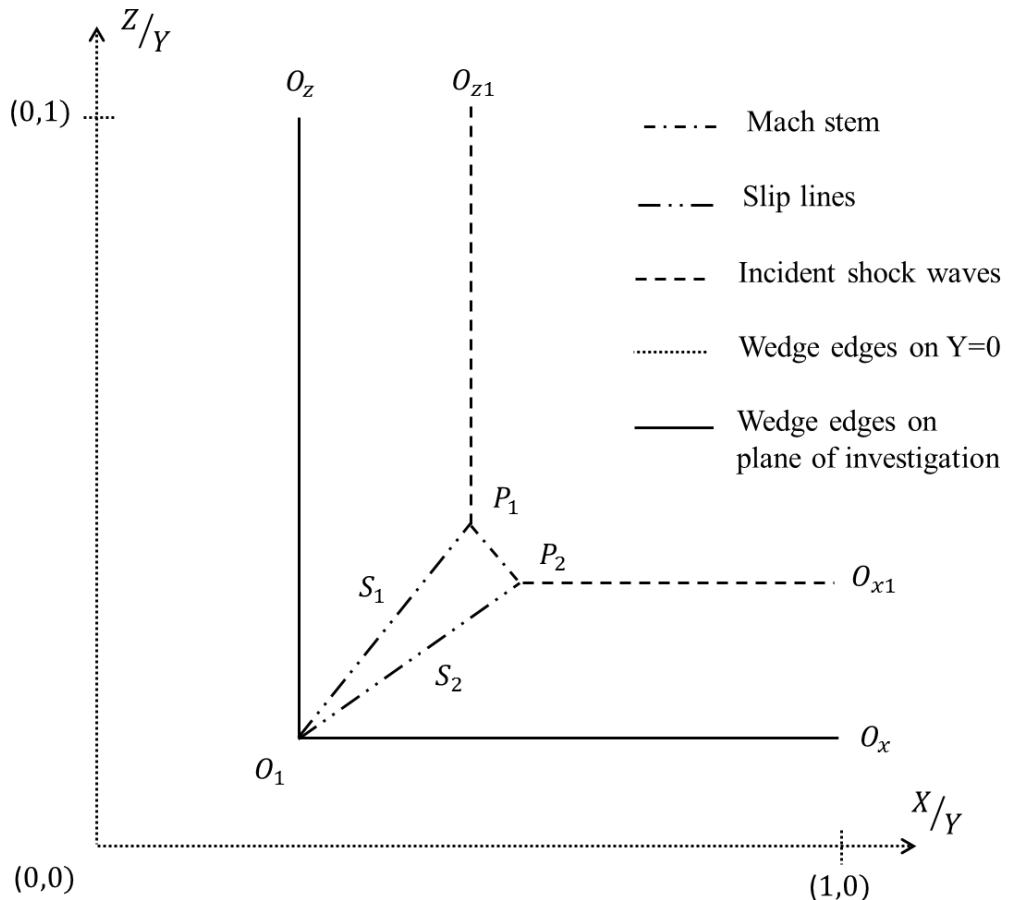


Figure 3.11. Demonstration of results on the plane of investigation

$$\mathbf{S}_2 = \begin{bmatrix} A \\ 0 \\ B \end{bmatrix}; m_{S_2} = \frac{A}{B}$$

where; (42)

$$(\mathbf{Dir}_1 A + \mathbf{Dir}_3 B) \cdot \mathbf{Dir}_1 + \mathbf{Dir}_{S21} - A = 0$$

$$(\mathbf{Dir}_1 A + \mathbf{Dir}_3 B) \cdot \mathbf{Dir}_3 + \mathbf{Dir}_{S23} - B = 0$$

$$\mathbf{S}_1 = \begin{bmatrix} C \\ 0 \\ D \end{bmatrix}; m_{S_1} = \frac{D}{C}$$

where; (43)

$$(\mathbf{Dir}_1 C + \mathbf{Dir}_3 D) \cdot \mathbf{Dir}_1 + \mathbf{Dir}_{S11} - C = 0$$

$$(\mathbf{Dir}_1 C + \mathbf{Dir}_3 D) \cdot \mathbf{Dir}_3 + \mathbf{Dir}_{S13} - D = 0$$

Directions of slip lines on the plane on investigation ($\mathbf{S}_1, \mathbf{S}_2$) and their slopes (m_{S_1}, m_{S_2}) can be found by solving Equations (42) and (43). Those equations define the projection of the direction of slip lines on the characteristic plane to the plane of investigation. Projection direction is the characteristic direction \mathbf{Dir} .

Positions of shock waves and wedges at the plane of investigation can be found by using relations for $X_{char}, Z_{char}, \mathbf{Dir}$ and \mathbf{Dir}_{wedge} which were already found. Points P_1 and P_2 are intersection points of slip lines and shock waves. P_1 and P_2 are found by the intersection of shock wave and slip line equations. Mach stem is constructed by connecting the points P_1 and P_2 by a line. Thus, Mach stem is treated as linear.

The presentation of results on the plane on investigation completes the analytical solution part.

Screenshots of a sample analytical solution are given in the Appendix A section.

3.4 Numerical Solutions

The numerical studies are performed to show the conformity of the analytical results. The main intention of comparison with the numerical results is to show the consistency of analytical results under the same or similar assumptions. Hence, the numerical solutions are designated accordingly.

A conventional numerical or computational study contains three steps. The first one defines the preparation of geometry. The geometrical model is also called the flow domain. The flow domain determines the outer limits of the problem. The second step is mesh preparation. The mesh or the grid divides the flow domain into finite volumes. These volumes are called cells and they are the basis of the computational domain. After the mesh is prepared, it is introduced to the solver. The solver discretizes the governing equations and does the computations by doing iterations until the defined convergence criteria are achieved. The flow properties are preserved in the cells either in the center or in its nodes. By using this information, flow properties can be visualized as contours or streamlines.

In this study, numerical solutions are performed done by using ANSYS Workbench 2020 R2 tools. The steps followed for the preparation and execution of the numerical study are given as follows.

3.4.1 Geometry Preparation

Geometry preparation for the numerical solution is done using ANSYS Design Modeler 2020 R2. It is determined to have a flow field whose dimensions at inlet 5×5 mm and depth in flow direction is 5 mm. A parametric model is prepared following the geometrical definitions in Section 3.2. A sample geometry can be seen in Figure 3.12 a).

3.4.2 Meshing

Meshing is done by using ANSYS Meshing 2020 R2. Structured mesh based on hexahedron-shaped elements is formed and provided to the solver as the base solution domain. Element size is approximately 1 mm and around 200 elements and nodes are present in the initial computational domain. Initial element size, together with the geometrical limits, is determined after several trials. After the adaptation steps (see Section 3.4.3.4), it is aimed to have elements with a minimum size in between 0,01-0,02 mm and a total number less than 3×10^6 . The minimum size of elements indicates the resolution of results, whereas the total number determines the solution time. Therefore, their accordance is critical for an accurate and economical numerical analysis especially if it includes shock waves.

A sample mesh can be seen in Figure 3.12 b).

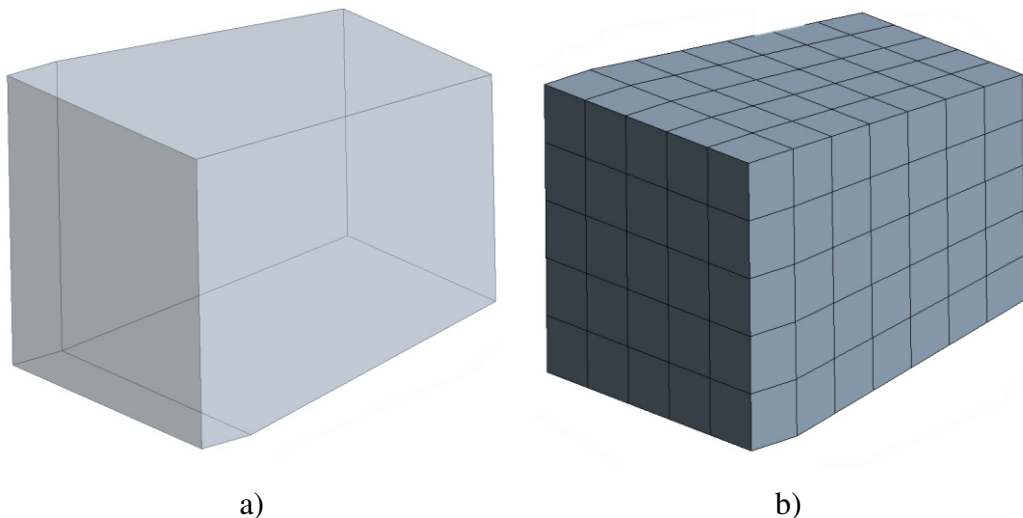


Figure 3.12. Demonstration of geometry a) and mesh b)

3.4.3 Solver

Numerical solutions are performed by using ANSYS Fluent 2020 R2. A proper computational study necessitates the selection of the correct material model, suitable boundary conditions, and appropriate solver settings. These steps are defined in the following sections, including the mesh adaptation and post-processing processes.

3.4.3.1 Material Model

The flow is assumed to obey the ideal and perfect gas assumption. Molecular weight and specific heat capacity values used are given in Table 3.1.

Table 3.1 Material properties

Property	Abbreviation	Value	Unit
The ratio of specific heats	γ	1.4	-
Molecular weight	M_a	28.966	g/mol
Specific heat	c_p	1006.43	$J/kg * K$

3.4.3.2 Boundary Conditions

Locations of boundary conditions are given in Figure 3.13. At the inlet, the pressure far-field boundary condition is used to specify the Mach number. In addition, the static pressure and temperature are defined as 80 kPa and 300 K , respectively. At outlet region, pressure outlet is defined. It should be noted that the selected solver checks the flow Mach number for the outlet region and overrides the pressure value specified if the flow is supersonic. Thus, it does not reflect any information to the

calculation domain for the supersonic outlet case. Wedges are selected to be wall boundary conditions while remaining boundaries are chosen as symmetry.

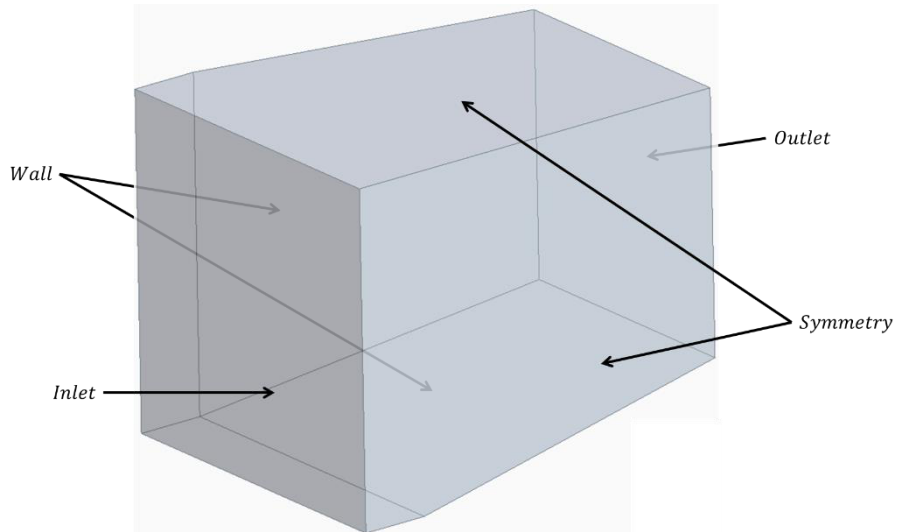


Figure 3.13. Demonstration of boundary condition on geometry

3.4.3.3 Solver Settings

As stated and justified in Section 3.1, flow is assumed to be inviscid.

A density-based implicit solver with flux type of AUSM is chosen for the numerical solution. Second-order upwind for spatial discretization of flow and least-squares cell-based gradient evaluation methods are chosen.

A density-based solver is a coupled solver and solves conservation equations (continuity, momentum, and energy equations for such problems) simultaneously. In density-based solution methods, governing equations that are non-linear are linearized for every cell to get a system of equations for the dependent variables. A linearized system is solved to find the updated solution for the flow field. Being implicit refers to the selection of linearization of governing equations. In the implicit

method, the unknown value in each cell is calculated using a set of equations that contains both existing and unknown values from neighboring cells. Thus, each unknown appears in more than one equation and all the equations must be solved simultaneously for unknown values. [38, pp. 644-645]

$$\frac{\partial}{\partial t} \int W d\forall + \oint (F - G) dA = \int H d\forall \quad (44)$$

$$W = \begin{bmatrix} \rho \\ \rho u \\ \rho v \\ \rho w \\ \rho E \end{bmatrix}, F = \begin{bmatrix} \rho V \\ \rho Vu + p\hat{i} \\ \rho Vv + p\hat{j} \\ \rho Vw + p\hat{k} \\ \rho VE + pV \end{bmatrix}, G = \begin{bmatrix} 0 \\ \tau_{xi} \\ \tau_{yi} \\ \tau_{zi} \\ \tau_{ij}V_j + q \end{bmatrix} \quad (45)$$

$$E = H - \frac{p}{\rho} \quad (46)$$

$$H = h + \frac{|V|^2}{2} \quad (47)$$

Governing equations in vector forms for density-based solvers are given in Equations (44), (45), (46), and (47). Equation (44) defines the system of governing equations for a single-component fluid for an arbitrary control volume \forall with a surface area dA . Equations (45), (46) and (47) shows the vectors which are included in system of governing equation. In those equations, ρ , V , E and p are the density, velocity, total energy for unit mass and pressure of the fluid, respectively. τ and q are viscous stress tensor and heat flux. It should be noted that total energy E and total enthalpy H are related with Equation (46) [38, p. 677].

AUSM (Advection Upstream Splitting Method) is proposed as an alternative way to compute flux vectors. This scheme is used since it is successful in “providing exact

resolution of contact and shock discontinuities [38, p. 681]” and “free of oscillations at stationary shock [38, p. 682]”.

Convergence is followed with control of residual terms of flow equations and mesh adaptation is done after residual terms for every term dropped around 1×10^{-3} and no more change in residual terms observed. For every solution between adaptations, approximately 1×10^3 iterations are done. The total solution takes 1×10^4 iterations roughly.

3.4.3.4 Mesh Adaptation

Mesh adaptation can be defined as coarsening or refining the mesh by using the solution data obtained. Because shock waves are treated as being infinitesimally small [39], a mesh adaptation technique is to be used to lessen the demand on computing sources (including time) while having a good resolution of discontinuities.

Gradient-based mesh adaptation is chosen. Since Mach number changes across every discontinuity in the flow field including slip lines, gradient calculations are preferred to be on this quantity to capture the flow field with a higher resolution [40]. Adaptation criterion for refinement and coarsening, cells with Mach number gradient higher than 0.01 and less than 0.005 are selected, respectively.

Adaptation is based on Mach number gradient with a maximum refining level of 6. Thus, at the shock zone, the element size is around 0.016 mm which is 64 times smaller than the initial mesh size. Final element and node numbers are about 2.5×10^6 .

Adaptation is done manually after solutions are converged.

The final mesh of a selected case is given in Figure 3.14 and Figure 3.15.

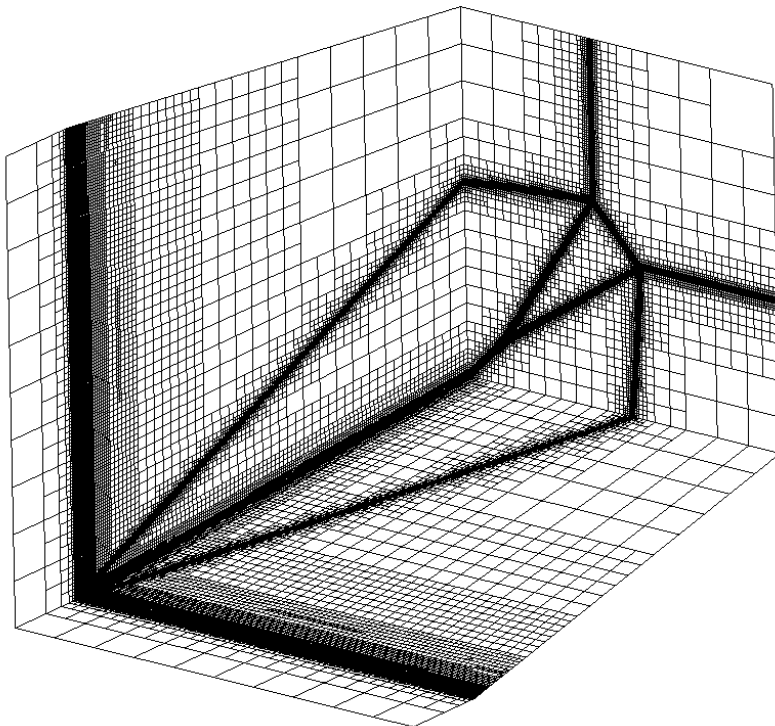


Figure 3.14. Demonstration of final mesh / inlet and symmetry regions hidden

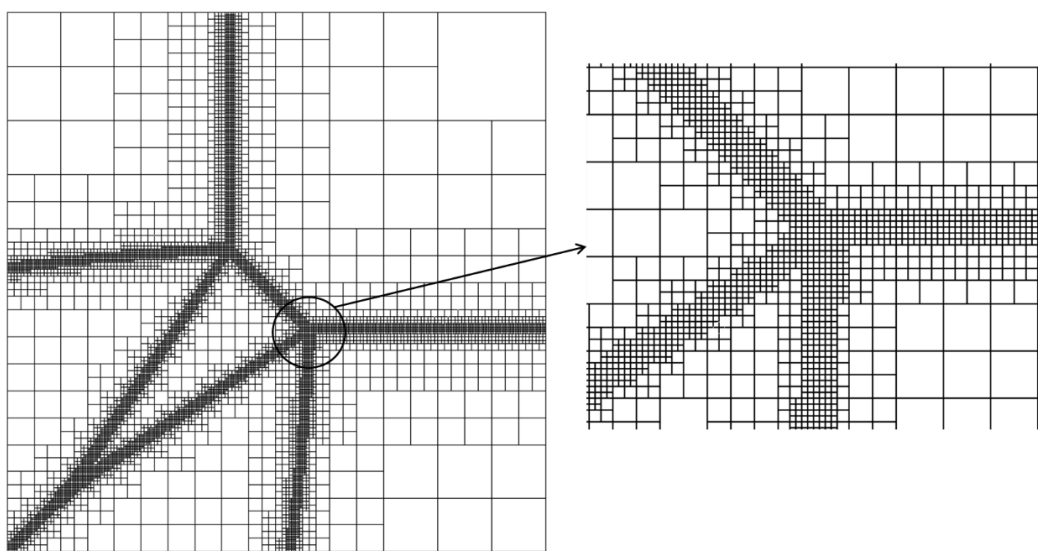


Figure 3.15. Demonstration of final mesh for outlet region

3.4.3.5 Demonstration of Results of Numerical Solutions

Results of numerical solutions are presented as pressure and Mach number (i.e., velocity) contours in iso-value demonstrations. Field contours for pressure and Mach number are prepared on the outlet (See Figure 3.13) region which is an example of the plane of investigation defined in Section 3.3.4. A total number of 100 iso-lines in between local maximum and minimum values of flow property are used to show the regions where flow properties change. Since flow fields are to be compared with analytical and experimental results to show their conformity, iso-lines are created in grayscale without legends. The pressure ratio across the Mach stem is calculated by using pressure values on the line created on the outlet. This manually formed line is selected to be originated at the wedge intersection point, crosses the Mach stem on its approximate mid-point, and extends towards the region where flow is not affected by shock waves. A sample line for pressure ratio calculation on adapted outlet mesh can be seen in Figure 3.16.

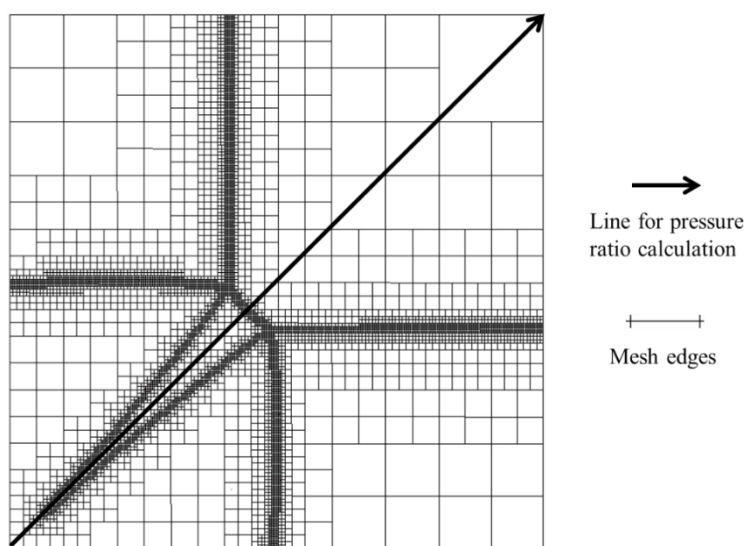


Figure 3.16. Demonstration of calculation line for pressure ratio

3.5 Computer Source and Solution Durations

All solutions are done with a computer. Computer hardware is as given in Table 3.2.

Table 3.2 Computer source

Type / model	:	Laptop / Lenovo ideapad Z580
RAM	:	8 GB DDR3
Processor	:	4 core (2 virtual), i5-3210M with 2.50 GHz max. speed
Disk	:	Solid-state drive
Operating system	:	Windows 8.1

Average computing times are 90 seconds for analytical, 24 hours for numerical solutions. It should be emphasized that numerical solutions are done by using MPI algorithms which shorten the solution times by dividing the solution domain into parts. By using MPI algorithms with two cores, numerical solutions are estimated to last approximately two times shorter than serial (i.e., one core) solutions.

CHAPTER 4

RESULTS AND DISCUSSIONS

This chapter is devoted to the comparison of analytical solutions with experimental and numerical results and discussion of deviations in results.

Thirteen analytical and numerical studies are performed. Flow and geometrical parameters of studies are summarized in Table 4.1.

Table 4.1 Flow and geometrical parameters

Case #	Mach number	θ_1 ($^{\circ}$)	θ_2 ($^{\circ}$)	λ_1 ($^{\circ}$)	λ_2 ($^{\circ}$)	ν ($^{\circ}$)
Ref. [17]	3	9.5	9.5	0	0	90
Ref. [14]	3.17	12.2	12.2	0	0	90
A	4	10	10	3	10	90
B	5	10	5	0	0	90
C	3.17	12.2	3.5	0	0	90
D	3	5	5	30	25	90
E	3.5	10	15	10	5	80
F	4.5	15	15	15	15	70
G	2.5	5	7.5	10	0	90
H	3.25	4	15	5	10	90
I	2.25	8	6	0	0	90
J	2	7.5	7.5	0	0	90
K	1.5	3	5	5	5	90

To have an overall understanding of the validity of the proposed analytical method, flow and geometrical parameters are altered in separate cases. Effects of the

asymmetrical intersection of wedges, Mach number, and compression level of flow are investigated. Asymmetrical intersection not only implies the difference in wedge angles but only includes the change of sweep angles. Mach numbers of cases are kept between 1.5 and 5. The degree of compression that the flow experiences is set by changing the dihedral, sweep, and wedge angles and Mach numbers.

Results are presented under two main titles as flow field and pressure ratio across Mach stem comparisons. For pressure ratio comparisons, values obtained from analytical and numerical data are tabulated and percent difference based on numerical data is calculated. Shock polar diagrams, pressure ratio curves along the calculation line, and velocity and pressure contours from numerical results are given in Appendices B, C, and D sections, respectively.

4.1 Comparison of Flow Fields

Flow field comparisons are done by demonstrating the results on a plane of investigation (perpendicular to upstream velocity direction) by using velocity fields for numerical solutions, by using the test data for experimental studies, and by using the positions of Mach stem drawn on figures for analytical results. Flow field presentations are made by using conical variables on the base of flow direction (+y). Experimental, numerical, and analytical data are digitized manually over plots presented in references and velocity contours prepared for each case.

4.1.1 Comparison of Flow Field with Experimental Data

Experimental results presented in Figure 2.4 for [14] and Figure 2.5 for [17] are used for comparison purposes as Case Ref. [14] and Case Ref. [17].

In experiments, viscous effects are inevitably effective on flow structures as no special measures were taken to suppress the formation of the boundary layer in neither [14] nor [17] (see Section 2.4.1). Viscous effects were linked with boundary

layer displacements and investigated as a function of Re number in [17]. According to the outcomes of this study, flow field structures are expected to show little dependency on Re number when Re number is beyond the threshold of the turbulent flow for external flow. However, the opposite was shown to be true for smaller Re numbers in both [14] and [17]. In other words, flow fields at which viscous effects are more important (i.e., having smaller Re numbers), solutions with inviscid flow assumption would deviate from experimental results.

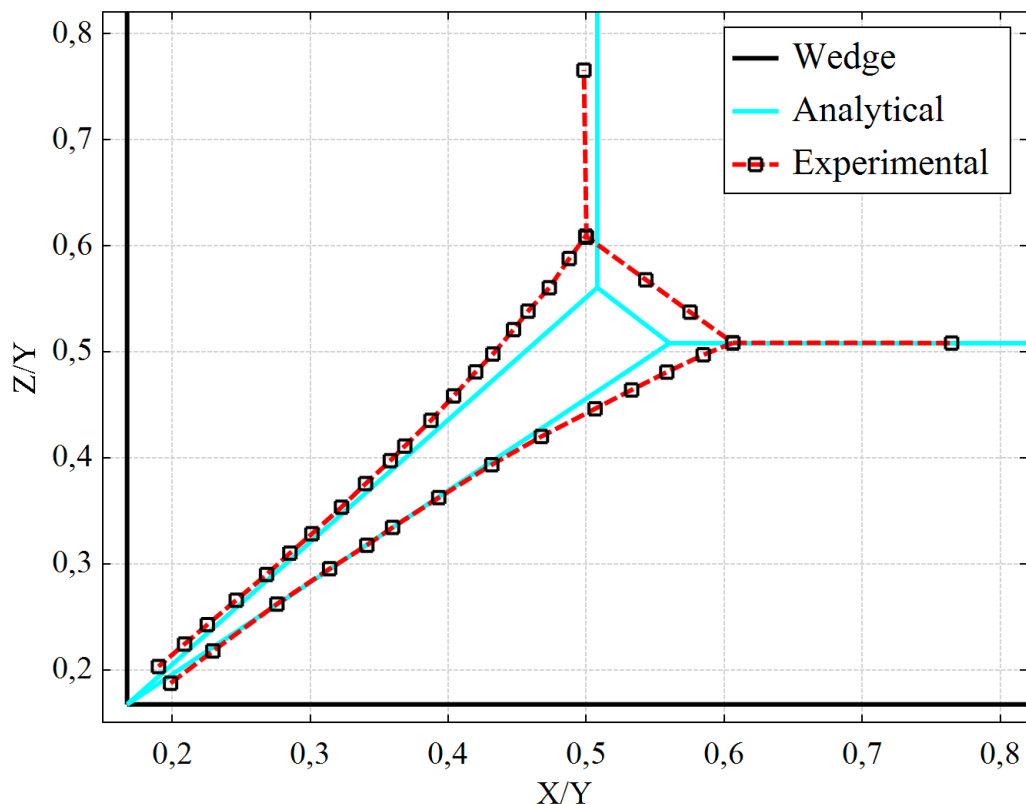


Figure 4.1. Comparison of analytical and experimental result for Case Ref. [17]

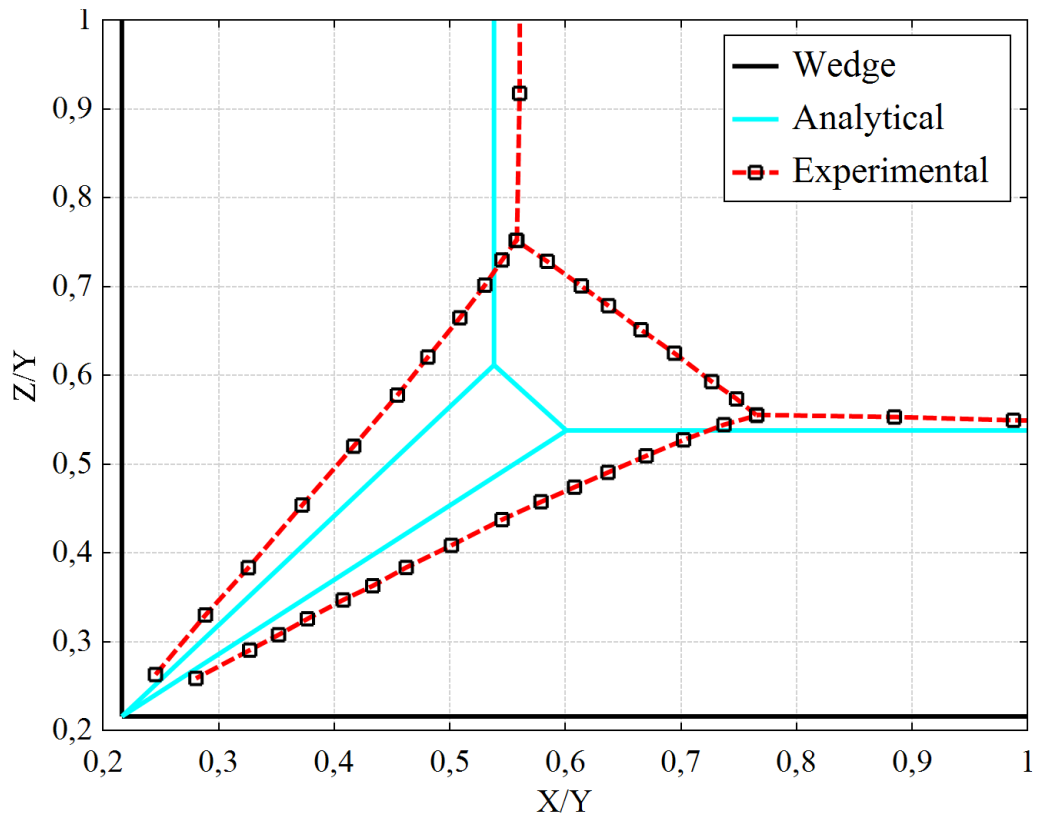


Figure 4.2. Comparison of analytical and experimental results for Case Ref. [14]

Indeed, a bigger difference is observed when the analytical results are compared with experimental data at which the flow field is laminar as in Case Ref. [14] as demonstrated in Figure 4.2. Analytical results are found to be closer to experimental data where the flow field is turbulent and less prevailed by viscosity as in Case Ref. [17] as shown in Figure 4.1.

It should be underlined that this outcome is expected for two additional reasons. Firstly the variation of shock structures of laminar and turbulent flows was already studied in [17] and stated that Mach stems were found at bigger distances to the corner in laminar flow as given in Figure 2.6. Secondly, the analytical solutions assume that the flow is inviscid. The flow approaches inviscid conditions as the Re number increases. The Re number is also a direct indicator of the type of flow regime

and turbulent flow is characterized by high Re numbers. Therefore, rather than a laminar flow, a turbulent flow can be studied better with inviscid methods.

4.1.2 Comparison of Flow Field with Numerical Results

The analytical results are compared with numerical results obtained for all cases defined in Table 4.1.

In Cases Ref. [17] and Ref. [14], the wedges are intersected symmetrically with zero sweep and orthogonal dihedral angles. Mach numbers are moderate in both cases.

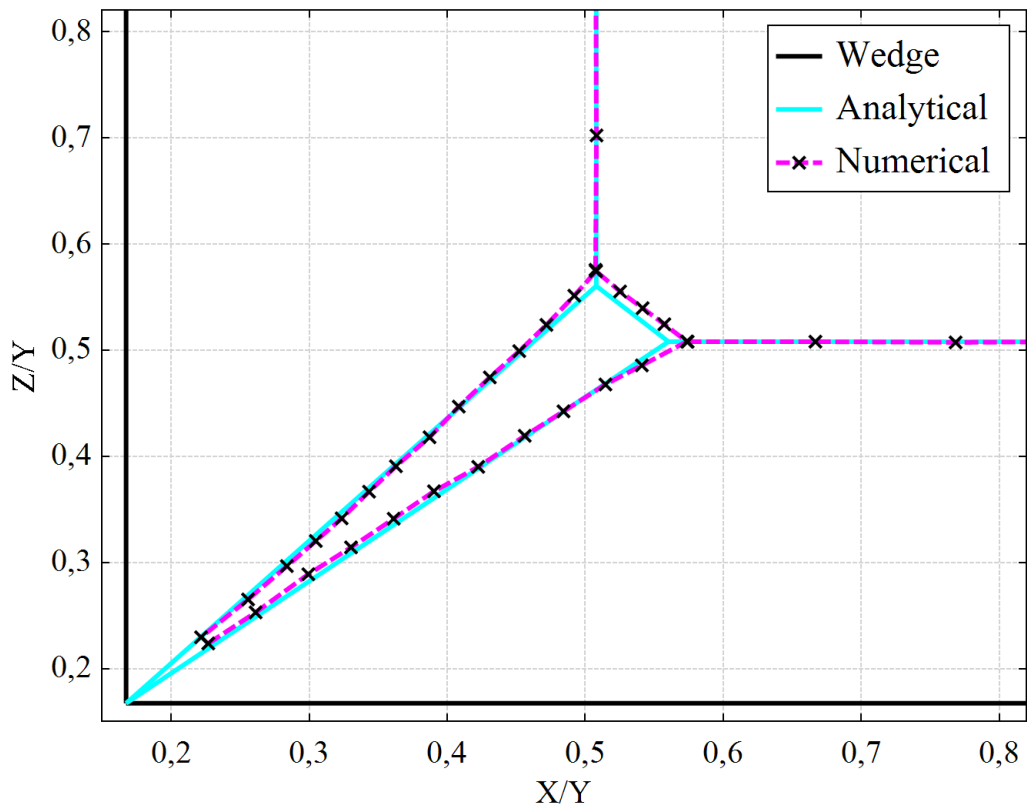


Figure 4.3. Comparison of analytical and numerical results for Case Ref. [17]

A very good agreement is observed in the comparison of analytical results with numerical ones for Case Ref. [17] although the position of Mach stem is found slightly different, distant to the corner in numerical results. The comparison for Case Ref [17] is given in Figure 4.3.

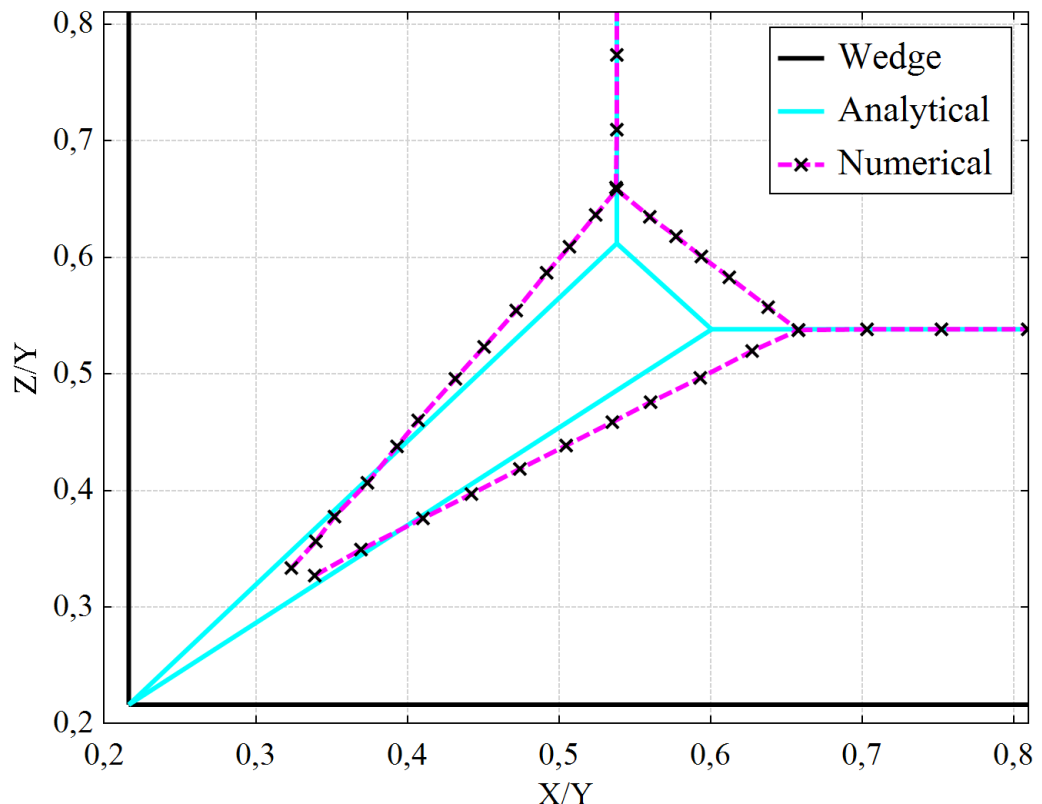


Figure 4.4. Comparison of analytical and numerical results for Case Ref. [14]

For Case Ref. [14], however, results show significant variations in both positions of Mach stem and angles of slip lines as given in Figure 4.4. The numerical results indicate that slip lines do not intersect at the corner. This is an unpredicted and distinctive feature of the flow field as no similar structure is observed in numerical

results of Case Ref. [17] and slip and wedges surfaces are assumed to intersect on the same line in analytical solutions.

When two symmetrical cases are compared in terms of flow and geometrical properties, higher wedge angles and Mach number are distinguished in Case Ref. [14]. This means that the flow experiences higher compression in Case Ref. [14]. Thus, it can be concluded that analytical methods give less accurate results when the compression becomes higher.

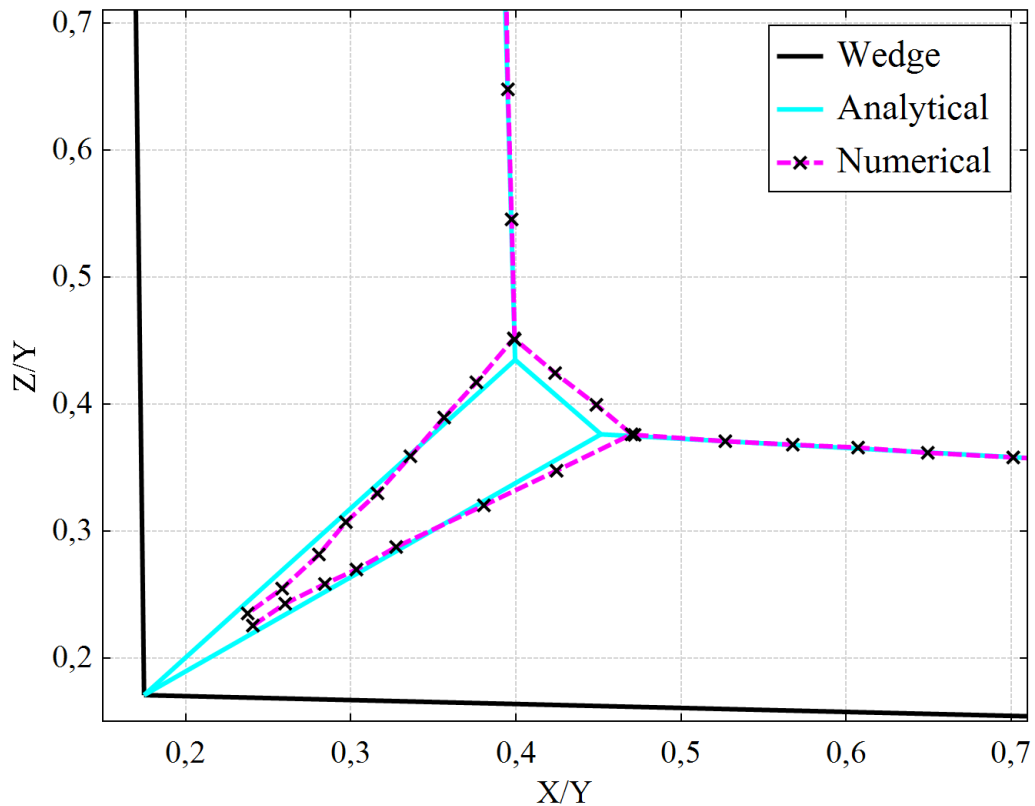


Figure 4.5. Comparison of analytical and numerical results for Case A

Case A has symmetrical wedge, orthogonal dihedral, small sweep angles, and relatively high Mach number. Comparison of results given in Figure 4.5 indicates

that good agreement is obtained. The distance of Mach stem to the corner is found extended in numerical solutions. Nevertheless, the results are more coherent when the conformity is checked with Case Ref. [14]. Thus, it can be concluded that the increase in wedge angles rather than sweep is more effective on compression.

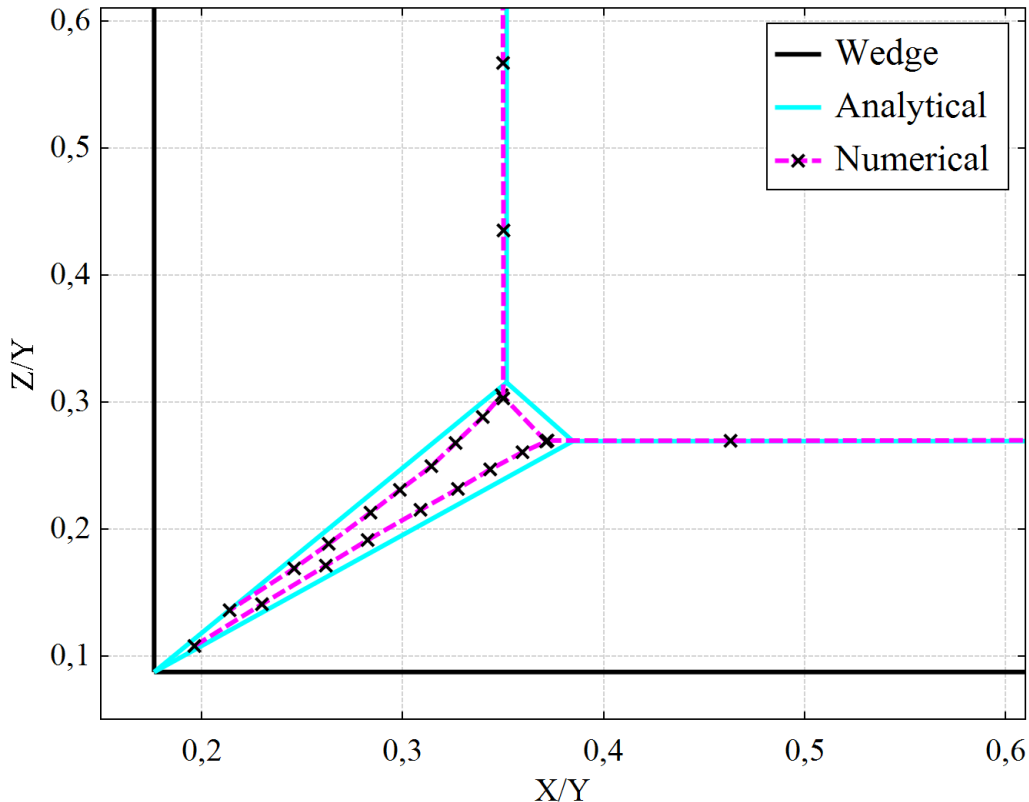


Figure 4.6. Comparison of analytical and numerical results for Case B

Case B has zero sweep, orthogonal dihedral, and asymmetrical wedge angles. Flow has the highest Mach number selected for this study. Flow field structures are found quite similar as given in Figure 4.6. Differently from other cases investigated, the triangular region whose limits are slip lines and Mach stem is estimated bigger by analytical methods. The directions of Mach stems seem to be parallel in both

solutions. Therefore, it can be concluded that analytical methods are prospering in terms of modeling the asymmetrical intersection of wedges for similar cases as in Case B.

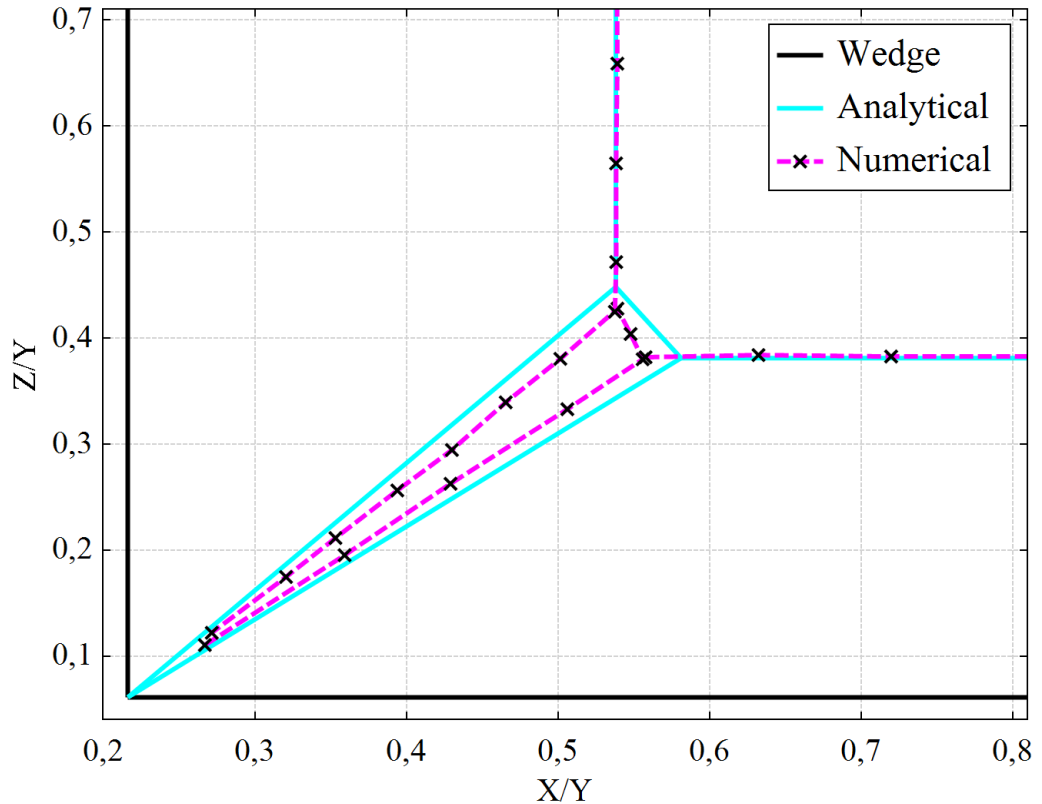


Figure 4.7. Comparison of analytical and numerical results for Case C

Case C has one of the most asymmetrical intersections of wedges when it is compared with other cases. The flow and geometrical properties of Case C are identical with Case Ref. [14] except for one wedge angle. Analytical methods give comparable results with numerical solutions as given in Figure 4.7. Like Case B, analytical solutions guess a bigger triangular zone for Case C. Nonetheless, Mach stems are not parallel to each other. Therefore, it can be concluded that the

asymmetry in the intersection of wedges affects the conformation of analytical and numerical results adversely.

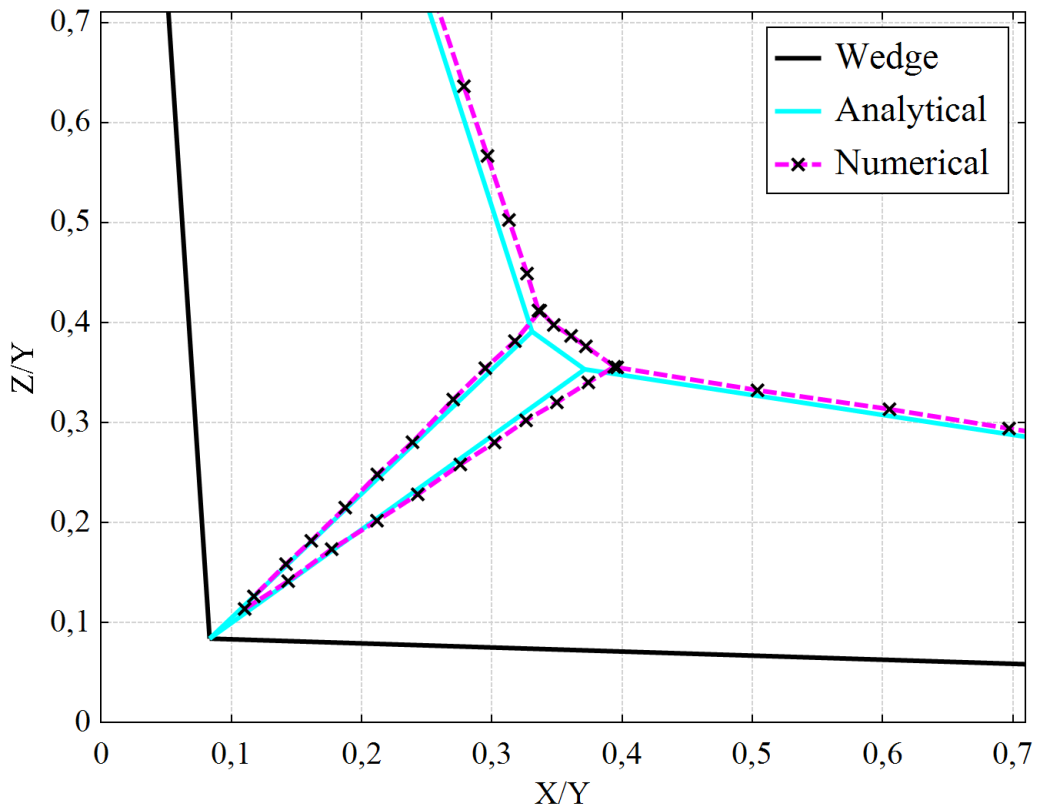


Figure 4.8. Comparison of analytical and numerical results for Case D

Case D has the highest sweep angles among other cases. Other properties of flow and geometry are selected as moderate values. The positions of Mach stem and incident shock waves are found a bit away from the corner in numerical solutions. Though, the agreement between analytical and numerical results is evaluated as very good since the similarity of the shape of flow structures is notable. The comparison of analytical and numerical results can be seen in Figure 4.8.

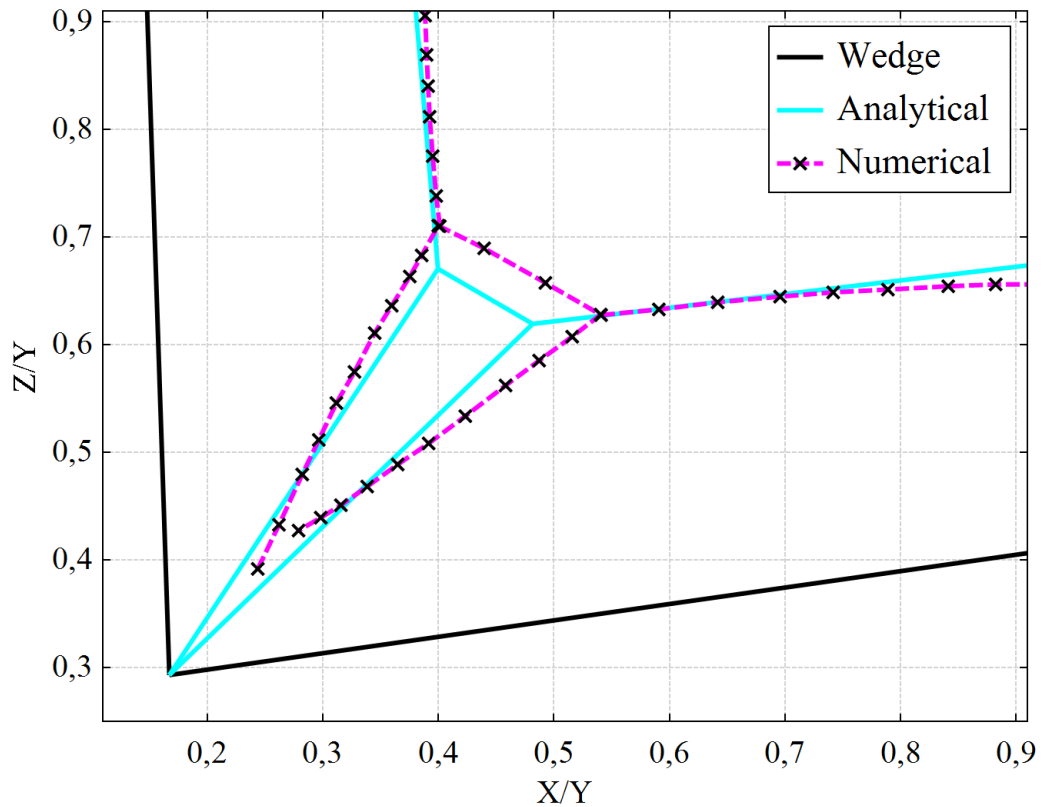


Figure 4.9. Comparison of analytical and numerical results for Case E

Case E is characterized by non-orthogonal dihedral, high wedge, and moderate sweep angles. Together with Case F, Case E is one the cases where the flow is compressed mostly. Mach number of the flow is selected for representation of moderate flow speed. As given in Figure 4.9, the numerical solution indicates a distant Mach stem from the corner and the intersection of slip lines not on the corner. These findings are analogous with the ones of Case Ref [14]. The deviations between analytical and numerical results can be evaluated in the same way with Case Ref [14] as smaller dihedral angles increase the compression and the high compression is pointed out to be a cause of deviation in between analytical and numerical results. Yet, the results are similar in terms of wave structures and analytical results resemble the flow structure adequately.

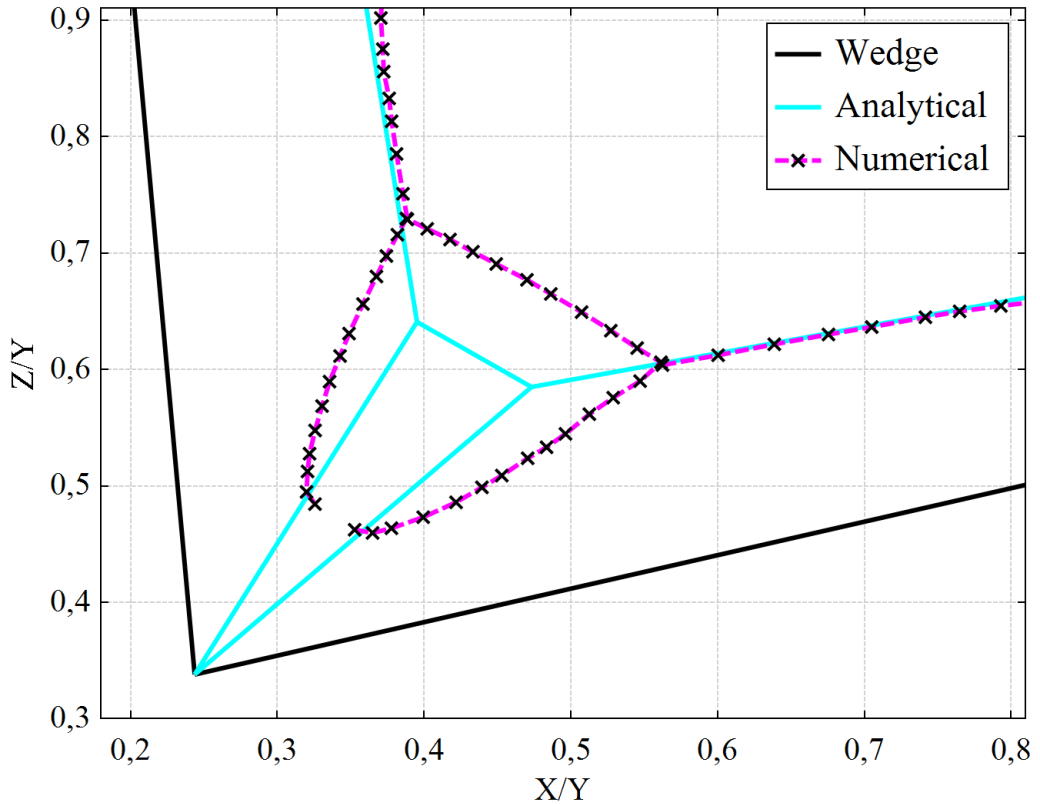


Figure 4.10. Comparison of analytical and numerical results for Case F

In Case F, flow and geometrical parameters are selected to create the highest compression among other cases. This is done by increasing the wedge and decreasing the dihedral angles. It should also be underlined that the Mach number of the flow is also high when compared with other cases. The effects of high compression are already defined and discussed in Cases Ref [14] and E. However, further deviations between analytical and numerical results are obtained for Case F as given in Figure 4.10. Besides a distant Mach stem from the corner, slip lines are found curved in numerical solutions. Curved slip lines are distinctive outcomes of vortices. Indeed, vortices can be identified clearly on velocity contours of numerical solutions given in Figure 5.46. It should also be emphasized that the numerical solutions demonstrate

dense pressure contours in the Mach stem region. Together with apparent vortices, this indicator shows that the flow regions are found remarkably different in numerical solutions and zone descriptions given in Section 2.1 may not be valid or sufficient to describe the flow structure in Case F. As a result, despite other highly compressed cases, analytical results deviate from numerical results significantly in this case. Still, the positions of incident shock waves are found with great accuracy by analytical methods. Thus, it should be underscored that deviations of flow structures in the Mach stem region affect the close region of the corner and have no direct influence on outer zones of flow.

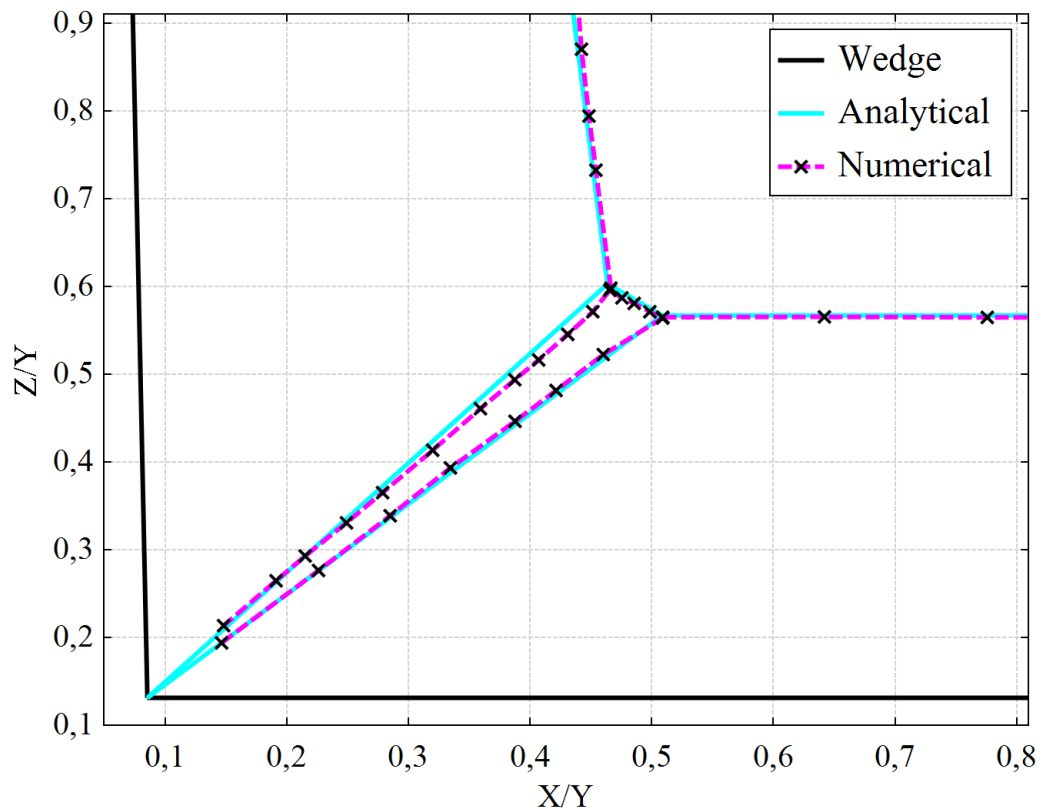


Figure 4.11. Comparison of analytical and numerical results for Case G

Case G has a relatively low Mach number when compared with other cases. Wedge angles are kept small and mildly asymmetrical whereas the dihedral angle is kept orthogonal. Sweep angles are also asymmetrical. The comparison of analytical and numerical results is given in Figure 4.11. This comparison shows that both methods indicate very similar results. Therefore, for similar flow parameters, flow structures can be found with very good accuracy with analytical methods.

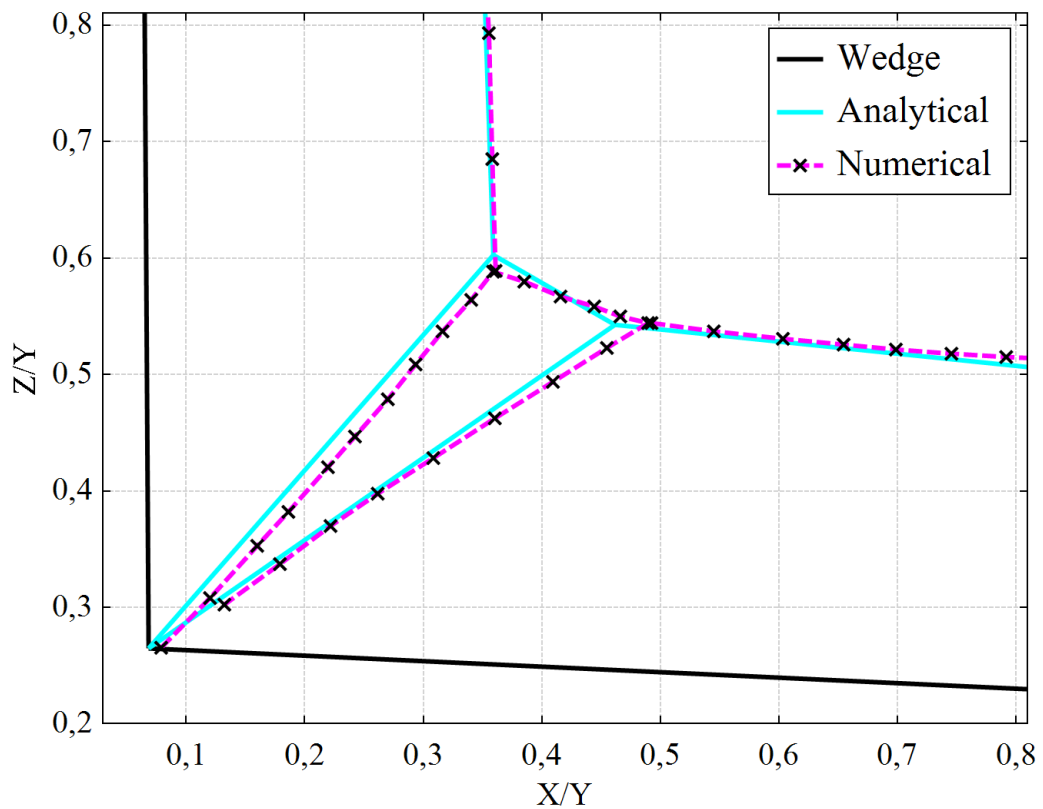


Figure 4.12. Comparison of analytical and numerical results for Case H

Flow and geometrical properties of Case H are selected to create another asymmetrical intersection case. To have such a condition, wedge and sweep angles are adjusted accordingly. The dihedral angle is chosen as orthogonal. The most

distinguishing property of Case H is that only one reflected shock polar curve can be prepared because the subsonic flow is expected after one incident shock wave on the characteristic plane. The shock polar curve for Case H is given in Figure 5.22 It should be noted that shock polar curves can only be prepared for initially-supersonic flow. The comparison of results shows that good agreement is obtained between analytical and numerical solutions. The differences are already discussed as in Cases B and C and comments on asymmetrical intersection are also valid for Case H. Furthermore, it should be emphasized that the analytical solution gives coherent results even in the case for which the preparation of shock polar curves is not possible.

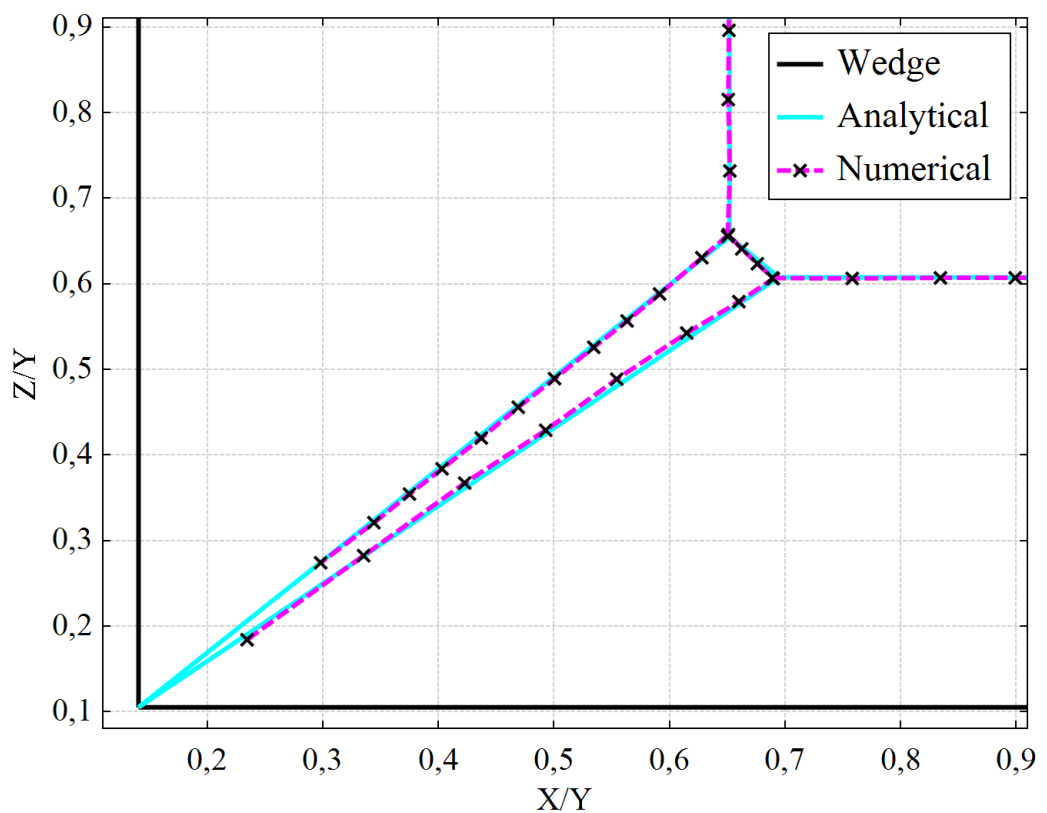


Figure 4.13. Comparison of analytical and numerical results for Case I

Case I is an example of an asymmetrical intersection of wedges with zero sweep and orthogonal dihedral angles with a relatively low Mach number, like Case G. The comparison for Case I shows the perfect agreement of analytical results with numerical ones as shown in Figure 4.13.

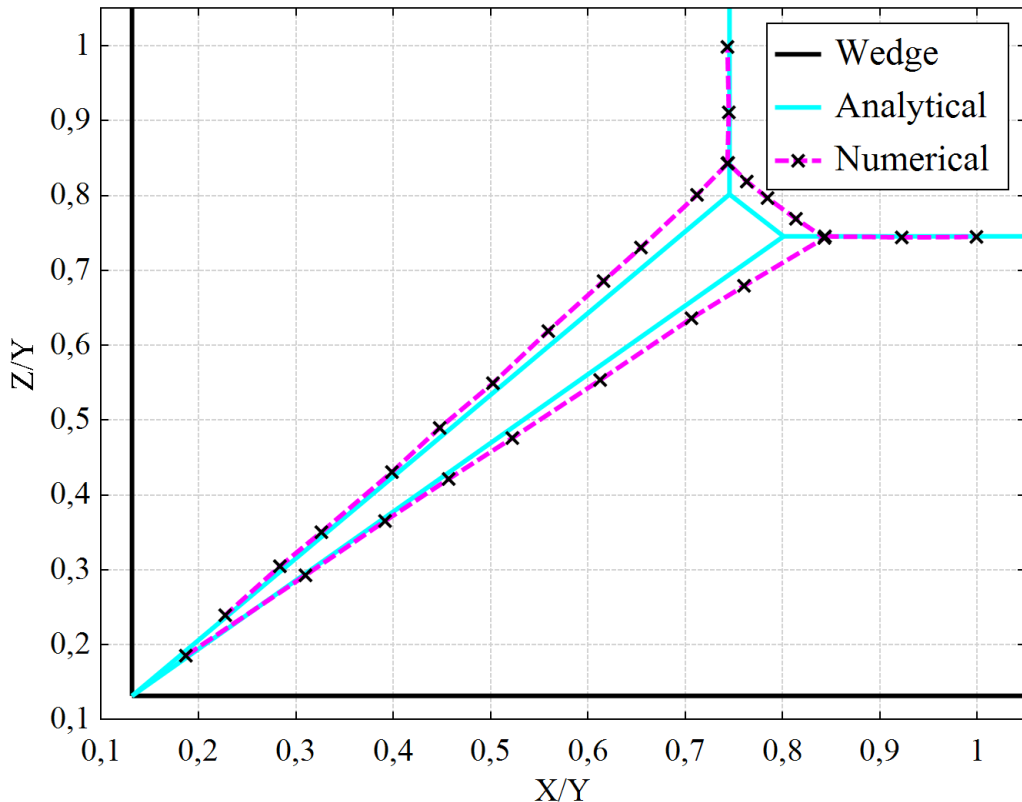


Figure 4.14. Comparison of analytical and numerical results for Case J

Case J represents a low Mach number and symmetrical intersection case with zero sweep and orthogonal dihedral angles. The comparison of results is given in Figure 4.14. Like Case Ref. [17], the analytical results give accurate estimations on positions of wave structures for Case J. A slightly broader triangular region is predicted by numerical solutions indicating mildly curved slip lines and distant Mach

stem from the corner. As the quality of numerical and analytical results are comparable, overall accuracy is evaluated as acceptable.

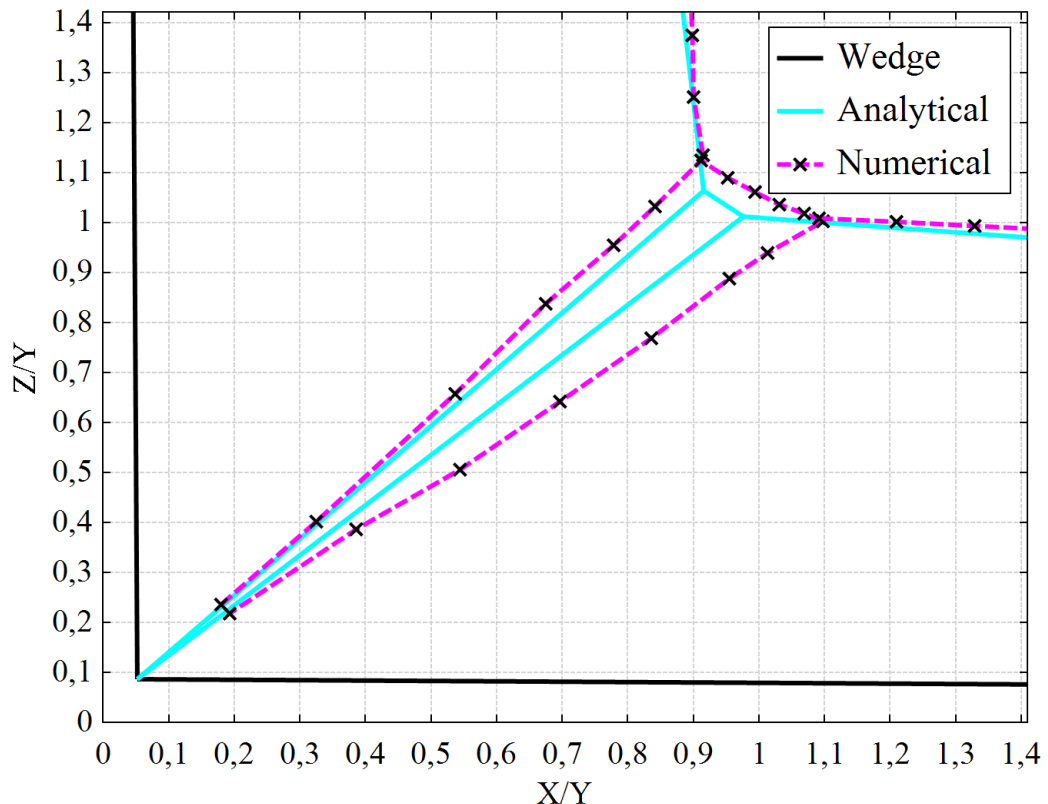


Figure 4.15. Comparison of analytical and numerical results for Case K

Case K has the minimum Mach number among the studied cases. As a result of it, Mach stem is formed at a greater distance from the corner when it is compared with other cases even though very small wedge angles are selected for Case K. Positions of the Mach stem and the incident shock waves are found in good agreement, however, a bigger triangular zone is calculated by numerical solutions as given Figure 4.15. In addition to the reasons mentioned above, several other reasons may explain the deviation. Firstly, the computational domain is kept almost two times

bigger in volume ($7.5 \times 7.5 \text{ mm}$ at the inlet instead of $5 \times 5 \text{ mm}$, see Section 3.4.1) as incident shock waves have higher shock wave angles and their intersection is calculated to be at around 1 in terms of conical coordinates Z/Y and X/Y . Due to this reason, mesh adaptation could be made five times instead of six as in other cases. Hence, the necessary resolution of mesh might not be acquired. Secondly, the slip lines (the one on the right especially, see Figure 5.51) are barely detected and not distinct as in other cases. Thus, its exact position may be determined wrongly.

4.1.3 Comparison of Flow Field with Analytical Results

The problem defined in Case Ref. [17] was used as a validation case by Xiang et al also and the conformity of their analytical results was compared with both numerical and experimental results in Fig. 8 of [31]. Their analytical results are taken from [31], digitized, and compared with the analytical results obtained for this study. The comparison of analytical results is given in Figure 4.16.

The positions of Mach stems are found different. The Mach stem is located further afield from the corner in [31]. It is surprising to obtain dissimilar results since both solutions are based on the principles of the spatial-dimension reduction technique. Moreover, it is also unexpected to see that the same Mach numbers for Mach stems are found in both solutions (1.84 for both, see [31, p. 1477] and Figure 5.9). As the solution steps and intermediate results are neither given in [31] nor in any references containing the same information such as [29], it is not possible to figure out the discrepancy. Still, it is reasonable to expect that an analytical solution should be in better agreement with an inviscid numerical solution rather than the experimental data. This hypothesis also explains the deviation of analytical results from experimental data and almost perfect fit of them with the numerical solutions for Case Ref. [17]. However, the opposite was shown to be true in Fig. 8 of [31]. In other words, analytical results were in better conformity with experimental data. Thus, there is a contradiction that can not be enlightened with the information available.

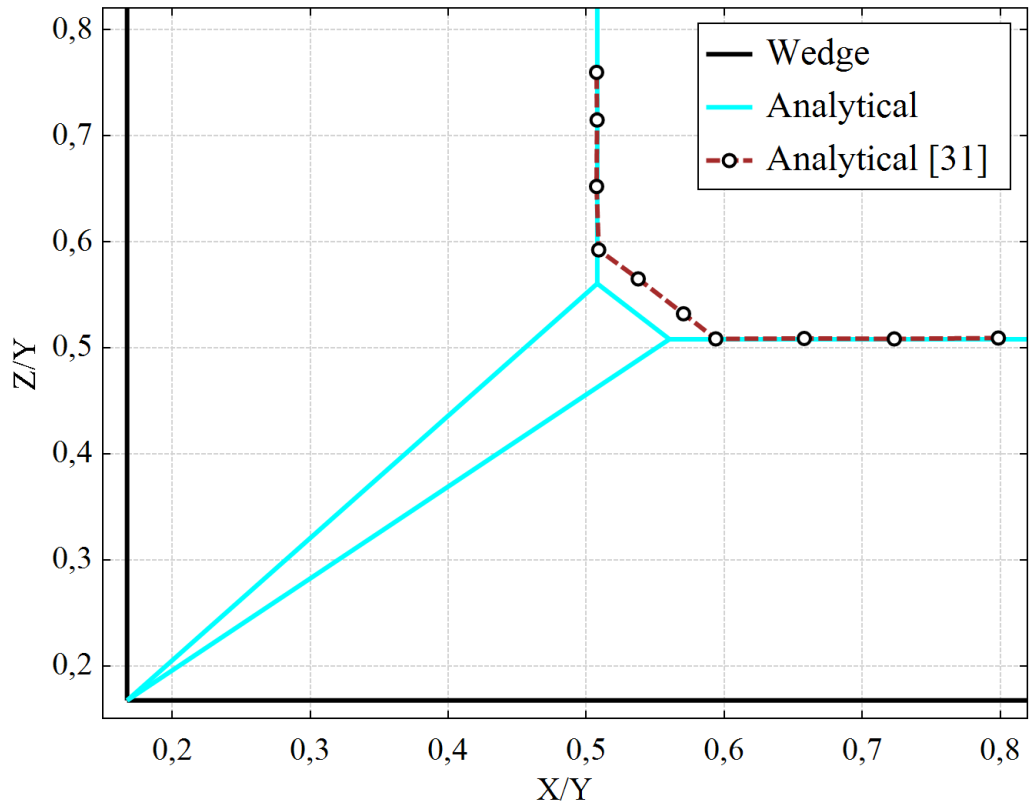


Figure 4.16. Comparison of analytical results for Case Ref. [17]

4.2 Pressure Ratios Across Mach Stem

Mach stem calculations are compared by pressure ratios across Mach stem via numerical and analytical solutions.

$$Difference (\%) = 100 \frac{\zeta_m - \zeta_{numerical}}{\zeta_{numerical}} \quad (48)$$

Difference percents are calculated as given in Equation (48). ζ_m is already defined in Equation (39) and demonstrates the pressure ratio across Mach stem found by analytical methods. $\zeta_{numerical}$ defines the pressure ratio across Mach stem found by numerical methods (see Section 3.4.3.5 for details).

No pressure data which was used during the preparation of Figure 2.4 is presented in [17]. Although pressure measurements were presented in [14], they are demonstrated in the form of static to total pressure ratios. As total and static pressure both change after a shock wave, this pressure ratio information cannot be used for comparison of shock strength across Mach stem. Nevertheless, no information of static and/or total pressures on the plane of investigation is provided. Therefore, pressure ratio comparisons for Cases Ref. [17] and [14] are done by using numerical and analytical solutions.

Pressure ratio differences are given in Table 4.2. Flow field determination should include physical properties of Mach stem region (triangular zone whose limits are slip lines and Mach stem) besides its shape and displacement which are already given in discussed in previous sections. Table 4.2 indicates that pressure ratio across Mach stem can be found with approximately $2 \pm 10\%$ difference by analytical methods when compared to numerical solutions. The difference is increased as the intersection of wedges becomes asymmetrical which is the condition for Cases C and H. It is also shown that for cases whose flow fields can be approximated poorly with analytical methods such as Case F, pressure ratio findings are still satisfactorily close. Such an agreement proves the applicability of the method used.

Table 4.2 Comparison of pressure ratios across Mach stem

Case #	Numerical	Analytical	Difference (%)
Ref. [17]	3.695	3.786	2.463
Ref. [14]	4.778	4.709	-1.444
A	4.773	4.783	0.210
B	4.889	5.210	6.566
C	3.353	3.783	12.824
D	2.077	2.042	-1.685
E	5.593	5.508	-1.520
F	9.407	8.794	-6.516
G	2.445	2.570	5.112
H	3.671	4.058	10.542
I	2.543	2.636	3.657
J	2.465	2.479	0.568
K	1.632	1.629	-0.184

In several studies [29, 31], the analytical results are compared with numerical solutions in terms of Mach stem velocity. However, pressure ratios across Mach stem are preferred in this work. Instead of performing unsteady numerical solutions as in [29, 31], steady numerical solutions are done. As a result, the velocity of the Mach stem cannot be obtained directly from numerical solutions. Therefore, the accuracy of analytical results should be tested in terms of other flow properties than velocity. On the other hand, the analytical method approximates the steady-state problem as if it is pseudo-steady by doing the Galilean transformation characteristic plane. Thus, a virtual velocity component is calculated which represents the Mach stem velocity in the characteristic plane. Mach stem velocity can be used to find the pressure ratios across Mach stem itself since static properties of flow do not change with Galilean

transformation. Thus, pressure ratio comparison is chosen to be convenient with both numerical and analytical solution procedures.

4.3 Discussion of Results

Types of reflections (i.e., interaction) are found by using shock polar analysis in the characteristic plane. Estimated types are found to be consistent with both experimental and numerical findings. Thus, shock polar analysis for the determination of interaction type can be used for corner flow problems. Shock polar curves for cases are given in Appendix B.

Triple point trajectories are assumed to form slip lines when MR occurs. This assumption is validated by numerical solutions by comparing the velocity and pressure field on the plane of investigation. Slip lines are also called entropy waves and in the 3D domain, they create surfaces originating at the point of the cross-section of two wedges. Across slip surfaces, continuous pressure and discrete velocity fields are expected. Since numerical solutions are obtained by using mesh adaptation based on velocity gradient, iso-pressure lines should cross the iso-velocity lines if a slip surface exists. In addition, changes in basic characteristics of isolines can also be associated with such formation. Indeed, in the region where slip lines are expected to be seen, both situations are observed. Except for the region whose boundaries are reflected shock waves, Mach stems, and wedge surfaces, pressure and velocity field are found quite similar. Inside this region, however, an abrupt change in velocity field is captured which resembles a planar surface in most cases. But, the pressure field does not indicate a sharp change. Therefore, it can be concluded that slip lines (i.e., surfaces in the 3D domain) are generated in the flow field and findings from analytical and numerical solutions are similar in most cases.

In studies on corner flow problems, it is common to classify the flow structures according to their conical invariance. Being conically invariant (or simply conical) for corner flow problems defines that the flow properties would not vary if space

variables were non-dimensionalized by the undisturbed flow direction. In other words, flow structures are observed at the same dimensionless positions on any plane perpendicular to the upstream flow direction if the problem is conically invariant. Several researchers [14, 16, 17] have been used this classification to identify the characteristics of interaction as dominated by inviscid or viscous effects. As flow structure is found conically invariant in a corner flow problem, this means that the inviscid structure of interaction is dominant and viscous effects can be neglected. In this work, flow is assumed to be inviscid in both analytical and numerical solutions (see Section 3.1). This assumption indicates that analytical and numerical solutions are also conically invariant. By using this condition, the numerical solution domain can be kept small. Likewise, one analytical solution to determine the flow structure on a plane of investigation is sufficient to determine the properties of the whole flow field. On the other hand, inviscid numerical and analytical solutions should be expected to deviate from real conditions as the flow becomes less conical.

Numerical solutions are made with geometrical and flow parameters which are found to create a Mach type reflection for all cases. This selection was done on purpose due to two main reasons. Firstly, the Mach reflections are more common in real flight conditions because they begin to form when the deflection of flow is above a certain angle. Approximate wedge angle limits for different Mach numbers are given in Table 4.3. A similar discussion was also made in [21] and the limit angles of wedges for symmetrical intersection are given as a function of upstream Mach number on a graph. An adaptation of this graphic demonstration can be seen in Figure 4.17. It is less than 4° for most of the cases. It should also be emphasized that an increase in sweep angle also increases the possibility of MR formation. Secondly, in the case of RR formation, the solution procedure becomes simpler because no Mach stem calculations are needed for flow field determination and all the flow parameters can be obtained from shock polar curves prepared for the characteristic plane.

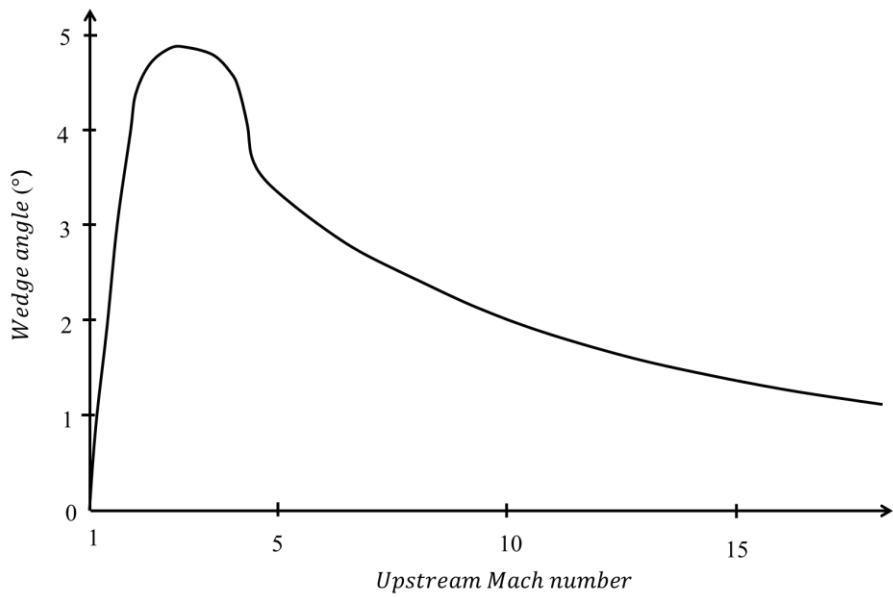


Figure 4.17. Maximum symmetrical wedge angle for RR / adapted from [21]

Table 4.3 Limits of wedge angles for RR formation

Mach number	$\theta_1 = \theta_2$ (°)	$\lambda_1 = \lambda_2$ (°)	v (°)
1.5	2.40	0	90
2	3.75		
3	4.25		
4	3.80		
5	3.40		

The outcome of analytical results demonstrates that calculated flow fields are qualitatively similar in terms of Mach stem, slip line, and incident shock wave locations with both numerical and experimental data. Thus, the “characteristic skeleton of wave structures [14, p. 488]” can successfully be obtained by analytical methods.

It is shown that analytical results give very close solutions with most of the numerical solutions. However, in some cases, the location of the Mach stem was found closer to wedge surfaces and narrower in analytical solutions than numerical solutions. In addition, in those cases, slip lines show curved structures rather than linear and intersect at a point above the wedge intersection line. This situation can be explained by vorticity which can be produced by a strong compression region between reflected shock wave and slip lines. A vortex generation in the region between reflected shock and slip lines would result in a stretched region (See Figure 2.2, region 2 for the mentioned zone). Thus, a wider and distant Mach stem and curved slip lines (i.e., triple point trajectories) would be expected. Indeed, the presence of vortices was reported by Watson and Weinstein in [16] and vortex structures were visualized by several experimental techniques (by using pressure data and electron beam photographs of [16, p. 1282]). In addition, it should be emphasized that vortex generation in the close region of the corner was observed for Re number (3.7×10^6) above limit defined in [17] which was 3×10^6 . Therefore, it is reasonable to explain the above-mentioned deviation by vortex generation even though it was reported that in turbulent cases, only weak vortex structures were observed ([17, p. 656]). A similar consideration was also expressed in [14]. Charwat and Redekeopp stated that slip surfaces create an apparent cross-stream vorticity gradient, and such an effect should be regarded for an accurate analysis of the corner flow problem.

The basics of the spatial-dimension reduction technique are used in this study. It is expected to see very similar or the same results for analytical solutions executed by different sources. However, a surprising difference was shown and discussed in Section 4.1.3. When solution methodology and equations which are available in the literature are investigated, it is realized that the slip line angles are found by using different equations. Equations (49) and (50) are taken from [28, 31] and adapted for their consistency with the present study. The equations which are used for the present study were given in Equations (37) and (38) in Section 3.3.3.

$$\tan(\chi_1) = \frac{M_m + \sec(\eta + \theta_{w2})M_{s2}}{-\tan(\eta + \theta_{w2})M_m} \quad (49)$$

$$\tan(\chi_2) = \frac{M_m - \sec(\theta_{w2})M_{s2}}{\tan(\theta_{w2})M_m} \quad (50)$$

The equations seem distinctive. However, a moving shock wave diffracted by a wedge problem can be solved by using ray-shock solution methods which are based on the geometric relations between upstream and diffracted shock waves. Therefore, the discrepancy can be understood better by comparison of individual results. The slip line angles calculated by Equations (37), (38) and Equations (49), (50) are compared for selected cases and given in Table 4.4.

Table 4.4 Comparison of slip line angles found by different equations

Case #	Equations (37), (38)		Equations (49), (50)	
	χ_1 (°)	χ_2 (°)	χ_1 (°)	χ_2 (°)
Ref. [17]	3.453	3.453	3.453	3.453
B	6.591	0.946	22.785	0.949
C	7.496	0.322	29.130	0.326
D	3.226	3.681	2.410	3.674
H	0.378	11.101	-17.827	11.127

When Table 4.4 is investigated, it is apparent that when the interaction becomes asymmetrical, the dissimilarity in findings for the first slip lines increases. However, the angles of the second slip lines are found very close by Equations (37) and (50) for all the cases. Such a condition may be explained by a typo made when Equation (49) was being defined. Indeed, the difference found for the first slip line angle disappears when the term M_{s2} in Equation (49) is changed with M_{s1} . Therefore, it

can be concluded that both equations are valid, however, the second slip line angle is not defined correctly in [28, 31].

By following the outcomes of the cases studied, it can be stated that the analytical methods are applicable up to the separation point of incident shock waves as equations used for analytical methods diverge beyond this point. The separation point defines the maximum angle of deflection (i.e., wedge) before the shock wave detaches from the edge and a bow shock occurs. This point can be found by reading the highest possible deflection angle on the shock polar curves. It should be noted that it is a function of the Mach number and increases as the Mach number rises. In other words, analytical methods have a broader application range for higher Mach numbers. However, it should be kept in mind that as the compression of flow increases, analytical solutions become less accurate as discussed in previous sections. Moreover, to identify the limits of the applicability of the analytical methods, a more comprehensive study must be performed. This could be done by changing only one variable at once and by defining the acceptable deviations of analytical results from numerical ones. These are left as further work and kept out of the scope of this study.

It is realized that in some cases, incident shock waves show curved structures in numerical solutions. Due to this curvature, a discrepancy between analytical and numerical solutions is observed. In addition to curved shock waves, velocity and pressure gradients are also distinguished in contour plots. It is uncommon to see such a shock wave shape since all the geometrical properties are defined as lines and planes. Similarly, no gradient in flow properties is expected in those regions. This condition is observed because of the symmetry boundary condition defined for the outer surfaces of the computation domain. Since symmetry condition forces the derivative of flow properties to be diminished at boundaries, shock waves must be normal to outer surfaces. When sweep and dihedral angles are other than 0 and 90°, incident shock waves cross the outer boundary with angles other than normal, and that difference is observed in such cases. Thus, this curvature is fictitious and not correct in physical means. This problem can be overcome by using non-reflecting

type boundary conditions instead of symmetry or moving the outer boundaries far away. Outcomes of numerical solutions presented are still useful since no direct effect of forced boundary condition is observed in the Mach stem region. This is determined by checking the conformity of incident shock waves in close regions of Mach stem for analytical and numerical solutions in flow field demonstrations. Therefore, this inconvenience is neglected.

Solution duration for analytical methods is longer than expected. When analyzed, it is recognized that two main solution steps significantly prolong the solution interval. These solution steps are the preparation of shock polar diagrams and the solution of Mach stem (i.e., C.C.W. solution) equations. Shock polar diagrams are based on pressure ratio values for deflection angles. Since polar diagrams can be formed as a function of shock angles for both pressure ratios and deflection angles, shock polar diagrams are generated by using point values found for every increment of possible shock wave angles. Thus, smaller increments result in longer times. During the solutions, 100 increments are used for shock angle intervals. During the solution of equations for Mach stem, a numerical trial-and-error method whose acceptance criteria was determined as 0.01° for Equations (34), (35), and (36) is used. This method is found easier than the analytical definition of equations since exponential and integral definitions are done for equations to be solved. During the trial-and-error procedure, increment of change of input parameter (i.e., the velocity of Mach stem) is decreased as a smaller difference for acceptance is found. Thus, an adaptive approach is used to lessen the solution time. However, it is still time-consuming and spends approximately two-thirds of the total solution time. Total iterations needed for the solution of C.C.W. equations are between 30 to 40 for the required accuracy level.

CHAPTER 5

CONCLUSION AND FURTHER WORK

In this study, a series of analytical solutions based on the “spatial-dimension reduction” method defined by Yang et al are done for three-dimensional SSI problems. Analytical solution procedure with assumptions and simplifications is defined in detail. Numerical solutions are also obtained for comparison purposes with both analytical and existing experimental data. The accuracy of the analytical model is determined by comparing the results with experimental, numerical, and analytical data. Comparison is done qualitatively for flow field shape and quantitatively for pressure ratio across Mach stems. Analytically-calculated flow fields and gathered experimental, numerical, and analytical data are visualized and presented in dimensionless coordinates and the pressure ratio across Mach stem results are tabulated. Differences and deviations of results are explained with possible reasons and commented on. It is concluded that the analytical solution method presented in this work can be used successfully for flow field determination (i.e., the position of Mach stem, slip lines, and incident shock waves) the cases where compression effects are small to moderate. For cases with strong compression, vortex structures may be formed and due to this reason, the flow field estimations may become less accurate. Nevertheless, pressure ratio calculations across the Mach stem of analytical methods give results with differences of $2 \pm 10\%$ when compared with numerical methods and no increase in deviation is apparent for cases with strong compression effects being dominant.

Future work that can be done are listed as follows:

- 1- The solution time for the analytical solution is approximately 90 seconds. Although it is already short when compared with other solution methods, it is not optimized for pace. When optimized, solution time is estimated to be

between 5 to 15 seconds. Thus, it can be shortened by improving the solution techniques used.

- 2- Inviscid solutions can be improved by the addition of vorticity and boundary layer displacement equations which can increase the accuracy of detection of slip lines and Mach stem structures.
- 3- Solutions on the characteristic plane can be extended for reflected shock waves and their demonstration of the plane of investigation.
- 4- A detailed investigation can be performed to study the effects of change of geometrical or flow parameters. To do such work, a parametric input should be done to code. By using the results of such a work, a flow regime may be proposed to an aircraft for required flow properties in its air duct. Similarly, the preliminary design of an air duct whose requirements are already defined can be done by using the results of this work.
- 5- The applicability limits of the analytical methods can be determined by doing comparisons with numerical results. For this purpose, the effects of change of every variable which are defined as the wedge, sweep, dihedral angles, and Mach number should be investigated independently.

REFERENCES

- [1] G. Ben-Dor, Shock Wave Reflection Phenomena, Second ed., Berlin: Springer, 2007.
- [2] H. G. Hornung, H. Oertel and R. J. Sandeman, "Transition to Mach reflexion of shock waves in steady and pseudosteady flow with and without relaxation," *Journal of Fluid Mechanics*, vol. 90, no. 3, pp. 541-560, 1979.
- [3] L. T. Felthun and B. W. Skews, "Dynamic Shock Wave Reflection," *AIAA Journal*, vol. 42, no. 8, pp. 1633-1639, 2004.
- [4] L. F. Henderson and A. Lozzi, "Experiments on transition of Mach reflexion," *Journal of Fluid Mechanics*, vol. 68, no. 1, pp. 139-155, 1975.
- [5] H. G. Hornung and M. L. Robinson, "Transition from regular to Mach reflection of shock waves Part 2. The steady-flow criterion," *Journal of Fluid Mechanics*, vol. 123, pp. 155-164, 1982.
- [6] H. G. Hornung and J. R. Taylor, "Transition from regular to Mach reflection of shock waves Part 1. The effect of viscosity in the pseudosteady case," *Journal of Fluid Mechanics*, vol. 123, pp. 143-153, 1982.
- [7] M. S. Ivanov, S. F. Gimelshein and G. N. Markelov, "Statistical Simulation of the Transition between Regular and Mach Reflection in Steady Flows," *Computers and Mathematics with Applications*, vol. 35, no. 1/2, pp. 113-125, 1998.
- [8] C. A. Mouton, *Thesis of Doctorate "Transition between Regular Reflection and Mach Reflection in the Dual-Solution Domain"*, Pasadena, California: California Institute of Technology, 2006.
- [9] R. Kawamura and H. Saito, "Reflection of Shock Waves-1 Pseudo-Stationary Case," *Journal of the Physical Society of Japan*, vol. 11, no. 5, pp. 584-592, 1956.
- [10] T. J. Goldberg and J. N. Hefner, "Starting Phenomena for Hypersonic Inlets with Thick Turbulent Boundary Layers at Mach 6," National Aeronautics and Space Administration, Washington D.C., 1971.
- [11] M. S. Holden, J. R. Moselle and J. Lee, "Studies of Aerothermal Loads Generated in Regions of Shock/Shock Interaction in Hypersonic Flow,"

National Aeronautics and Space Administration, Hampton, Virginia, 1991.

- [12] B. E. Edney, "Effects of Shock Impingement on the Heat Transfer around Blunt Bodies," *AIAA Journal*, vol. 6, no. 1, pp. 15-21, 1968.
- [13] C. Wang, R. Yang and Z. Jiang, "The Mechanism of Three-Dimension Steady Shock Wave Interaction," in *ASME 5th Joint US-European Fluids Engineering Division Summer Meeting*, Montreal, 2018.
- [14] A. F. Charwat and L. G. Redekeopp, "Supersonic Interference Flow along the Corner of Intersection Wedges," *AIAA Journal*, vol. 5, no. 3, pp. 480-488, 1966.
- [15] R. J. Cresci, S. G. Rubin, C. T. Nardo and T. C. Lin, "Hypersonic Interaction Along a Rectangular Corner," *AIAA Journal*, vol. 7, no. 12, pp. 2241-2246, 1969.
- [16] R. D. Watson and L. M. Weinstein, "A Study of Hypersonic Corner Flow Interactions," *AIAA Journal*, vol. 9, no. 7, pp. 1280-1286, 1971.
- [17] J. E. West and R. H. Korkegi, "Supersonic Interaction in the Corner of Intersecting Wedges at High Reynolds Number," *AIAA Journal*, vol. 10, no. 5, pp. 652-656, 1972.
- [18] S. G. Rubin, T. C. Lin, M. Pierucci and S. Rudman, "Hypersonic Interactions near Sharp Leading Edges," *AIAA Journal*, vol. 7, no. 9, pp. 1744-1751, 1969.
- [19] P. Kutler, "Supersonic Flow in the Corner Formed by Two Intersecting Wedges," *AIAA Journal*, vol. 12, no. 5, pp. 577-578, 1974.
- [20] P. Kutler and H. Lomax, "Shock-Capturing, Finite-Difference Approach to Supersonic Flows," *Journal of Spacecraft and Rockets*, vol. 8, no. 12, pp. 1175-1182, 1971.
- [21] F. Marconi, "Supersonic, Inviscid, Conical Corner Flowfields," *AIAA Journal*, vol. 18, no. 1, pp. 78-84, 1980.
- [22] G. Moretti, B. Grossman and F. J. Marconi, "A Complete Numerical Technique for the Calculation of Three-Dimensional Inviscid Supersonic Flows," in *AIAA 10th Aerospace Sciences Meeting*, San Diego, California, 1972.
- [23] T. Meguro, K. Takayama and O. Onodera, "Three-dimensional shock wave reflection over a corner of two intersecting wedges," *Shock Waves*, vol. 7, pp. 107-121, 1997.

- [24] Y. P. Goonko, A. N. Kudryavtsev and A. Chpoun, "3D interaction of shock waves in corner flow," in *Shock Waves*, Beijing, 2005.
- [25] D. J. Azevedo and C. S. Liu, "An Analytical Approach to the Prediction of Shock Patterns in Bounded High-Speed Flows," in *AIAA 20th Fluid Dynamics, Plasma Dynamics and Lasers Conference*, New York, 1989.
- [26] D. J. Azevedo and C. S. Liu, "Engineering Approach to the Prediction of Shock Patterns in Bounded High-Speed Flows," *AIAA Journal*, vol. 31, no. 1, pp. 83-90, 1993.
- [27] Y. Yang, C. Wang and Z. Jiang, "Analytical and numerical investigations of the reflection of asymmetric nonstationary shock waves," *Shock Waves*, vol. 22, pp. 439-449, 2012.
- [28] G. Xiang, C. Wang, H. Teng, Y. Yang and Z. Jiang, "Study on Mach stems induced by interaction of planar shock waves on two intersecting wedges," *Acta Mechanica Sinica*, vol. 32, no. 3, pp. 362-368, 2015.
- [29] G. Xiang, C. Wang, Z. Hu, X. Li and Z. Jiang, "Theoretical solutions to three-dimensional asymmetrical shock/shock interaction," *Science China Technological Sciences*, vol. 59, pp. 1208-1216, 2016.
- [30] G. Xiang, C. Wang, H. Teng and Z. Jiang, "Three-dimensional shock wave configurations induced by two asymmetrical intersecting wedges in supersonic flow," *Shock Waves*, vol. 28, no. 2, pp. 311-319, 2018.
- [31] G. X. Xiang, C. Wang, H. H. Teng and Z. L. Jiang, "Investigations of Three-Dimensional Shock/Shock Interactions over Symmetrical Intersecting Wedges," *AIAA Journal*, vol. 54, no. 5, pp. 1472-1481, 2016.
- [32] Z. Han and X. Yin, *Shock Dynamics / Fluid Mechanics and Its Applications*, vol. 11, R. Moreau, Ed., Beijing: Springer Science+Business Media, 1993.
- [33] M. J. Zucrow and J. D. Hoffman, *Gas Dynamics*, vol. 1, New York: John Wiley & Sons, Inc., 1976.
- [34] M. H. Aksel, Notes on Fluid Dynamics, 4 ed., vol. 2, Ankara: Department of Mechanical Engineering Middle East Technical University, 2018.
- [35] M. H. Aksel, *ME 503 Advanced Gas Dynamics Lecture Notes*, Vols. One-Dimensional Unsteady Flows (Lecture 10), Middle East Technical University, 2019 / Spring.

- [36] Z.-Y. Han and X.-Z. Yin, "Geometrical Shock Dynamics," in *Handbook of Shock Waves, Three Volume Set*, G. Ben-Dor, O. Igra and T. Elperin, Eds., San Diego, Academic Press, 2001, pp. 485-552.
- [37] C. Tomasi, *COMPSCI 527 Computer Vision Lecture Notes*, vol. Vector Representation of Rotations, Duke University, Fall 2013.
- [38] ANSYS, Inc., "ANSYS FLUENT Theory Guide Release 14.0," ANSYS, Inc., Canonsburg, 2011.
- [39] E. Morishita, "Analytical Formula of Shock-Wave Structure for Pr=3/4," *Transactions of the Japan Society for Aeronautical and Space Sciences*, vol. 47, no. 158, pp. 287-287, 2005.
- [40] W. Ziniu, X. Yizhe, W. Wenbin and H. Ruifeng, "Review of shock wave detection method in CFD post-processing," *Chinese Journal of Aeronautics*, vol. 26, no. 3, pp. 501-5013, 2013.

APPENDICES

A. Sample Calculations for Analytical Solutions

Analytical solutions are done by using SMath Studio Desktop 0.99.7822. SMath Studio is free software that can be downloaded directly from its website. Its design and language resemble commercial software MathCAD. In addition to the built-in solver library, other solvers developed or found can be used as plug-ins. Owing to its paper-like GUI, the presentation and debugging of coding is easy.

Screenshots from sample calculations for analytical solutions of [17] are given from Figure 5.1 to Figure 5.12.

Geometrical parameters and flow properties

$$\theta_1 := 9.5 \text{ deg} \quad \theta_2 := 9.5 \text{ deg} \quad \lambda_1 := 0 \text{ deg} \quad \lambda_2 := 0 \text{ deg} \quad v := 90 \text{ deg}$$

$$T_0 := 300 \text{ K} \quad M_a := 28.96 \frac{\text{g}}{\text{mol}} \quad R := 8314 \frac{\text{joule}}{\text{kmol K}} \quad \gamma := 1.4 \quad Flow := \begin{bmatrix} 0 \\ 1 \\ 0 \end{bmatrix} \quad M_0 := 3$$

Characteristic directions and corresponding Mach numbers

Definition of resultant of a vector

$$Res(Dir) := \sqrt{Dir_1^2 + Dir_2^2 + Dir_3^2}$$

$$Z := \begin{bmatrix} 0 \\ \sin(\lambda_1) \\ \cos(\lambda_1) \end{bmatrix} = \begin{bmatrix} 0 \\ 0 \\ 1 \end{bmatrix} \quad X := \begin{bmatrix} 1 \cdot \sin(v) \cdot \cos(\lambda_2) \\ \sin(\lambda_2) \\ \cos(v) \cdot \cos(\lambda_2) \end{bmatrix} = \begin{bmatrix} 1 \\ 0 \\ 0 \end{bmatrix} \quad Z_0 := \begin{bmatrix} 0 \\ 0 \\ 1 \end{bmatrix} \quad X_0 := \begin{bmatrix} 1 \\ 0 \\ 0 \end{bmatrix} \quad Y_0 := \begin{bmatrix} 0 \\ 1 \\ 0 \end{bmatrix}$$

$$Z_{wedge} := \begin{bmatrix} \sin(\theta_1) \\ \cos(\theta_1) \\ 0 \end{bmatrix} = \begin{bmatrix} 0.165 \\ 0.9863 \\ 0 \end{bmatrix} \quad X_{wedge} := \begin{bmatrix} 0 \\ \cos(\theta_2) \\ \sin(\theta_2) \end{bmatrix} = \begin{bmatrix} 0 \\ 0.9863 \\ 0.165 \end{bmatrix}$$

$$Dir_{wedge} := \frac{(Z \times Z_{wedge}) \times (X \times X_{wedge})}{Res((Z \times Z_{wedge}) \times (X \times X_{wedge}))} = \begin{bmatrix} 0.162845 \\ 0.97312 \\ 0.162845 \end{bmatrix}$$

Angle of pressure wave when no flow deflection is observed.

$$\mu_0 := \arcsin\left(\frac{1}{M_0}\right) = 19.4712 \text{ deg}$$

$$\beta_1 := \text{solve} \left(\tan(a) \cdot \left(\frac{\gamma+1}{2} \cdot \frac{M_0^2}{(M_0 \cdot \sin(a))^2 - 1} - 1 \right) - \cot(\theta_1); a; \mu_0 \cdot 1.01; 90 \text{ deg} \right) = \begin{bmatrix} 26.9308 \\ 86.5966 \end{bmatrix} \text{ deg}$$

$$\beta_2 := \text{solve} \left(\tan(a) \cdot \left(\frac{\gamma+1}{2} \cdot \frac{M_0^2}{(M_0 \cdot \sin(a))^2 - 1} - 1 \right) - \cot(\theta_2); a; \mu_0 \cdot 1.01; 90 \text{ deg} \right) = \begin{bmatrix} 26.9308 \\ 86.5966 \end{bmatrix} \text{ deg}$$

$$\beta_1 := \min(\beta_1) = 26.9308 \text{ deg} \quad \beta_2 := \min(\beta_2) = 26.9308 \text{ deg}$$

Figure 5.1. Screenshot of analytical solution procedure / 1

$$Z_{char} := \begin{bmatrix} \sin(\beta_1) \\ \cos(\beta_1) \\ 0 \end{bmatrix} = \begin{bmatrix} 0.4529 \\ 0.8916 \\ 0 \end{bmatrix} \quad X_{char} := \begin{bmatrix} 0 \\ \cos(\beta_2) \\ \sin(\beta_2) \end{bmatrix} = \begin{bmatrix} 0 \\ 0.8916 \\ 0.4529 \end{bmatrix}$$

$$Dir := \frac{(Z \times Z_{char}) \times (X \times X_{char})}{Res((Z \times Z_{char}) \times (X \times X_{char}))} = \begin{bmatrix} 0.4126 \\ 0.8121 \\ 0.4126 \end{bmatrix}$$

$$M_{c,d} := \frac{Dir \cdot M_0 \cdot Flow}{Res(Dir)} \cdot Dir \quad Res(M_{c,d}) = 2.4364$$

$$V_{c,d} := Res(M_{c,d}) \cdot \sqrt{T_0 \cdot Y \cdot \frac{R}{M_a}} = 846.0235 \frac{\text{m}}{\text{s}}$$

$$M_{c,p} := M_0 \cdot Flow - M_{c,d} \quad Res(M_{c,p}) = 1.7504$$

$$X_{c,d} := \frac{Dir \cdot X}{Res(Dir)} \cdot Dir = \begin{bmatrix} 0.1702 \\ 0.3351 \\ 0.1702 \end{bmatrix} \quad X_{c,p} := X - X_{c,d} = \begin{bmatrix} 0.8298 \\ -0.3351 \\ -0.1702 \end{bmatrix}$$

Defines the unit vector of decomposed Mach number in characteristic plane, occurred due to theta 2

$$Dir_{Ms2} := \frac{X_{c,p}}{Res(X_{c,p})} = \begin{bmatrix} 0.9109 \\ -0.3678 \\ -0.1869 \end{bmatrix}$$

$$\alpha_2 := \text{solve} \left(\frac{|X_{c,p} \cdot M_{c,p}|}{Res(M_{c,p}) \cdot Res(X_{c,p})} - \cos(\alpha_2); \alpha_2; 0; \text{pi} \right) = 50.9186 \text{ deg}$$

$$\delta_2 := \text{solve} \left(\tan(\alpha_2) \cdot \left(\frac{Y+1}{2} \cdot \frac{\left(Res(M_{c,p})\right)^2}{\left(Res(M_{c,p}) \cdot \sin(\alpha_2)\right)^2} - 1 \right) - \cot(\delta_2); \delta_2; 0 \text{ deg}; 90 \text{ deg} \right) = 13.6468 \text{ deg}$$

$$M_{s2} := Res(M_{c,p}) \cdot \sin(\alpha_2) = 1.3587$$

Figure 5.2. Screenshot of analytical solution procedure / 2

$$Z_{c,d} := \frac{Dir \cdot Z}{Res(Dir)} \cdot Dir = \begin{bmatrix} 0.1702 \\ 0.3351 \\ 0.1702 \end{bmatrix} \quad Z_{c,p} := Z - Z_{c,d} = \begin{bmatrix} -0.1702 \\ -0.3351 \\ 0.8298 \end{bmatrix}$$

Defines the unit vector of decomposed Mach number in characteristic plane, occurred due to theta 1

$$Dir_{Ms1} := \frac{Z_{c,p}}{Res(Z_{c,p})} = \begin{bmatrix} -0.1869 \\ -0.3678 \\ 0.9109 \end{bmatrix}$$

$$\alpha_1 := \text{solve} \left(\frac{|Z_{c,p} \cdot M_{c,p}|}{Res(M_{c,p}) \cdot Res(Z_{c,p})} - \cos(\alpha_1); \alpha_1; 0; \frac{\pi}{2} \right) = 50.9186 \text{ deg}$$

$$\delta_1 := \text{solve} \left(\tan(\alpha_1) \cdot \left(\frac{Y+1}{2} \cdot \frac{(Res(M_{c,p}))^2}{(Res(M_{c,p}) \cdot \sin(\alpha_1))^2 - 1} - 1 \right) - \cot(\delta_1); \delta_1; 0 \text{ deg}; 90 \text{ deg} \right) = 13.6469 \text{ deg}$$

$$M_{s1} := Res(M_{c,p}) \cdot \sin(\alpha_1) = 1.3587$$

$$\eta := \text{solve} \left(\frac{Z_{c,p} \cdot X_{c,p}}{Res(X_{c,p}) \cdot Res(Z_{c,p})} - \cos(\alpha); \alpha; 0; \frac{\pi}{2} \right) = 101.8372 \text{ deg}$$

Figure 5.3. Screenshot of analytical solution procedure / 3

Shock polar determination for incident shock

$$\mu_0 := \arcsin\left(\frac{1}{\text{Res}(M_{c,p})}\right) = 34.841 \text{ deg} \quad m := 100$$

$$\beta_0 := \left[\mu_0; \frac{\frac{\pi}{2} - \mu_0}{m} + \mu_0 \cdot \frac{\pi}{2} \right] \quad n := \text{length}(\beta_0) = 100 \quad \boxed{\text{interval of shock wave angles}}$$

$$\text{for } k \in [1..n] \\ \theta_0_k := \text{solve} \left\{ \tan(a) - 2 \cdot \cot\left(\beta_0_k\right) \cdot \frac{\left(\text{Res}(M_{c,p}) \cdot \sin\left(\beta_0_k\right)\right)^2 - 1}{2 + \text{Res}(M_{c,p})^2 \cdot \left(Y + \cos\left(2 \cdot \beta_0_k\right)\right)}; a; -0.01; \frac{\pi}{2} \right\} \quad \boxed{\text{flow deflection angles w.r.t. shock angles}}$$

$$\max(\theta_0) = 18.1297 \text{ deg}$$

Determines the maximum flow deflection angle with an oblique shock wave. This value limits the wedge angles, wedge angles can not be greater than this value.

$$\text{for } k \in [1..n] \\ \zeta_0_k := 1 + \frac{2 \cdot Y}{Y + 1} \cdot \left(\left(\text{Res}(M_{c,p}) \cdot \sin\left(\beta_0_k\right) \right)^2 - 1 \right) \quad \boxed{\text{Pressure ratio w.r.t. shock angle.}}$$

$$R_1 := \text{augment}\left(\theta_0 \cdot \frac{180}{\pi}; \zeta_0\right) \quad T_1 := \text{augment}\left(\theta_0 \cdot \frac{180}{\pi}; \beta_0 \cdot \frac{180}{\pi}\right) \quad R_2 := \text{augment}\left((- \theta_0) \cdot \frac{180}{\pi}; \zeta_0\right)$$

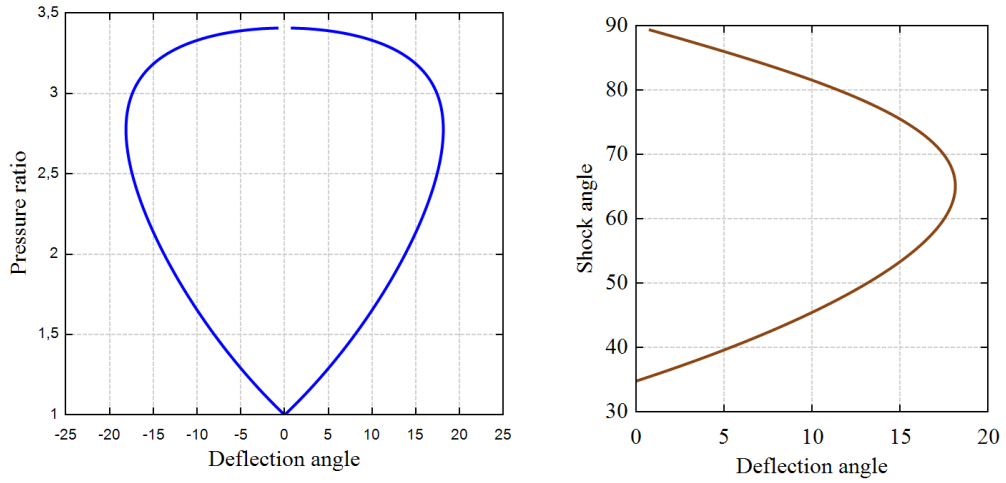


Figure 5.4. Screenshot of analytical solution procedure / 4

Shock polar determination for first reflected shock

$$\beta_{01} := \text{solve} \left[\tan(\alpha) \cdot \left(\frac{\gamma+1}{2} \cdot \frac{\text{Res}(M_{c,p})^2}{\left(\text{Res}(M_{c,p}) \cdot \sin(\alpha) \right)^2 - 1} - 1 \right) - \cot(\delta_1); \alpha; \mu_0 \cdot 1.01; 90 \text{ deg} \right] = \begin{bmatrix} 50.9184 \\ 77.4721 \end{bmatrix} \text{ deg}$$

$$\beta_{01} := \min(\beta_{01}) = 50.9184 \text{ deg} \quad \zeta_{01} := 1 + \frac{2 \cdot \gamma}{\gamma+1} \cdot \left(\left(\text{Res}(M_{c,p}) \cdot \sin(\beta_{01}) \right)^2 - 1 \right) = 1.987198$$

$$M_1 := \text{solve} \left[M_1^2 \cdot \left(\sin(\beta_{01} - \delta_1) \right)^2 - \frac{(\gamma-1) \cdot \text{Res}(M_{c,p})^2 \cdot \left(\sin(\beta_{01}) \right)^2 + 2}{2 \cdot \gamma \cdot \text{Res}(M_{c,p})^2 \cdot \left(\sin(\beta_{01}) \right)^2 - (\gamma-1)}; M_1; 0; \text{Res}(M_{c,p}) \right] = 1.2513$$

$$\mu_1 := \arcsin \left(\frac{1}{M_1} \right) = 53.0535 \text{ deg} \quad \beta_{1,1} := \left[\mu_1; \frac{\frac{\pi}{2} - \mu_1}{m} + \mu_1 \cdot \frac{\pi}{2} \right] \quad n := \text{length}(\beta_{1,1}) = 101$$

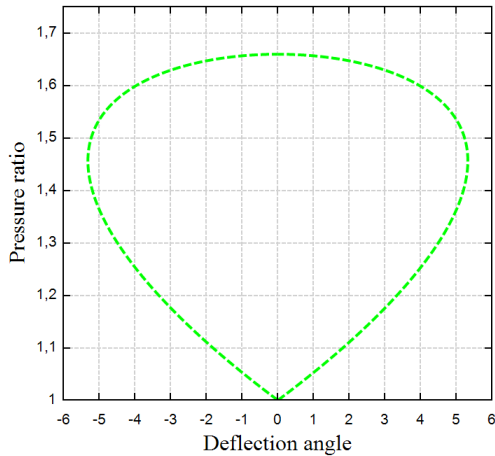
for $k \in [1..n]$

$$\theta_{1,1,k} := \text{solve} \left[\tan(\alpha) - 2 \cdot \cot(\beta_{1,1,k}) \cdot \frac{\left(M_1 \cdot \sin(\beta_{1,1,k}) \right)^2 - 1}{2 + M_1^2 \cdot \left(\gamma + \cos(2 \cdot \beta_{1,1,k}) \right)}; \alpha; -0.01; \frac{\pi}{2} \cdot 1.01 \right]$$

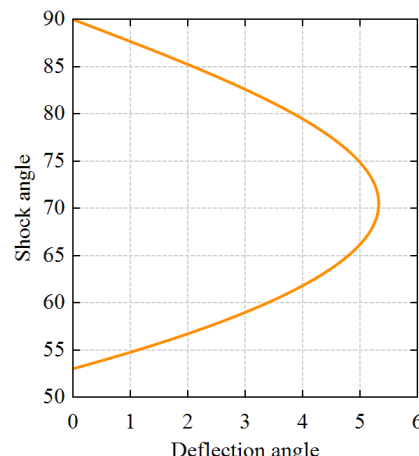
for $k \in [1..n]$

$$\zeta_{1,k} := 1 + \frac{2 \cdot \gamma}{\gamma+1} \cdot \left(\left(M_1 \cdot \sin(\beta_{1,1,k}) \right)^2 - 1 \right)$$

$$R_3 := \text{augment} \left(\theta_{1,1} \cdot \frac{180}{\pi}; \zeta_{1,k} \right) \quad R_4 := \text{augment} \left((-\theta_{1,1}) \cdot \frac{180}{\pi}; \zeta_{1,k} \right) \quad T_{1,1} := \text{augment} \left(\theta_{1,1} \cdot \frac{180}{\pi}; \beta_{1,1} \cdot \frac{180}{\pi} \right)$$



$$\begin{cases} R_3 \\ R_4 \end{cases}$$

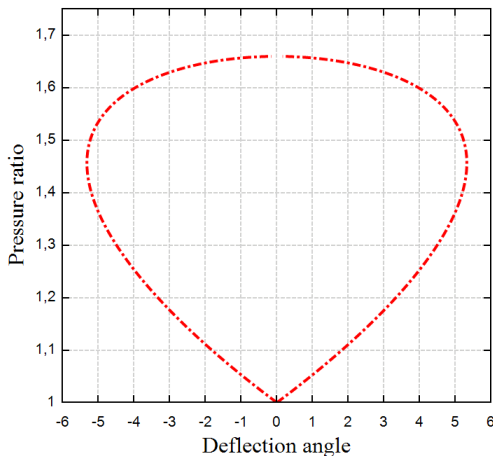


$$T_{1,1}$$

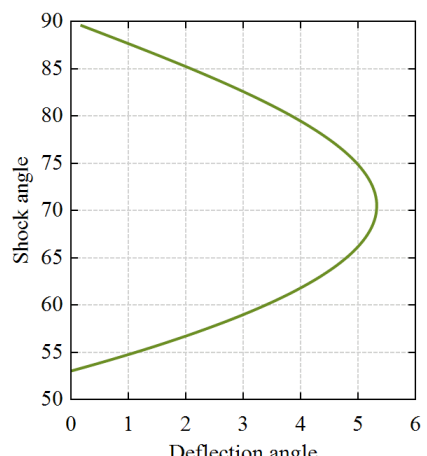
Figure 5.5. Screenshot of analytical solution procedure / 5

Shock polar determination for second reflected shock

$$\begin{aligned}\beta_{02} &:= \text{solve} \left(\tan(a) \cdot \left(\frac{\gamma+1}{2} \cdot \frac{\text{Res}(M_{c,p})^2}{(\text{Res}(M_{c,p}) \cdot \sin(a))^2 - 1} - 1 \right) - \cot(\delta_2); a; \mu_0 \cdot 1.01; 90 \text{ deg} \right) = \begin{bmatrix} 50.9184 \\ 77.4721 \end{bmatrix} \text{ deg} \\ \beta_{02} &:= \min(\beta_{02}) = 50.9184 \text{ deg} \quad \zeta_{02} := 1 + \frac{2 \cdot \gamma}{\gamma+1} \cdot \left((\text{Res}(M_{c,p}) \cdot \sin(\beta_{02}))^2 - 1 \right) = 1.9872 \\ M_2 &:= \text{solve} \left(M_2^2 \cdot (\sin(\beta_{02} - \delta_2))^2 - \frac{(\gamma-1) \cdot \text{Res}(M_{c,p})^2 \cdot (\sin(\beta_{02}))^2 + 2}{2 \cdot \gamma \cdot \text{Res}(M_{c,p})^2 \cdot (\sin(\beta_{02}))^2 - (\gamma-1)}; M_2; 0; \text{Res}(M_{c,p}) \right) = 1.2513 \\ \mu_2 &:= \text{asin} \left(\frac{1}{M_2} \right) = 53.0535 \text{ deg} \quad \beta_{2,2} := \left[\mu_2; \frac{\pi}{2} - \mu_2 + \mu_2 \cdot \frac{\pi}{2} \right] \quad n := \text{length}(\beta_{2,2}) = 100 \\ \text{for } k &\in [1..n] \\ \theta_{2,2,k} &:= \text{solve} \left(\tan(a) - 2 \cdot \cot(\beta_{2,2,k}) \cdot \frac{(M_2 \cdot \sin(\beta_{2,2,k}))^2 - 1}{2 + M_2^2 \cdot (\gamma + \cos(2 \cdot \beta_{2,2,k}))}; a; -0.01; \frac{\pi}{2} \cdot 1.01 \right) \\ \text{for } k &\in [1..n] \\ \zeta_{2,k} &:= 1 + \frac{2 \cdot \gamma}{\gamma+1} \cdot \left((M_2 \cdot \sin(\beta_{2,2,k}))^2 - 1 \right) \\ R_5 &:= \text{augment} \left(\theta_{2,2} \cdot \frac{180}{\pi}; \zeta_{2,k} \right) \quad R_6 := \text{augment} \left((-\theta_{2,2}) \cdot \frac{180}{\pi}; \zeta_{2,k} \right) \quad T_{1,2} := \text{augment} \left(\theta_{2,2} \cdot \frac{180}{\pi}; \beta_{2,2} \cdot \frac{180}{\pi} \right)\end{aligned}$$



$$\begin{cases} R_5 \\ R_6 \end{cases}$$

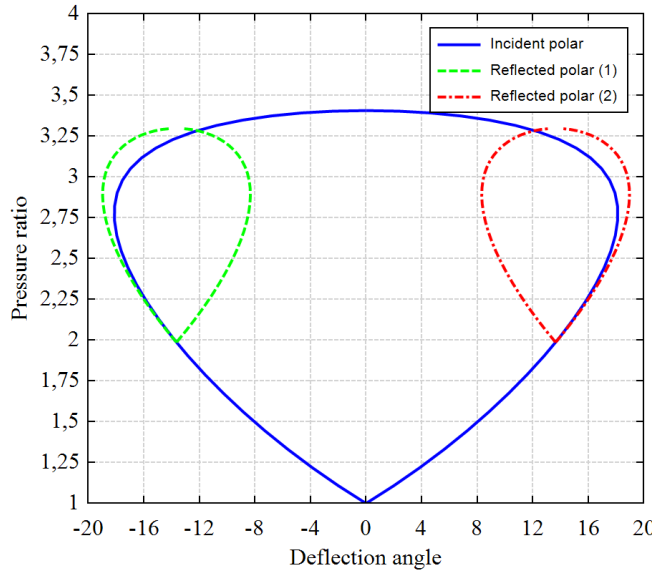


$$T_{1,2}$$

Figure 5.6. Screenshot of analytical solution procedure / 6

$$R_3 := \text{augment} \left(\left(\theta_{1,1} - \delta_1 \right) \cdot \frac{180}{\pi}; \zeta_1 \cdot \zeta_{01} \right) \quad R_4 := \text{augment} \left(\left(-\theta_{1,1} - \delta_1 \right) \cdot \frac{180}{\pi}; \zeta_1 \cdot \zeta_{01} \right)$$

$$R_5 := \text{augment} \left(\left(\theta_{2,2} + \delta_2 \right) \cdot \frac{180}{\pi}; \zeta_2 \cdot \zeta_{02} \right) \quad R_6 := \text{augment} \left(\left(-\theta_{2,2} + \delta_2 \right) \cdot \frac{180}{\pi}; \zeta_2 \cdot \zeta_{02} \right)$$



$$\begin{cases} R_1 \\ R_2 \\ R_3, \\ R_4, \\ R_5, \\ R_6, \end{cases}$$

Calculation of Mach number of stem and related angles

□

```

 $M_s := \text{if } M_{s1} < M_{s2} = 1.3587 \quad n := 70$ 
 $\quad M_{s2}$ 
 $\text{else} \quad m := 70$ 
 $\quad M_{s1}$ 
 $\Delta := 0.01 \quad M_m := M_s$ 

```

Figure 5.7. Screenshot of analytical solution procedure / 7

```

for k ∈ [1..m]
  M_m := (M_m + Δ · k)
  for i ∈ [1..(n+1)]
    M_i := M_s1 +  $\frac{i-1}{n} \cdot (M_m - M_{s1})$ 
    μ_i :=  $\sqrt{\frac{(\gamma-1) \cdot (M_i)^2 + 2}{2 \cdot \gamma \cdot (M_i)^2 - (\gamma-1)}}$ 
    K_i :=  $\frac{2}{2 \cdot \mu_i + 1 + (M_i)^2} \cdot \left(1 + \frac{2}{\gamma+1} \cdot \frac{1 - (\mu_i)^2}{\mu_i}\right)^{-1}$ 
    a_i :=  $\frac{2 \cdot M_i}{(M_i)^2 - 1} \cdot K_i$ 
    F_1 := exp  $\left(- \sum_{i=1}^{n+1} a_i \cdot (M_2 - M_1)\right)$ 
  for i ∈ [1..(n+1)]
    M_i := M_s2 +  $\frac{i-1}{n} \cdot (M_m - M_{s2})$ 
    μ_i :=  $\sqrt{\frac{(\gamma-1) \cdot (M_i)^2 + 2}{2 \cdot \gamma \cdot (M_i)^2 - (\gamma-1)}}$ 
    K_i :=  $\frac{2}{2 \cdot \mu_i + 1 + (M_i)^2} \cdot \left(1 + \frac{2}{\gamma+1} \cdot \frac{1 - (\mu_i)^2}{\mu_i}\right)^{-1}$ 
    a_i :=  $\frac{2 \cdot M_i}{(M_i)^2 - 1} \cdot K_i$ 
    F_2 := exp  $\left(- \sum_{i=1}^{n+1} a_i \cdot (M_2 - M_1)\right)$ 
    θ_w1_k := min solve  $\left[ \frac{M_m}{M_{s1}} \cdot \sqrt{1 - \left(\frac{M_{s1}}{M_m}\right)^2} \cdot \sqrt{1 - (F_1)^2} - \tan(b); b; 0.1 \text{ deg}; \frac{\pi}{2} \right]$ 
    θ_w2_k := min solve  $\left[ \frac{M_m}{M_{s2}} \cdot \sqrt{1 - \left(\frac{M_{s2}}{M_m}\right)^2} \cdot \sqrt{1 - (F_2)^2} - \tan(\pi - \eta - c); c; 0.1 \text{ deg}; \frac{\pi}{2} \right]$ 
    if θ_w2_k - θ_w1_k < 0.1 deg
      break
    else
      if θ_w2_k - θ_w1_k < 0.5 deg
        Δ := 0.00001
      else
        if θ_w2_k - θ_w1_k < 2 deg
          Δ := 0.0001
        else
          if θ_w2_k - θ_w1_k < 5 deg
            Δ := 0.001
          else
            continue

```

Figure 5.8. Screenshot of analytical solution procedure / 8

$$\begin{aligned}
M_m &= 1.8407 \quad F_1 = 0.0891 \quad F_2 = 0.0891 \quad \theta_{w1} = 39.085 \text{ deg} \quad \pi - \eta - \theta_{w1} = 39.0779 \text{ deg} \\
\chi_1 &:= \text{solve} \left[F_1 \cdot \sqrt{\frac{1 - \left(\frac{M_{s1}}{M_m}\right)^2}{1 - F_1^2}} - \tan(a); a; -\frac{\pi}{4}; \frac{\pi}{4} \right] = 3.4531 \text{ deg} \quad k = 36 \\
\chi_2 &:= \text{solve} \left[F_2 \cdot \sqrt{\frac{1 - \left(\frac{M_{s2}}{M_m}\right)^2}{1 - F_2^2}} - \tan(b); b; 0; \frac{\pi}{2} \right] = 3.4531 \text{ deg} \\
\zeta_m &:= \frac{2 \cdot \gamma \cdot M_m^2 - (\gamma - 1)}{\gamma + 1} = 3.7862 \quad OY := 1 \text{ mm}
\end{aligned}$$

Rotation step for slip lines at characteristic plane

□

$$\begin{aligned}
C_1 &:= (-Dir) \cdot (-Dir)^T \cdot Dir_{Ms2} \quad C_2 := Dir_{Ms2} - C_1 \quad C_3 := -Dir \times Dir_{Ms2} \\
Dir_{S2} &:= C_1 + C_2 \cdot \cos \left(\frac{\pi}{2} - \left(\pi - \eta - \theta_{w1} \right) - \chi_2 \right) + C_3 \cdot \sin \left(\frac{\pi}{2} - \left(\pi - \eta - \theta_{w1} \right) - \chi_2 \right) = \begin{bmatrix} 0.6158 \\ -0.5824 \\ 0.5307 \end{bmatrix} \\
Dir_{S1} &:= C_1 + C_2 \cdot \cos \left(\frac{\pi}{2} - \left(\pi - \eta - \theta_{w1} \right) + \chi_1 \right) + C_3 \cdot \sin \left(\frac{\pi}{2} - \left(\pi - \eta - \theta_{w1} \right) + \chi_1 \right) = \begin{bmatrix} 0.5306 \\ -0.5824 \\ 0.6159 \end{bmatrix}
\end{aligned}$$

Solution step for slip line end points on characteristic plane and outlet plane

□

$$\begin{aligned}
Given_{S2} &:= \begin{bmatrix} (Dir_1 \cdot A + Dir_3 \cdot B) \cdot Dir_1 + Dir_{S2} & -A \\ (Dir_1 \cdot A + Dir_3 \cdot B) \cdot Dir_3 + Dir_{S2} & -B \end{bmatrix} \quad var_1 := \begin{bmatrix} A \\ B \end{bmatrix} \quad guess := \begin{bmatrix} 0 \\ 0 \end{bmatrix} \\
S_2 &:= \begin{bmatrix} \text{roots}(Given_{S2}; var_1; guess)_1 \\ 0 \\ \text{roots}(Given_{S2}; var_1; guess)_2 \end{bmatrix} = \begin{bmatrix} 0.9116 \\ 0 \\ 0.8265 \end{bmatrix} \\
Given_{S1} &:= \begin{bmatrix} (Dir_1 \cdot C + Dir_3 \cdot D) \cdot Dir_1 + Dir_{S1} & -C \\ (Dir_1 \cdot C + Dir_3 \cdot D) \cdot Dir_3 + Dir_{S1} & -D \end{bmatrix} \quad var_2 := \begin{bmatrix} C \\ D \end{bmatrix} \quad guess_1 := \begin{bmatrix} -1 \\ -1 \end{bmatrix} \\
S_1 &:= \begin{bmatrix} \text{roots}(Given_{S1}; var_2; guess_1)_1 \\ 0 \\ \text{roots}(Given_{S1}; var_2; guess_1)_2 \end{bmatrix} = \begin{bmatrix} 0.8265 \\ 0 \\ 0.9117 \end{bmatrix} \\
m_{S,2} &:= \frac{S_2}{S_2}_3 = 0.9067 \quad m_{S,1} := \frac{S_1}{S_1}_3 = 1.1032
\end{aligned}$$

Figure 5.9. Screenshot of analytical solution procedure / 9

Demonstration of velocity traces

□—
□—

$$X_{\infty} := 5 \text{ mm}$$

$$Z_{\infty} := 5 \text{ mm}$$

$$X_1 := \frac{X_{\infty}}{X_1} = 5 \text{ mm}$$

$$Z_1 := \frac{Z_{\infty}}{Z_3} = 5 \text{ mm}$$

$$X_2 := \frac{OY - X_2 \cdot X_1}{X_{wedge_2}} = 1.0139 \text{ mm}$$

$$Z_2 := \frac{OY - Z_2 \cdot Z_1}{Z_{wedge_2}} = 1.0139 \text{ mm}$$

$$X_3 := \frac{OY - X_2 \cdot X_1}{X_{char_2}} = 1.1216 \text{ mm}$$

$$Z_3 := \frac{OY - Z_2 \cdot Z_1}{Z_{char_2}} = 1.1216 \text{ mm}$$

$$O_1 := \begin{bmatrix} \frac{OY}{Dir_{wedge_2}} \cdot Dir_{wedge_1} & \frac{OY}{Dir_{wedge_2}} \cdot Dir_{wedge_3} \\ 1 & 3 \end{bmatrix} = [0.1673 \ 0.1673] \text{ mm}$$

$$O_{dir} := \begin{bmatrix} Dir_1 \cdot OY & Dir_3 \cdot OY \\ \frac{Dir_1}{Dir_2} \cdot OY & \frac{Dir_3}{Dir_2} \cdot OY \end{bmatrix} = [0.508 \ 0.508] \text{ mm}$$

$$O_x := \begin{bmatrix} (X \cdot X_1 + X_{wedge} \cdot X_2) & (X \cdot X_1 + X_{wedge} \cdot X_2) \\ 1 & 3 \end{bmatrix} = [5 \ 0.1673] \text{ mm}$$

$$O_z := \begin{bmatrix} (Z \cdot Z_1 + Z_{wedge} \cdot Z_2) & (Z \cdot Z_1 + Z_{wedge} \cdot Z_2) \\ 1 & 3 \end{bmatrix} = [0.1673 \ 5] \text{ mm}$$

$$O_{x1} := \begin{bmatrix} (X \cdot X_1 + X_{char} \cdot X_3) & (X \cdot X_1 + X_{char} \cdot X_3) \\ 1 & 3 \end{bmatrix} = [5 \ 0.508] \text{ mm}$$

$$O_{z1} := \begin{bmatrix} (Z \cdot Z_1 + Z_{char} \cdot Z_3) & (Z \cdot Z_1 + Z_{char} \cdot Z_3) \\ 1 & 3 \end{bmatrix} = [0.508 \ 5] \text{ mm}$$

$$Z_{wedge \cdot OY} := \begin{bmatrix} O_1 & O_1 \\ 1 & 2 \\ O_z & O_z \\ 1 & 2 \end{bmatrix} \quad X_{wedge \cdot OY} := \begin{bmatrix} O_1 & O_1 \\ 1 & 2 \\ O_x & O_x \\ 1 & 2 \end{bmatrix}$$

$$m_{s2.in} := \frac{O_{z1}^2 - O_{dir}^2}{O_{z1}^2 - O_{dir}^2} = -6.378 \cdot 10^{15}$$

$$m_{s1.in} := \frac{O_{x1}^2 - O_{dir}^2}{O_{x1}^2 - O_{dir}^2} = -1.5679 \cdot 10^{-16}$$

Figure 5.10. Screenshot of analytical solution procedure / 10

$$c_{S2.in} := \frac{O_{z1}}{2} - m_{S2.in} \cdot O_{z1} = 3.2401 \cdot 10^{15} \text{ mm} \quad c_{S1.in} := \frac{O_{x1}}{2} - m_{S1.in} \cdot O_{x1} = 0.508 \text{ mm}$$

$$X_{S2} := \frac{c_{S2.in}}{\left(m_{S.1} - m_{S2.in} \right)} = 0.508 \text{ mm} \quad X_{S1} := \frac{c_{S1.in}}{\left(m_{S.2} - m_{S1.in} \right)} = 0.5603 \text{ mm}$$

$$Z_{S2} := m_{S.1} \cdot X_{S2} = 0.5604 \text{ mm} \quad Z_{S1} := m_{S.2} \cdot X_{S1} = 0.508 \text{ mm}$$

$$P_1 := \begin{bmatrix} X_{S2} \\ Z_{S2} \end{bmatrix} \quad P_2 := \begin{bmatrix} X_{S1} \\ Z_{S1} \end{bmatrix}$$

$$O_{MS1} := \begin{bmatrix} O_1 & O_1 \\ P_1 & P_1 \\ P_2 & P_2 \\ 1 & 2 \end{bmatrix} = \begin{bmatrix} 0.1673 & 0.1673 \\ 0.5603 & 0.508 \end{bmatrix} \text{ mm}$$

$$S_{2.in} := \begin{bmatrix} P_2 & P_2 \\ 1 & 2 \\ O_{x1} & O_{x1} \\ 1 & 2 \end{bmatrix} = \begin{bmatrix} 0.5603 & 0.508 \\ 5 & 0.508 \end{bmatrix} \text{ mm}$$

$$O_{MS2} := \begin{bmatrix} O_1 & O_1 \\ P_1 & P_1 \\ P_2 & P_2 \\ 1 & 2 \end{bmatrix} = \begin{bmatrix} 0.1673 & 0.1673 \\ 0.508 & 0.5604 \end{bmatrix} \text{ mm}$$

$$S_{1.in} := \begin{bmatrix} P_1 & P_1 \\ 1 & 2 \\ O_{z1} & O_{z1} \\ 1 & 2 \end{bmatrix} = \begin{bmatrix} 0.508 & 0.5604 \\ 0.508 & 5 \end{bmatrix} \text{ mm}$$

$$O_{Mm} := \begin{bmatrix} P_1 & P_1 \\ P_2 & P_2 \\ 1 & 2 \end{bmatrix} = \begin{bmatrix} 0.508 & 0.5604 \\ 0.5603 & 0.508 \end{bmatrix} \text{ mm}$$

Results

Experimental

□

$$\begin{aligned} ER_{Mach} &:= importData ("D:\belgeler\egitim\ders-kitaplari-notlari\tez\analitik\cozumler\1\exp\mach.stem.txt"; 0; 0; 0; 0; 0; 0; 0; 0) + \frac{O_1}{1} \frac{1}{\text{mm}} \\ ER_{shock.x} &:= importData ("D:\belgeler\egitim\ders-kitaplari-notlari\tez\analitik\cozumler\1\exp\inc.left.txt"; 0; 0; 0; 0; 0; 0; 0; 0) + \frac{O_1}{1} \frac{1}{\text{mm}} \\ ER_{shock.z} &:= importData ("D:\belgeler\egitim\ders-kitaplari-notlari\tez\analitik\cozumler\1\exp\inc.right.txt"; 0; 0; 0; 0; 0; 0; 0; 0) + \frac{O_1}{1} \frac{1}{\text{mm}} \end{aligned}$$

Numerical

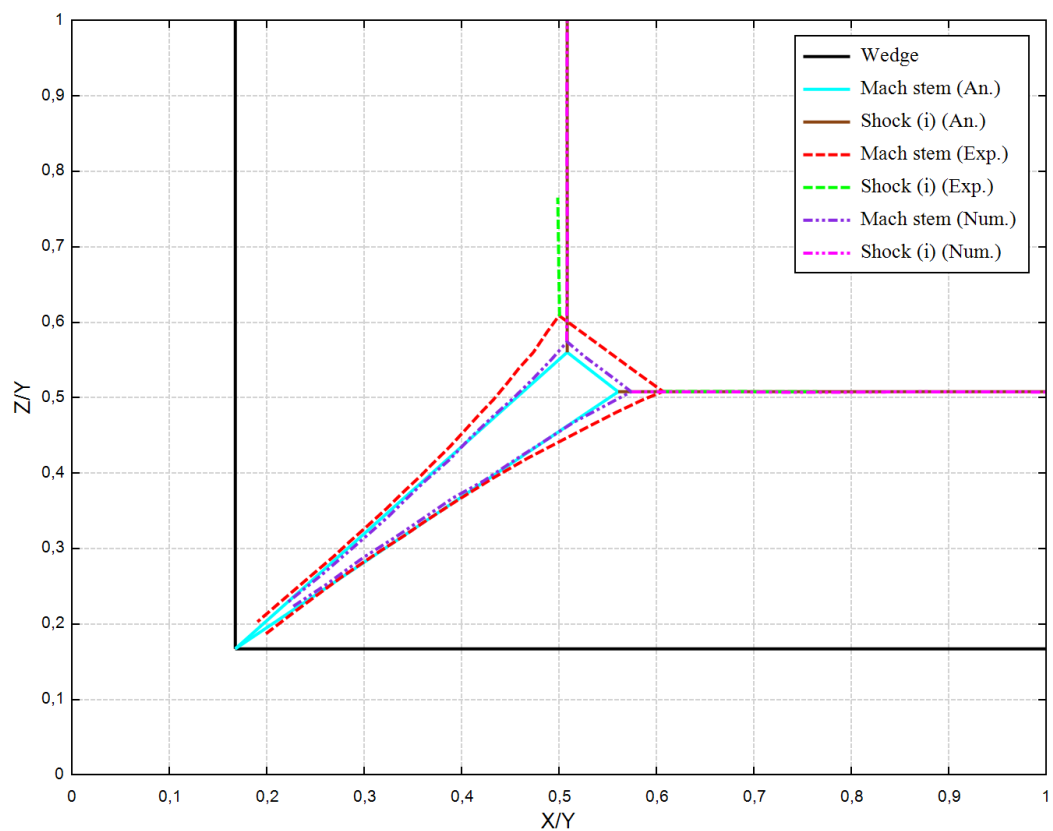
□

$$Num_{Mach} := \frac{importData ("D:\belgeler\egitim\ders-kitaplari-notlari\tez\analitik\cozumler\1\num\mach.stem.txt"; 0; 0; 0; 0; 0; 0; 0; 0)}{5}$$

$$Num_{shock.x} := \frac{importData ("D:\belgeler\egitim\ders-kitaplari-notlari\tez\analitik\cozumler\1\num\inc.left.txt"; 0; 0; 0; 0; 0; 0; 0; 0)}{5}$$

$$Num_{shock.z} := \frac{importData ("D:\belgeler\egitim\ders-kitaplari-notlari\tez\analitik\cozumler\1\num\inc.right.txt"; 0; 0; 0; 0; 0; 0; 0; 0)}{5}$$

Figure 5.11. Screenshot of analytical solution procedure / 11



$Z_{wedge, OY} \cdot 1000$
 $X_{wedge, OY} \cdot 1000$
 $O_{Ms1} \cdot 1000$
 $O_{Ms2} \cdot 1000$
 $O_{Mm} \cdot 1000$
 $S_{2,in} \cdot 1000$
 $S_{1,in} \cdot 1000$
 ER_{Mach}
 $ER_{shock,x}$
 $ER_{shock,z}$
 Num_{Mach}
 $Num_{shock,x}$
 $Num_{shock,z}$

Figure 5.12. Screenshot of analytical solution procedure / 12

B. Shock Polar Diagrams for Solutions

Shock polar curves are given from Figure 5.14 to Figure 5.25 for studied cases.

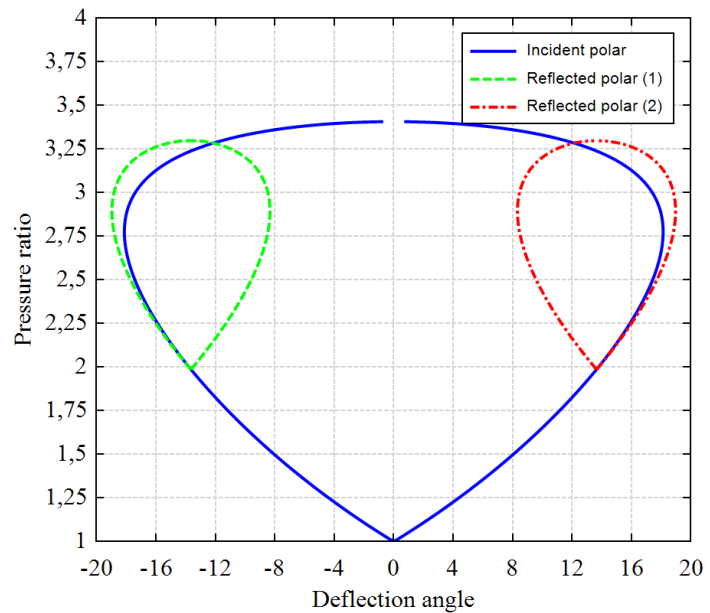


Figure 5.13. Shock polar curves for Case Ref. [17]

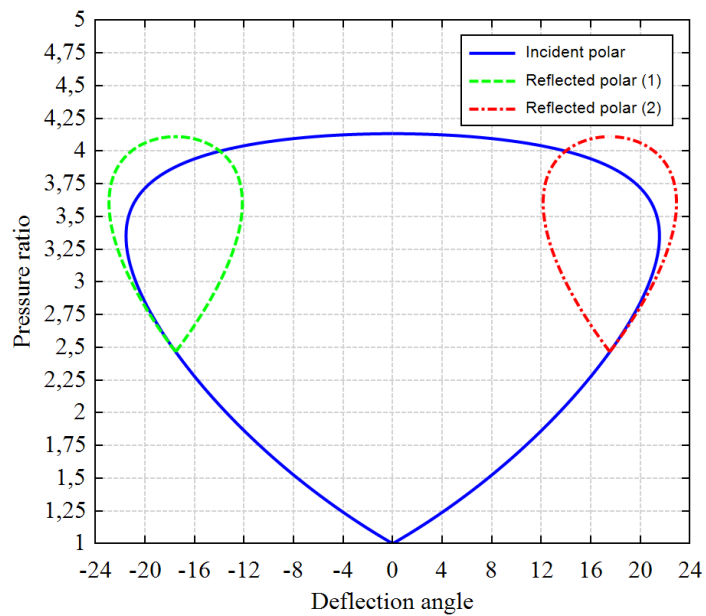


Figure 5.14. Shock polar curves for Case Ref. [14]

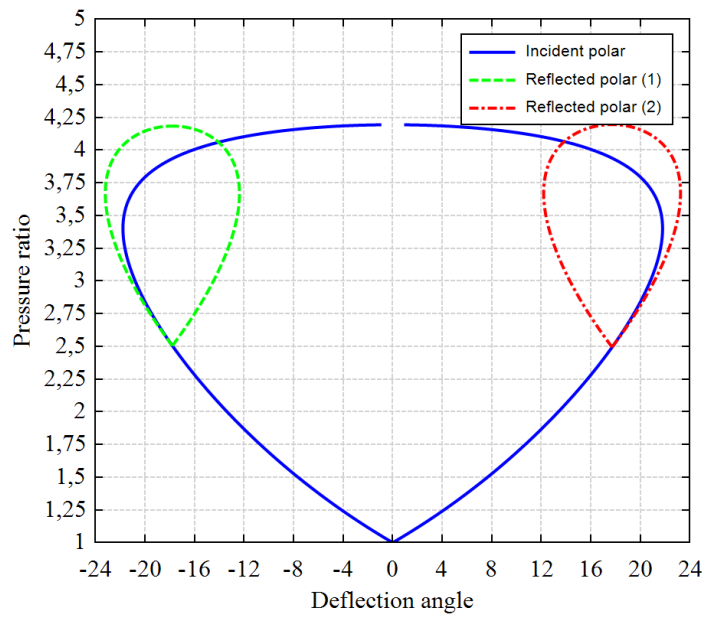


Figure 5.15. Shock polar curves for Case A

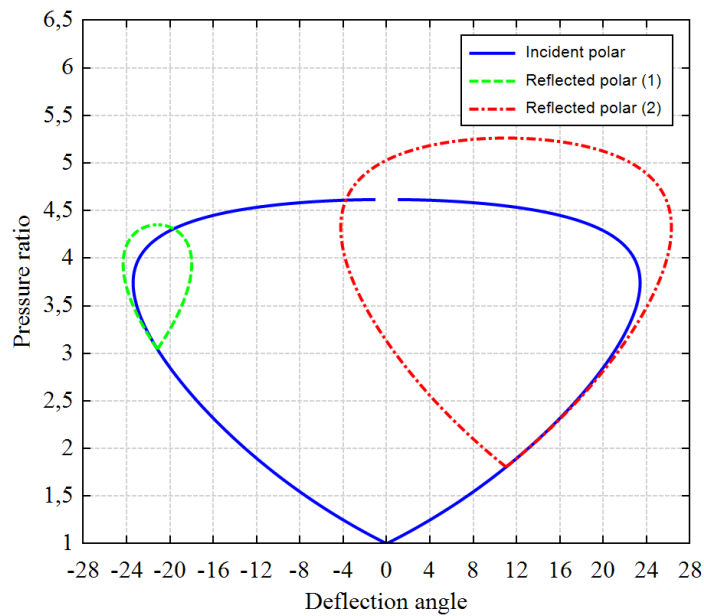


Figure 5.16. Shock polar curves for Case B

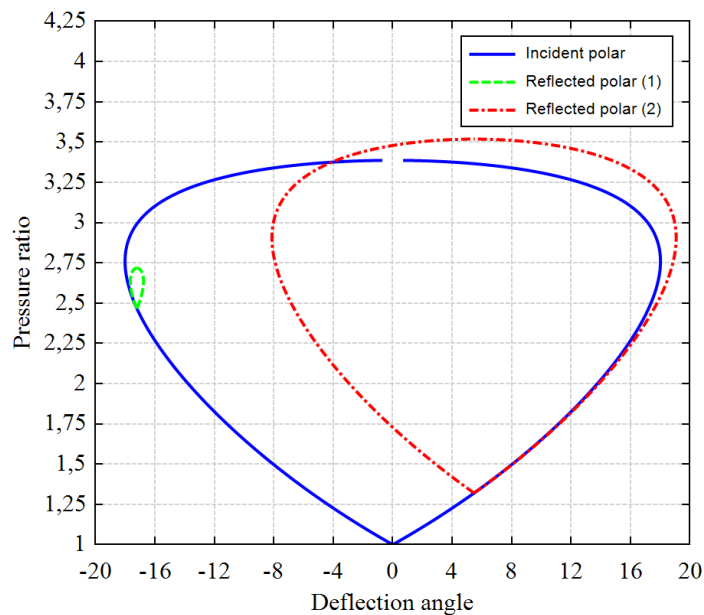


Figure 5.17. Shock polar curves for Case C

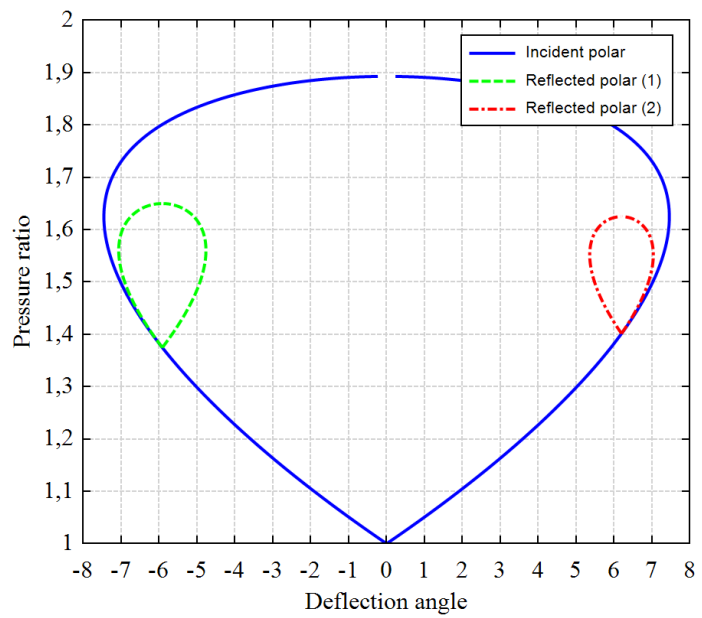


Figure 5.18. Shock polar curves for Case D

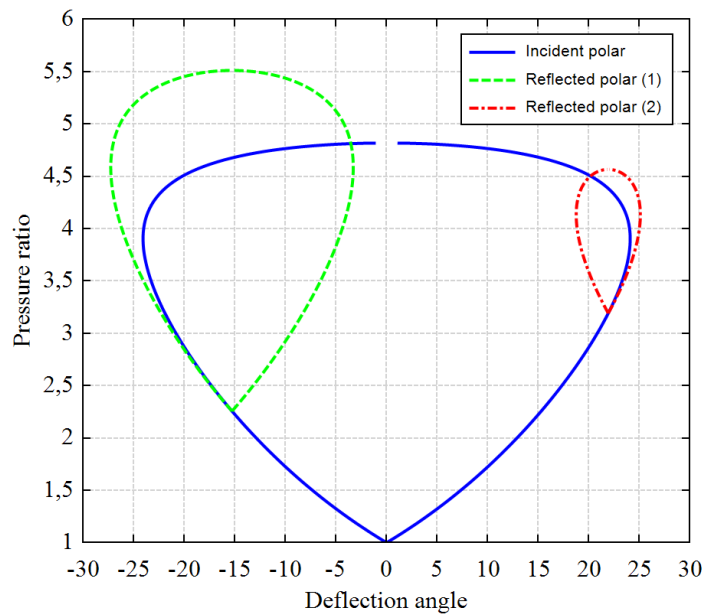


Figure 5.19. Shock polar curves for Case E

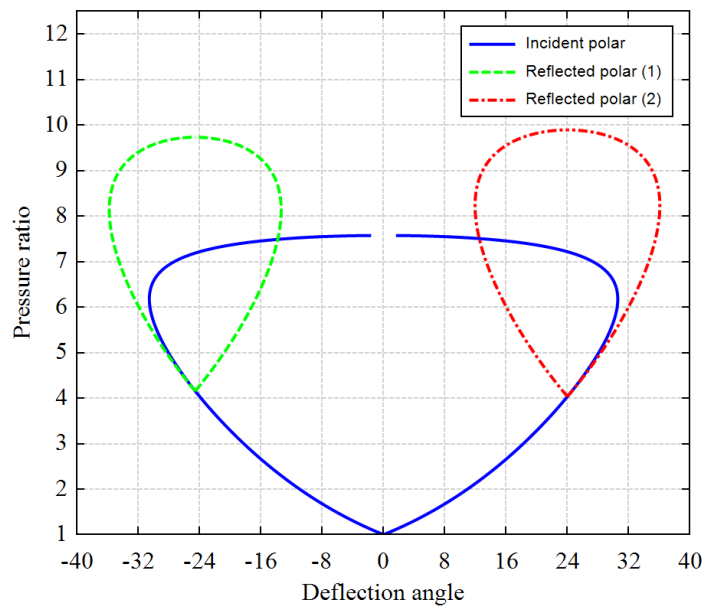


Figure 5.20. Shock polar curves for Case F

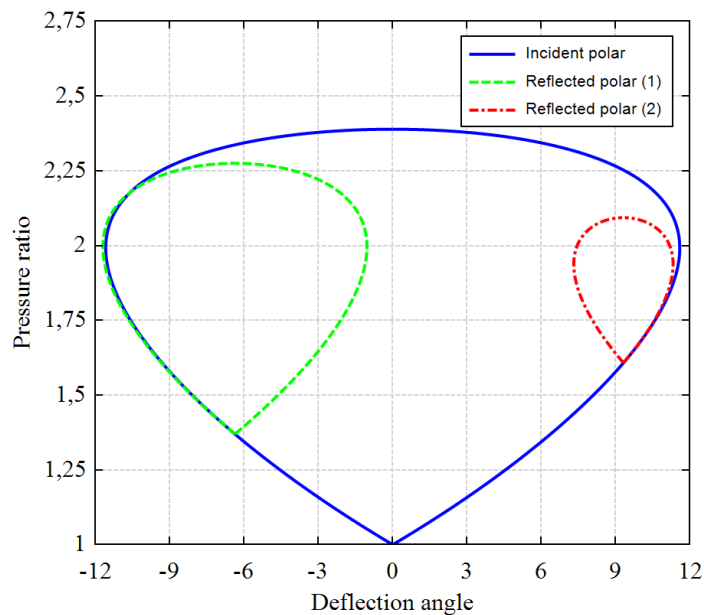


Figure 5.21. Shock polar curves for Case G

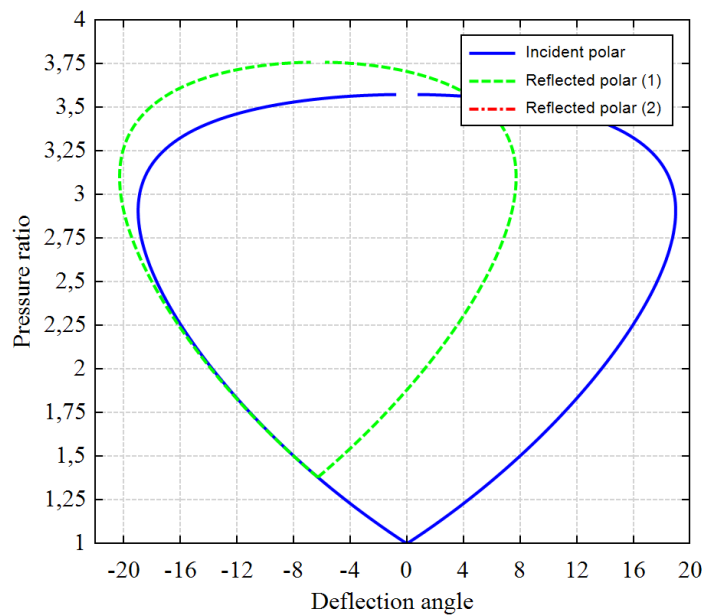


Figure 5.22. Shock polar curves for Case H

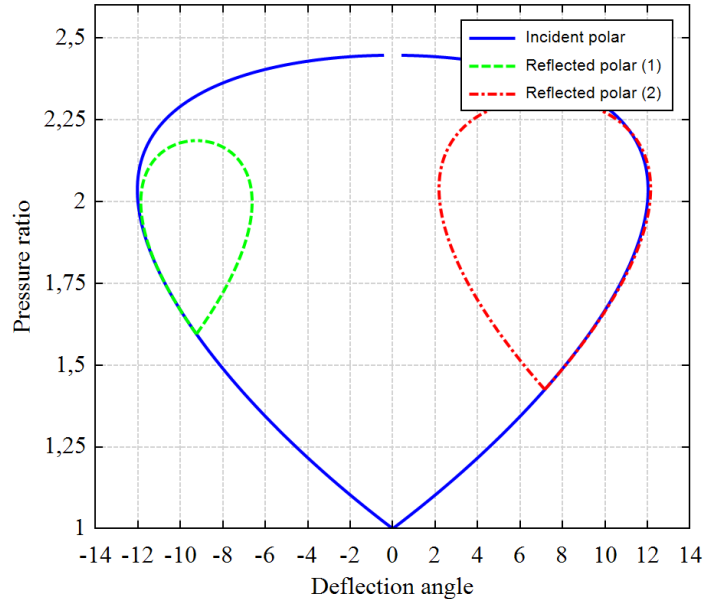


Figure 5.23. Shock polar curves for Case I

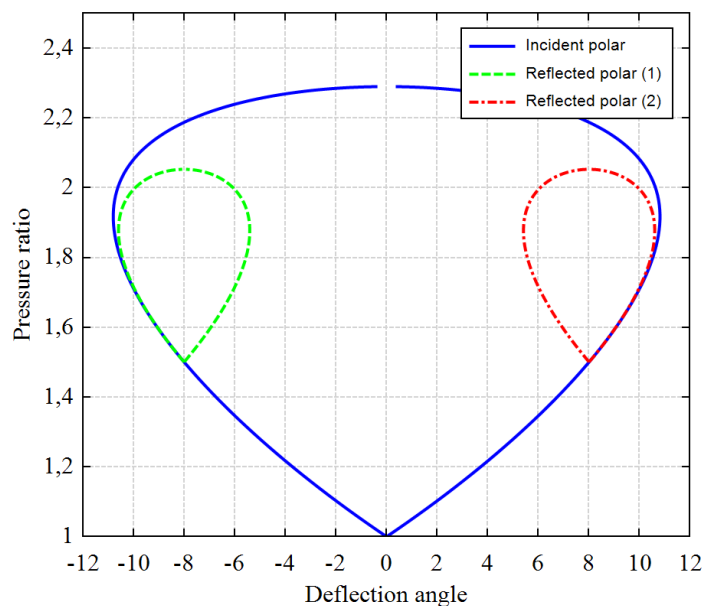


Figure 5.24. Shock polar curves for Case J

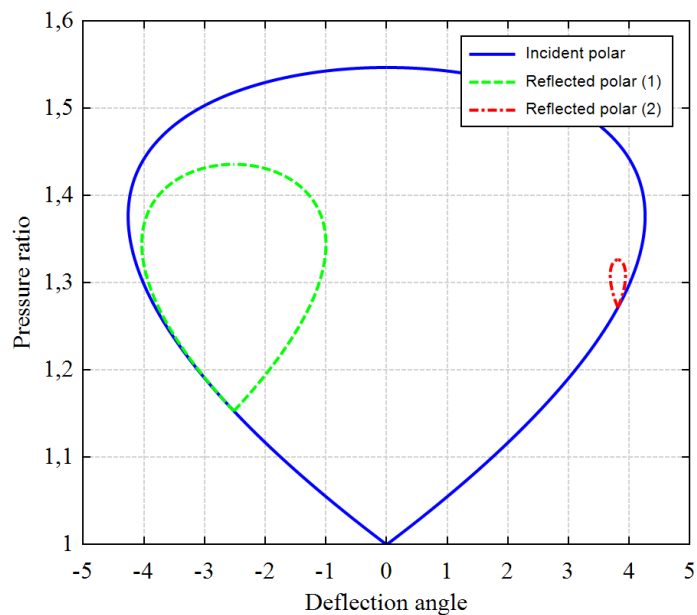


Figure 5.25. Shock polar curves for Case K

C. Pressure Ratios Along Calculation Lines

Pressure ratios along calculation lines are given from Figure 5.26 to Figure 5.38 for studied cases. Absolute pressure values are normalized with ambient pressure which is defined in Section 3.4.3.2 as 80 kPa . The abrupt change in pressure ratio indicates shock wave existence which is Mach stem in such cases. The selection of calculation lines can be seen in Figure 3.16. Pressure ratio across Mach stem is found by using the highest value in the proximity of abrupt decrease in pressure.

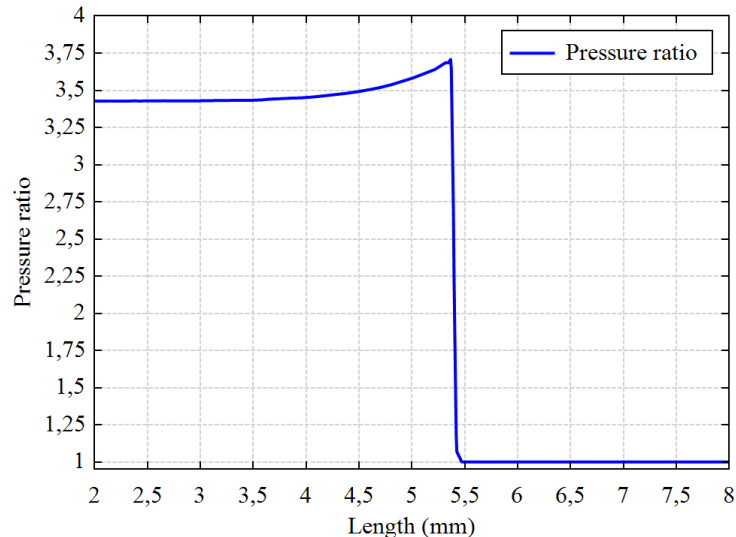


Figure 5.26. Pressure ratios for Case Ref. [17]

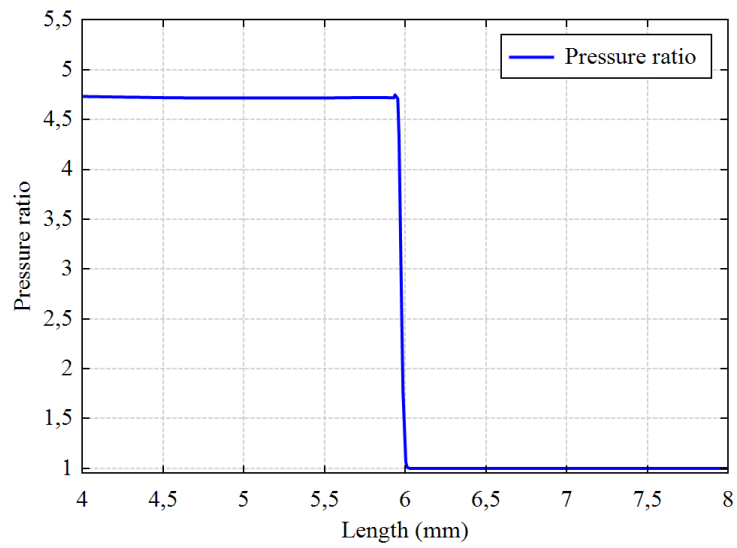


Figure 5.27. Pressure ratios for Case Ref. [14]

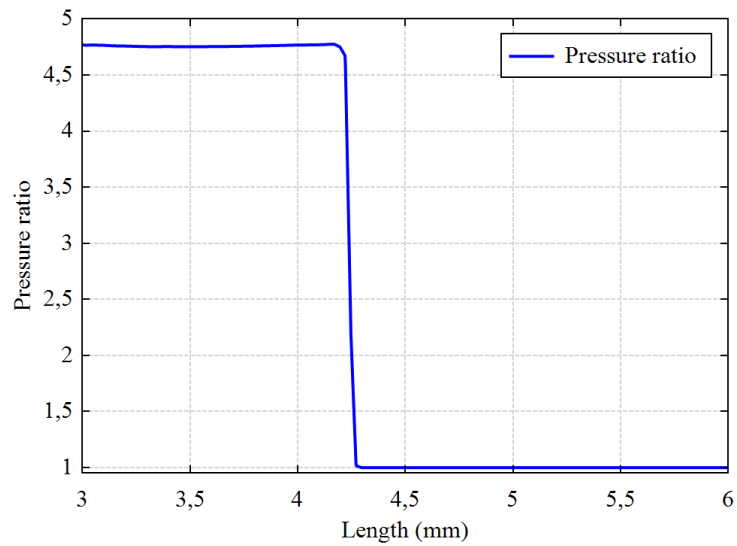


Figure 5.28. Pressure ratios for Case A

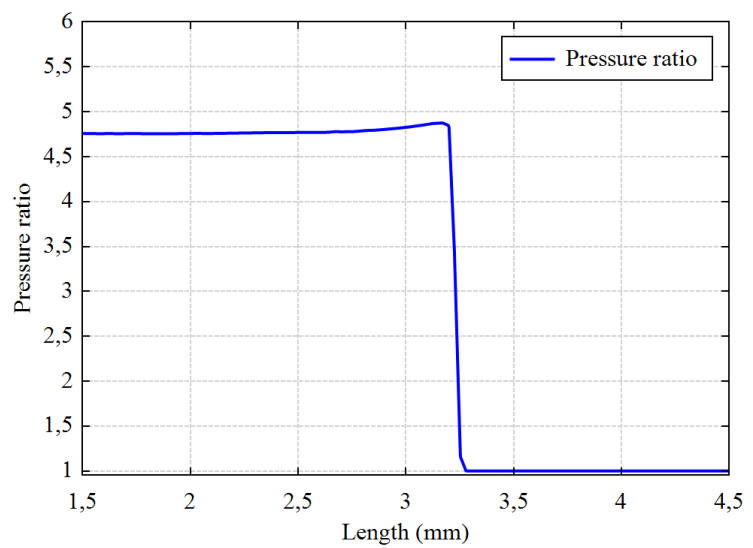


Figure 5.29. Pressure ratios for Case B

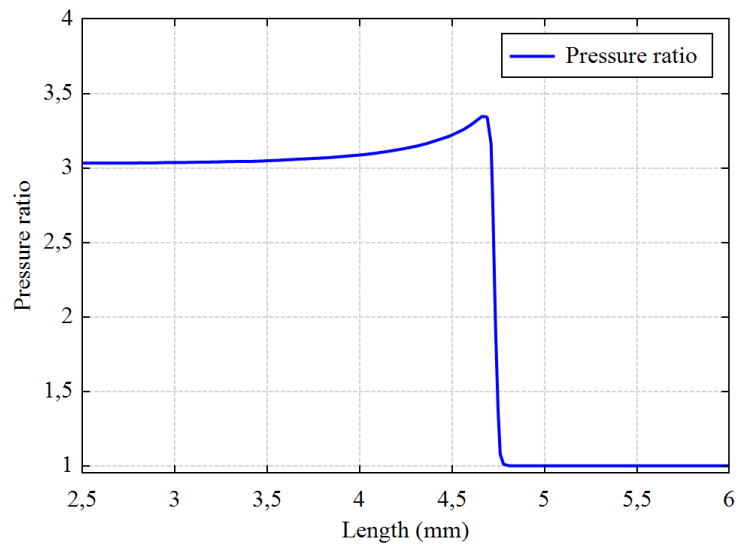


Figure 5.30. Pressure ratios for Case C

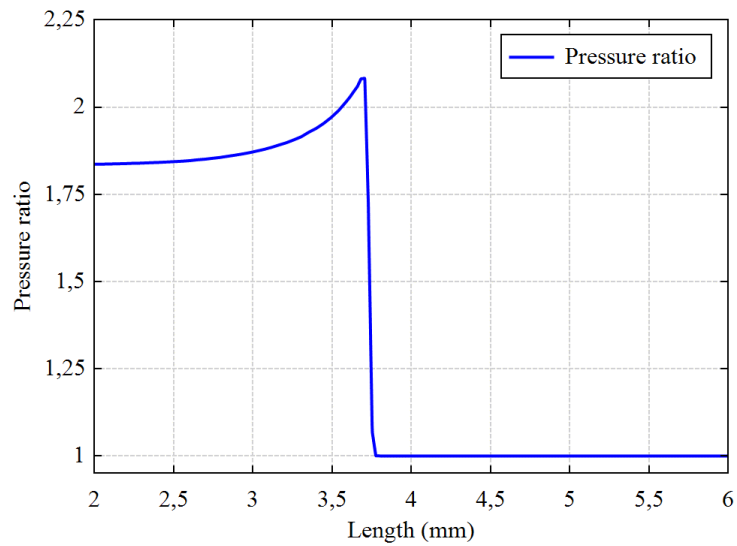


Figure 5.31. Pressure ratios for Case D

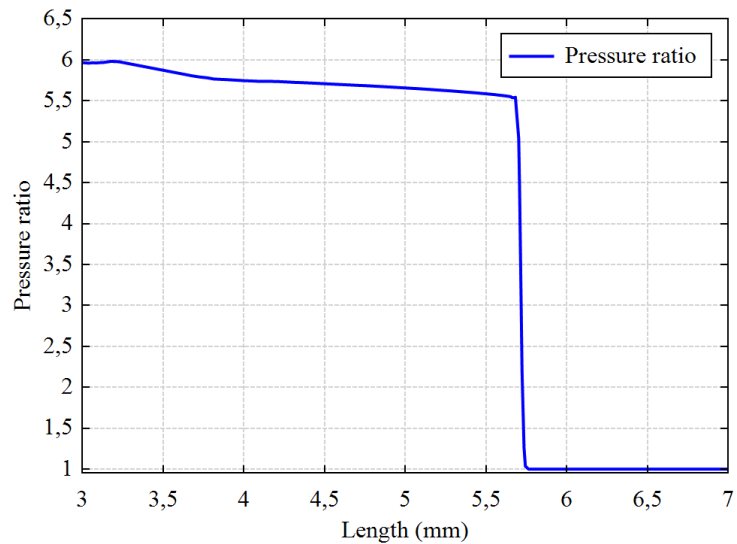


Figure 5.32. Pressure ratios for Case E

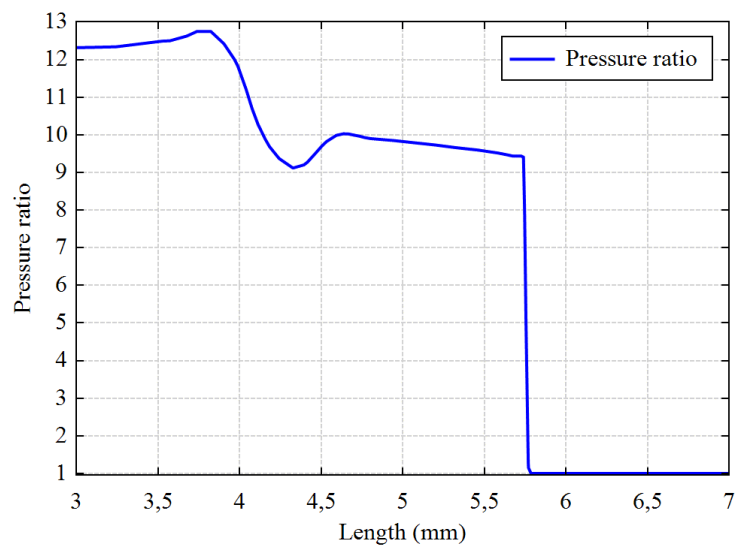


Figure 5.33. Pressure ratios for Case F

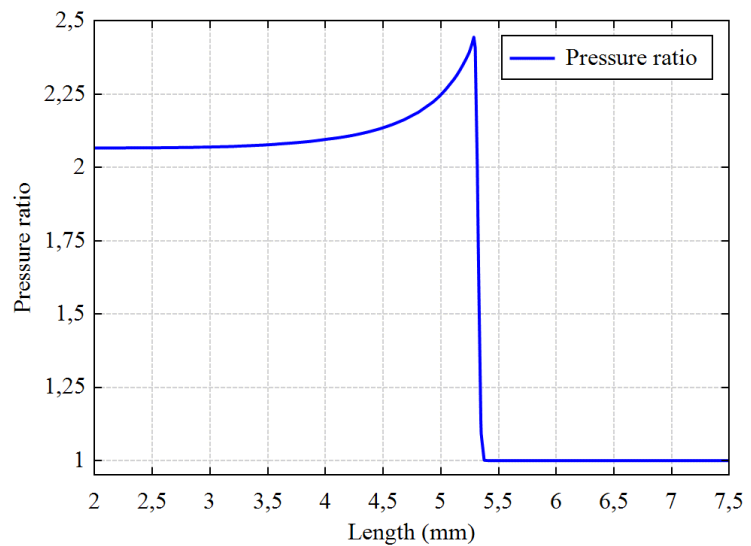


Figure 5.34. Pressure ratios for Case G

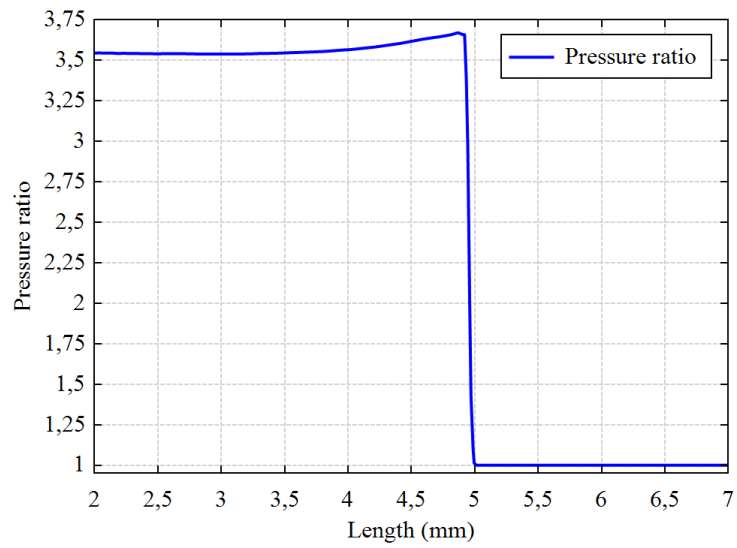


Figure 5.35. Pressure ratios for Case H

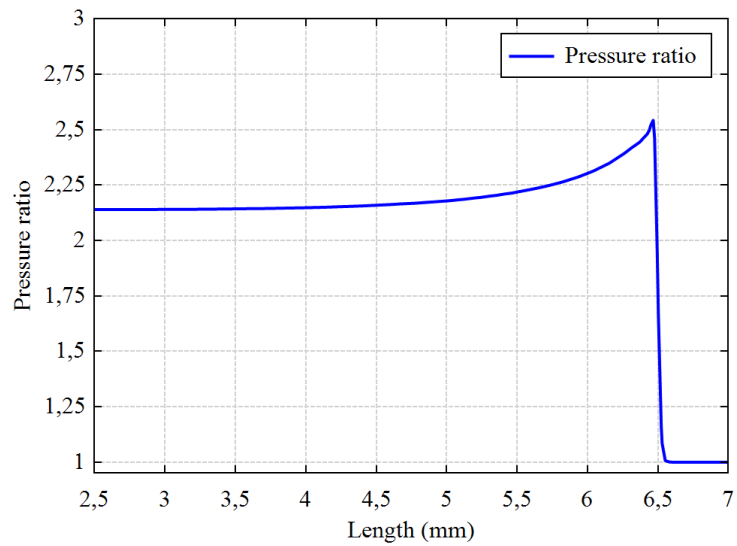


Figure 5.36. Pressure ratios for Case I

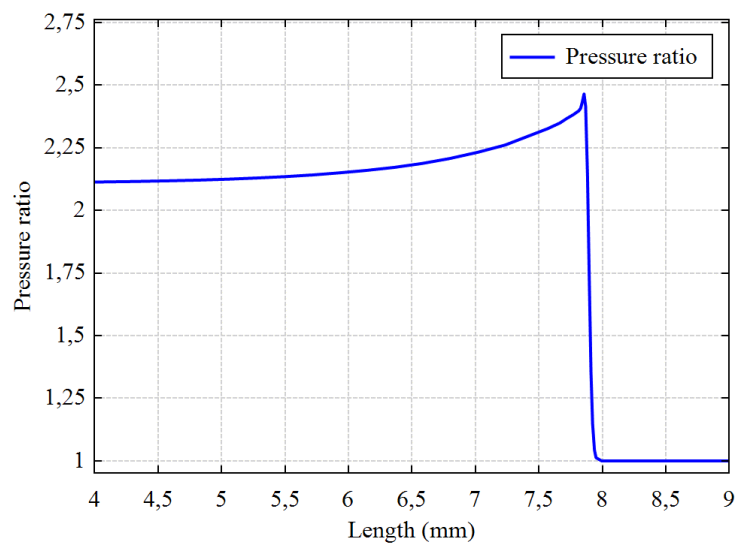


Figure 5.37. Pressure ratios for Case J

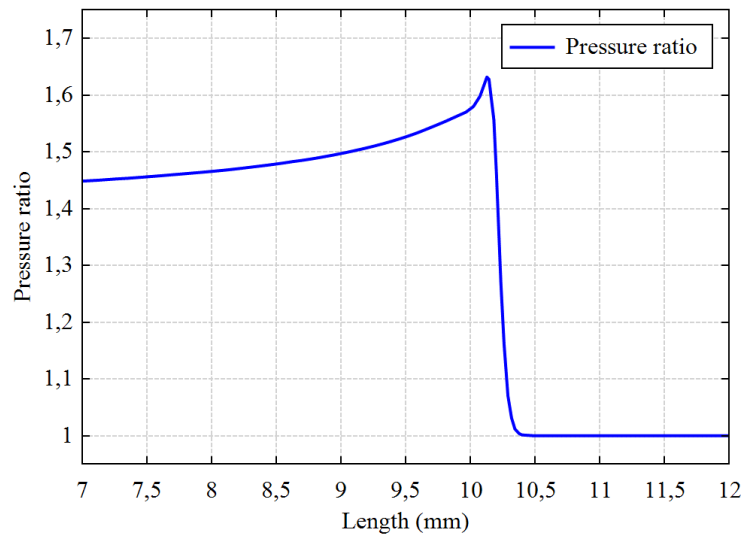


Figure 5.38. Pressure ratios for Case K

D. Velocity and Pressure Contours from Numerical Solutions

Velocity and pressure contours are prepared by using the numerical solutions and given from Figure 5.39 to Figure 5.51 for studied cases.

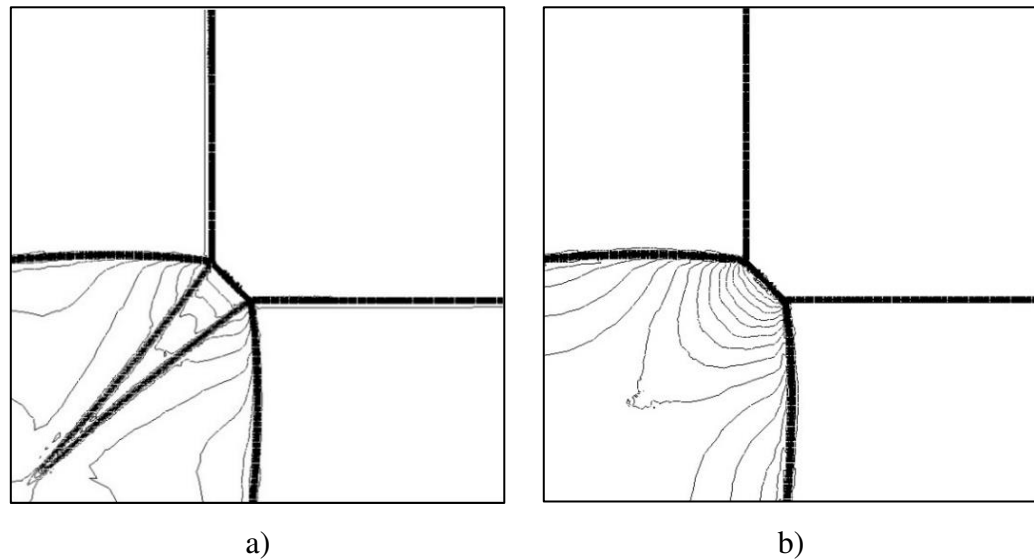


Figure 5.39. Contours of Case Ref. [17] for Mach number (a) and pressure (b)

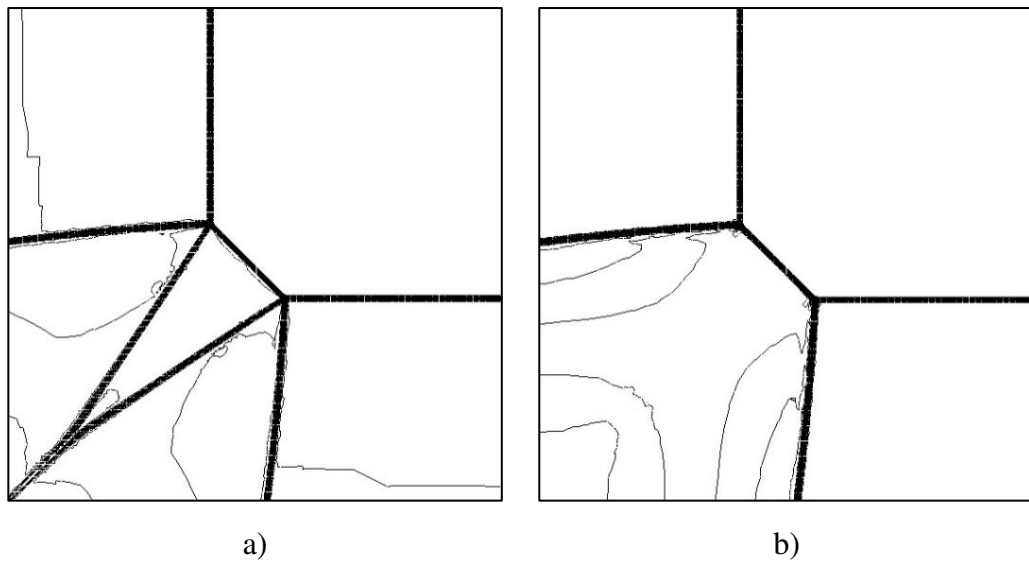


Figure 5.40. Contours of Case Ref. [14] for Mach number (a) and pressure (b)

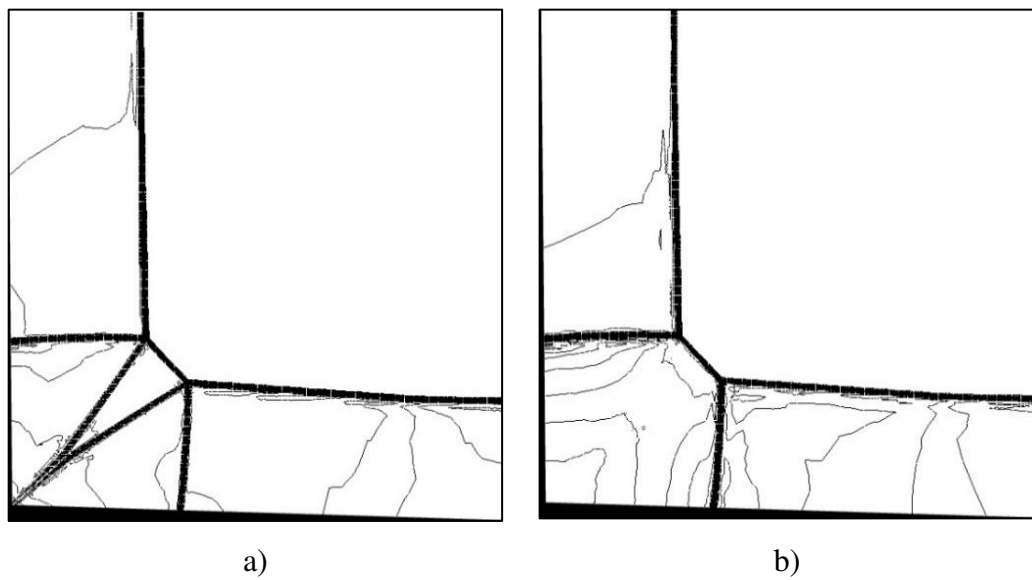


Figure 5.41. Contours of Case A for Mach number (a) and pressure (b)

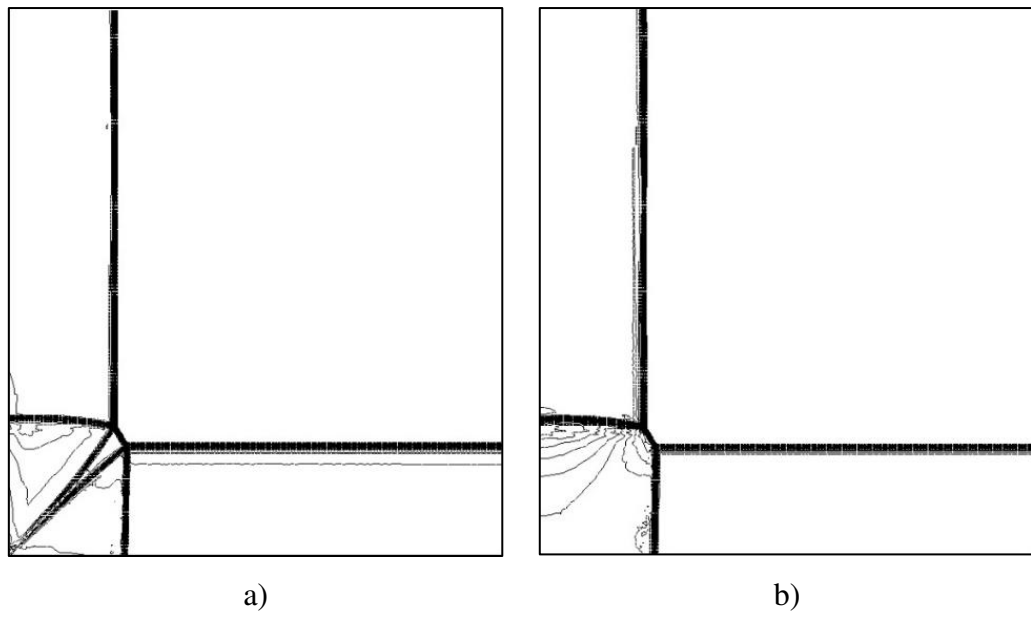


Figure 5.42. Contours of Case B for Mach number (a) and pressure (b)

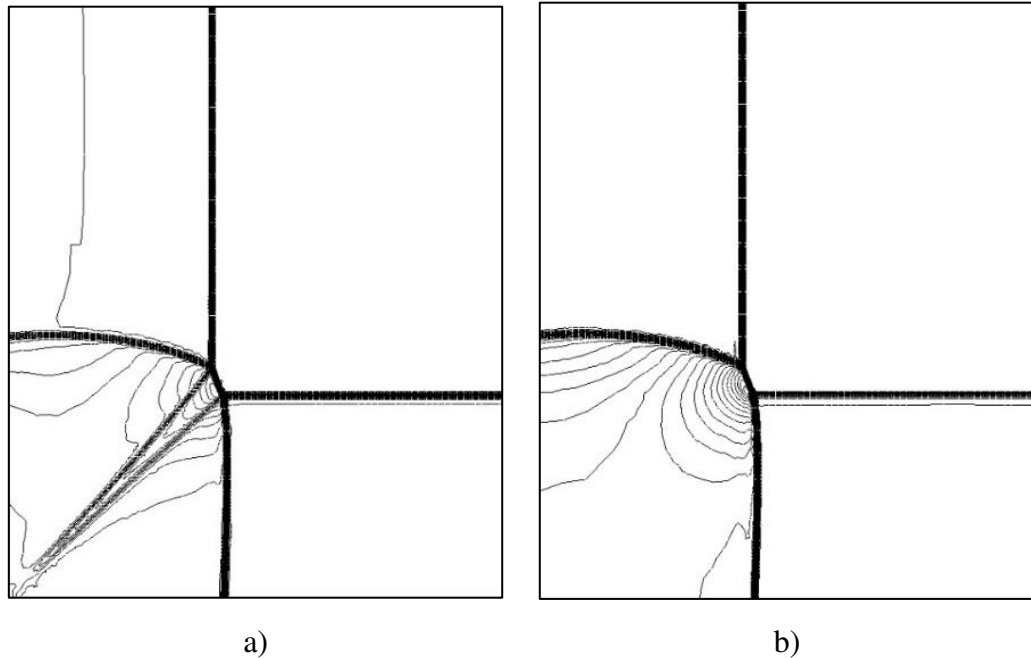


Figure 5.43. Contours of Case C for Mach number (a) and pressure (b)

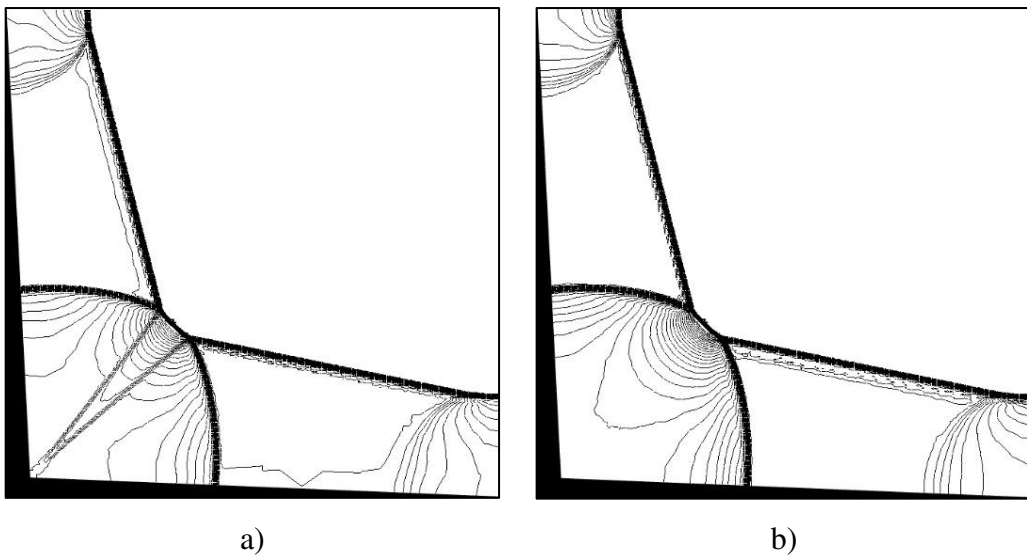


Figure 5.44. Contours of Case D for Mach number (a) and pressure (b)

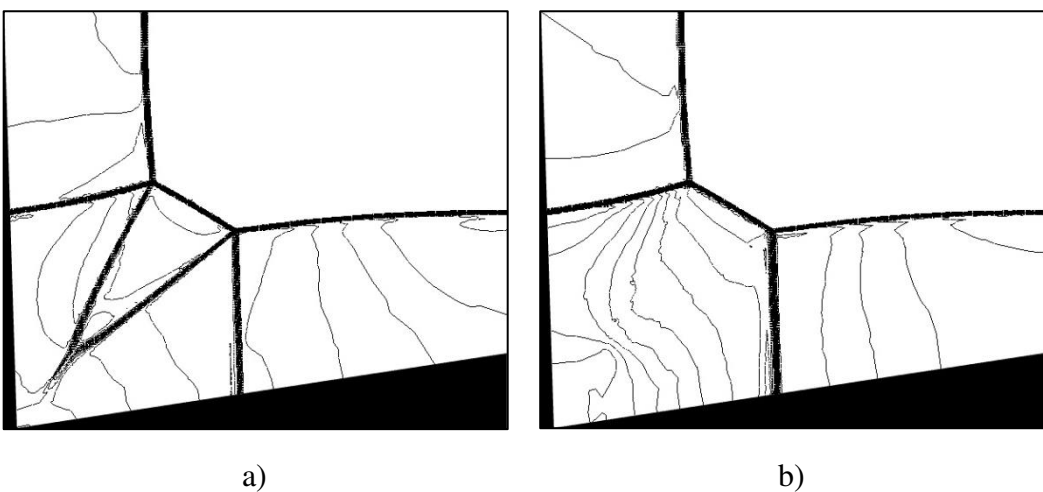


Figure 5.45. Contours of Case E for Mach number (a) and pressure (b)

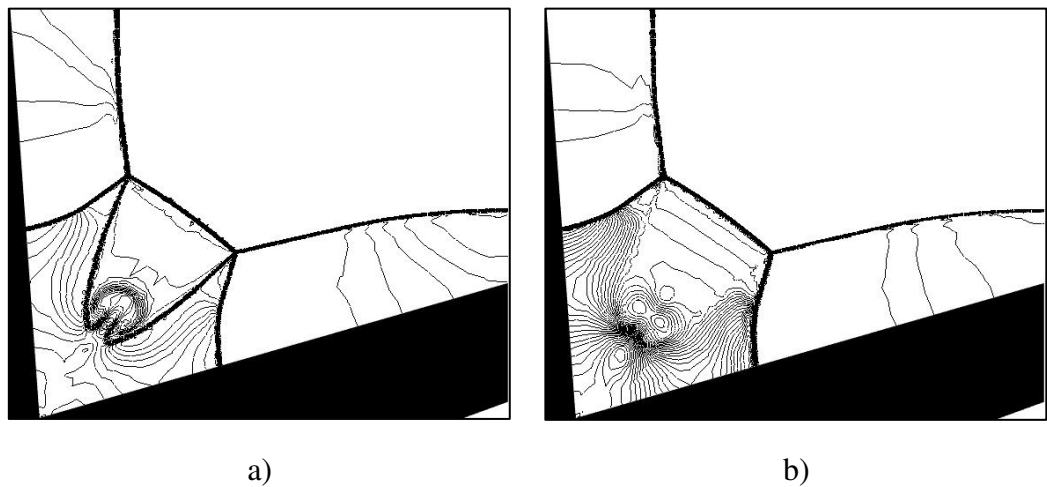


Figure 5.46. Contours of Case F for Mach number (a) and pressure (b)

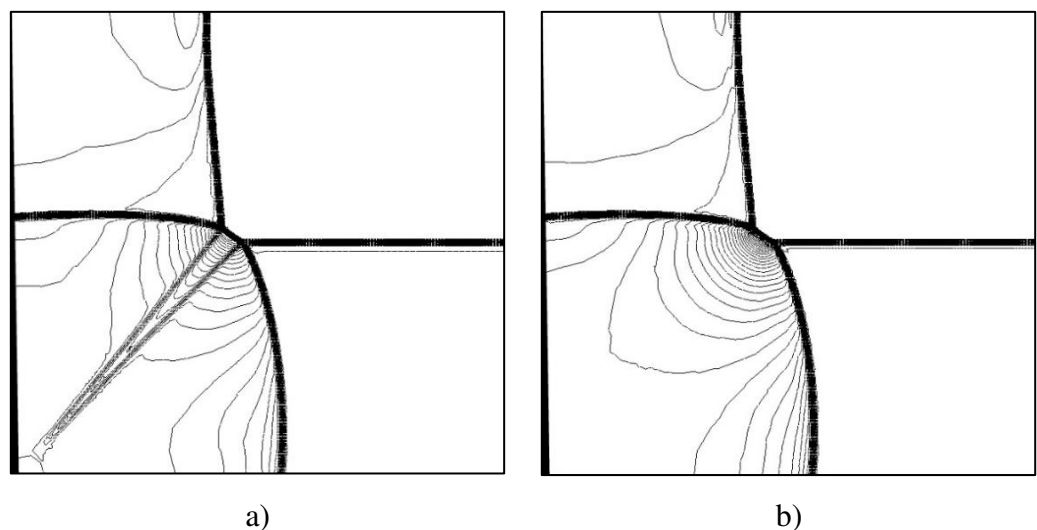


Figure 5.47. Contours of Case G for Mach number (a) and pressure (b)

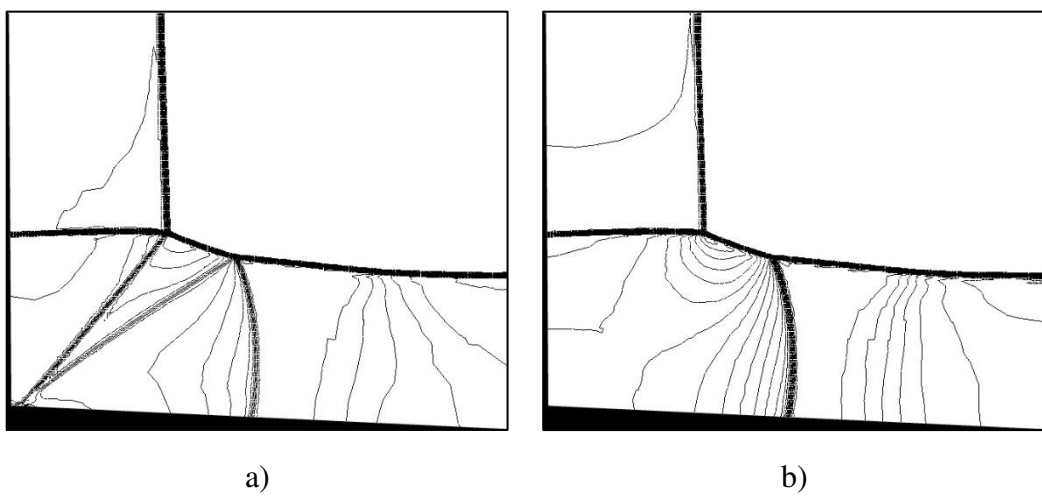


Figure 5.48. Contours of Case H for Mach number (a) and pressure (b)

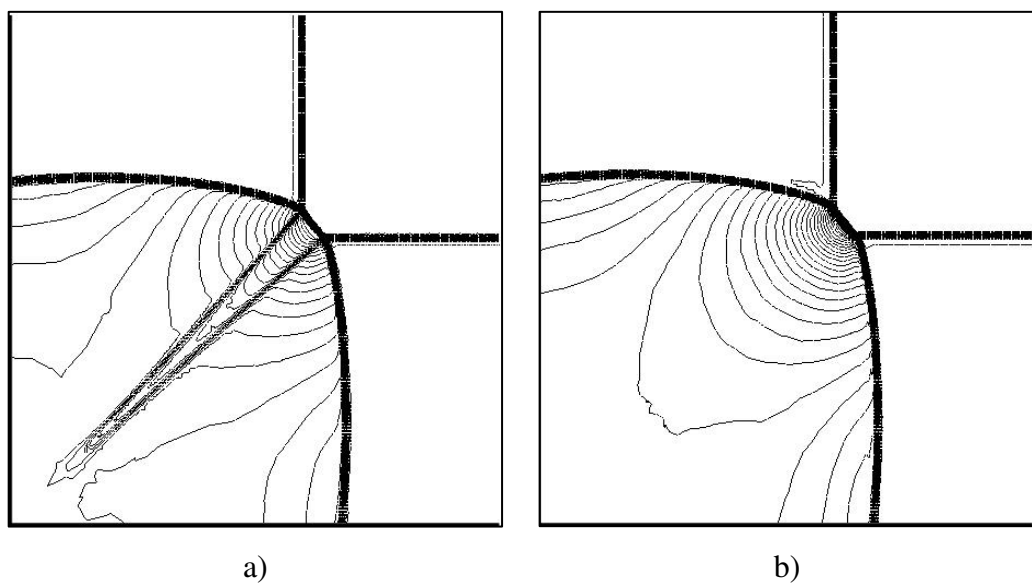
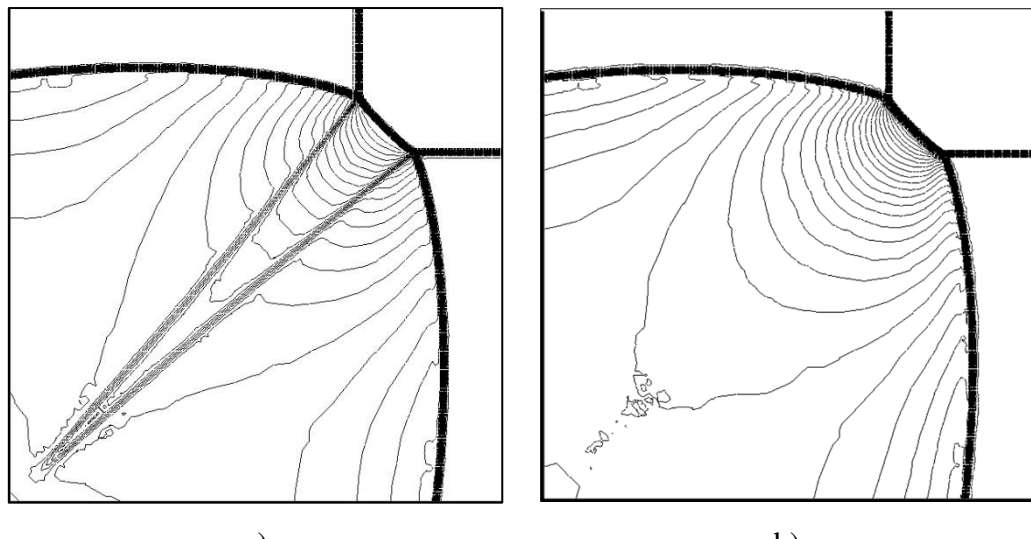


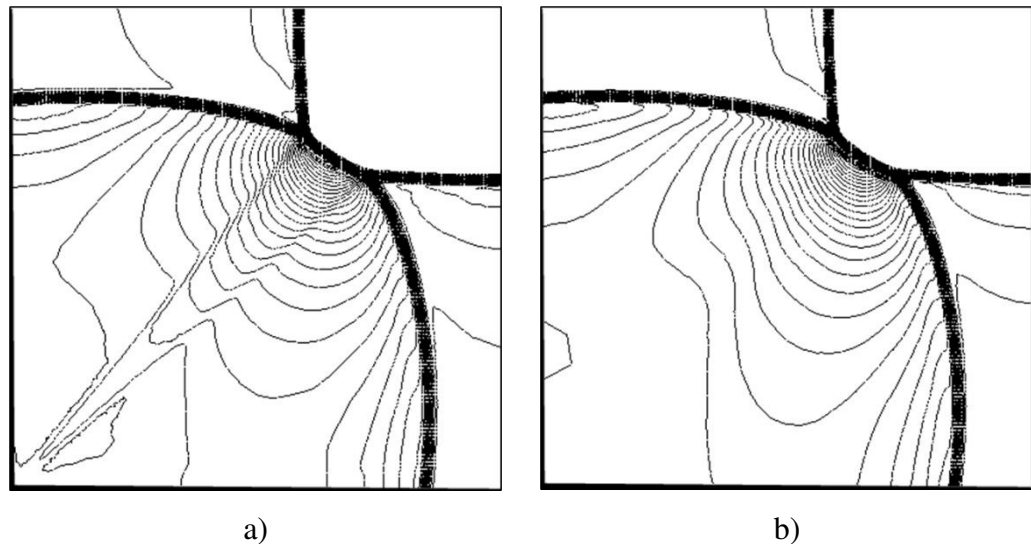
Figure 5.49. Contours of Case I for Mach number (a) and pressure (b)



a)

b)

Figure 5.50. Contours of Case J for Mach number (a) and pressure (b)



a)

b)

Figure 5.51. Contours of Case K for Mach number (a) and pressure (b)